Theoretical Insights into the Light Alkanes Dehydrogenation and Aldehydes Hydrogenation on Transition Metal and Metal Oxide Surfaces

Zur Erlangung des akademischen Grades eines

Doktors der Naturwissenschaften
(Dr. rer. nat.)

von der KIT-Fakultät für Chemie und Biowissenschaften
des Karlsruher Instituts für Technologie (KIT)

genehmigte

Dissertation

von

M.Sc. Eduard Araujo-Lopez

Abstract

Because of their extensive use as chemical building blocks, light olefins, such as propylene and ethylene, are among the essential types of compounds in the chemical industry. As a result, the demand for these building blocks has increased steadily over the last few years. For instance, the direct formation of propylene from propane is a well-established commercial process, which, based on energy consumption, is environmentally preferred to the current large-scale sources of propylene from steam cracking and fluid catalytic cracking. Moreover, there is still a big window for catalyst improvement, such as $C-H$ bond activation, reducing propane and hydrogen adsorption on surface sites, and minimizing coke formation.

By using density functional theory (DFT) calculations, it is investigated the C–H bond activation of light alkanes (methane, ethane, propane, n-butane) on transition metals (TMs), metal oxides (MOs), and single-atom-doped-metal oxides (M_1-MOs) surfaces, as well as the hydrogenation of aldehydes on palladium surfaces. This thesis develops simple and highly accurate models for predicting the transition state energy (ΔE_{TS}) of the C–H bond activation of light alkanes (C_1-C_4) on TMs, MOs, and M_1-MOs using the final state energy (ΔE_{FS}) as a descriptor. In the case of the TM surfaces, the models cover the non-oxidative, O-, and OH-assisted C–H bond activation on closed-packed and stepped surfaces. Here, the variations in ΔE_{TS} between alkanes were primarily attributed to differences in dispersion contributions determined by the carbon-chain length. In the case of MOs and M_1-MOs, the C–H bond activation can be explained based on the Lewis acid-base properties of the surfaces. The linear scaling relationships (LSRs) generated are universal with no functional restrictions and cover a broad structural diversity of MOs and M_1-MOs catalyst surfaces, including the effect of superficial oxygen vacancies, several dopants, and more than one phase of the same MO, and different active sites. Thus, it is confirmed that the ΔE_{FS} is one of the most general descriptors to estimate ΔE_{TS} on TMs, MOs, and M_1-MOs when LSRs are employed. The LSRs generated in this work are expected to pave the way toward the computational development of new and better catalyst materials, guiding future experiments as a first-hand tool in heterogeneous catalysis.

Finally, the fundamental understanding offered by DFT calculations serves as a cornerstone in the complete process of computer-aided catalytic design. This is demonstrated by combining adsorption studies (substrate adsorption and temperature-programmed desorption) and DFT calculations, which are used to elucidate the factors affecting the hydrogenation of various aldehydes on a Pd-based catalyst. The importance of the side chain in determining the reactivity of the carbonyl group is demonstrated. Although the adsorption mode and strength are affected by the substrate structure, these aspects have proven not to be the decisive factors in the conversion of the carbonyl group.

Zusammenfassung

Leichte Olefine, wie Propylen und Ethylen, gehören aufgrund ihrer umfangreichen Verwendung als chemische Bausteine zu den wichtigsten Verbindungsarten in der chemischen Industrie. Infolgedessen ist die Nachfrage nach diesen Bausteinen in den letzten Jahren stetig gestiegen. So ist beispielsweise die direkte Herstellung von Propylen aus Propan ein etabliertes kommerzielles Verfahren, das im Hinblick auf den Energieverbrauch den derzeitigen großtechnischen Propylenquellen aus Steamcracking und katalytischem Wirbelschichtcracken ökologisch vorzuziehen ist. Allerdings gibt es immer noch ein großes Fenster für die Verbesserung des Katalysators, wie z. B. die Aktivierung von C−H-Bindungen, die Verringerung der Adsorption von Propan und Wasserstoff an der Oberfläche und die Minimierung der Koksbildung.

Mit Hilfe von Dichtefunktionaltheorie (DFT)-Berechnungen wird die C-H-Bindungsaktivierung von leichten Alkanen (Methan, Ethan, Propan, n-Butan) auf Oberflächen von Übergangsmetallen (TM), Metalloxiden (MO) und mit einem einzigen Atom dotierten Metalloxiden (M1-MO) sowie die Hydrierung von Aldehyden auf Palladiumoberflächen untersucht. In dieser Arbeit werden einfache und hochgenaue Modelle zur Vorhersage der Übergangszustandsenergie (ΔE_{TS}) der C-H-Bindungsaktivierung von leichten Alkanen (C_1-C_4) auf TMs, MOs und M_1-MOs unter Verwendung der Endzustandsenergie (ΔE_{FS}) als Deskriptor entwickelt. Im Falle der TM-Oberflächen decken die Modelle die nicht-oxidative, O- und OH-unterstützte C-H-Bindungsaktivierung auf geschlossen gepackten und gestuften Oberflächen ab. Hier wurden die Unterschiede in den ΔE_{TS} zwischen den Alkanen in erster Linie auf Unterschiede in den Dispersionsbeiträgen zurückgeführt, die durch die Länge der Kohlenstoffkette bestimmt werden. Im Falle von MOs und M_1-MOs lässt sich die Aktivierung der C−H-Bindung auf der Grundlage der Lewis-Säure-Base-Eigenschaften der Oberflächen erklären. Die erzeugten linearen Skalierungsbeziehungen (LSR) sind universell und unterliegen keinen funktionellen Einschränkungen. Sie decken eine breite strukturelle Vielfalt von MO- und M_1-MO-Katalysatoroberflächen ab, einschließlich der Auswirkungen von oberflächlichen Sauerstoffleerstellen, mehreren Dotierstoffen und mehr als einer Phase desselben MO sowie verschiedenen aktiven Stellen. Somit wird bestätigt, dass der ΔE_{FS} einer der allgemeinsten Deskriptoren zur Abschätzung der ΔE_{TS} auf TMs, MOs und M1-MOs ist, wenn LSRs verwendet werden. Es wird erwartet, dass die in dieser Arbeit generierten LSRs den Weg für die rechnerische Entwicklung neuer und besserer Katalysatormaterialien ebnen werden, die zukünftige Experimente als ein Werkzeug aus erster Hand in der heterogenen Katalyse leiten.

Schließlich dient das grundlegende Verständnis, das die DFT-Berechnungen bieten, als Eckpfeiler für den gesamten Prozess des computergestützten katalytischen Designs. Dies

wird durch die Kombination von Adsorptionsstudien (Substratadsorption und tempera-turprogrammierte Desorption) und DFT-Berechnungen demonstriert, die zur Klärung der Faktoren verwendet werden, die die Hydrierung verschiedener Aldehyde an einem Pd-basierten Katalysator beeinflussen. Die Bedeutung der Seitenkette bei der Bestimmung der Reaktivität der Carbonylgruppe wird aufgezeigt. Obwohl der Adsorptionsmodus und -stärke von der Substratstruktur beeinflusst werden, haben sich diese Aspekte nicht als die entscheidenden Faktoren für die Umwandlung der Carbonylgruppe erwiesen.

Contents

1.   Introduction

1.1.   Olefin Market

The importance of light olefins, such as propylene and ethylene, in the current market is because they act as a chemical platform in the manufacturing and chemical industry. In the production of a vast array of chemicals, including polymers (e.g., polypropylene and polyethylene), oxygenates, and essential chemical intermediates where the light olefins are used as building blocks [1]. As a result, global propylene capacity is expected to experience considerable growth over the upcoming years, from around 129.80 million ton per annum (mtpa) in 2019 to 191.84 mtpa by 2030 (Figure 1.1). Around 171 planned and announced propylene plants are expected to come online, primarily in Asia and the Middle East, over the upcoming years. Oriental Energy Co Ltd, Shandong Yulong Petrochemical Ltd, and Jinneng Science and Technology Co Ltd are the top three companies by planned and announced capacity additions globally over the upcoming years.
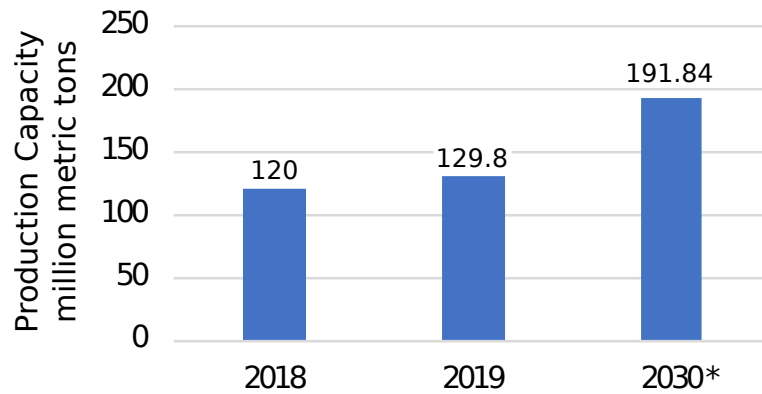
Figure 1.1. Global production capacity of propylene 2018-2030 (in million metric tons). Statista, copyright 2022.

There is an overwhelming planned capacity addition for propane dehydrogenation units in China, with predictions for the processing capacity expected to grow from 7 mtpa to 30 mtpa by 2030. Most likely, China will lead the global propylene industry over the next five years, with the most significant consumption and production increase [2]. With a rapidly industrializing and urbanizing economy, automotive, packaging, and electronic sectors have grown fast in China. It is forecast that Europe will solve imbalances in its propylene supply with additional imports. Currently, there are two propane dehydrogenation units

in Europe, but all indications are that new propane dehydrogenation investments are not viable options.

1.2. Propylene Production Processes

Commercial propylene production is carried out entirely without an oxidant. There are five main industrial processes patented, but commercially two processes are mainly used in the market: Olefex (from Honeywell UOP) and CATOFIN (from ABB Lummus). The former employs alkali metal-promoted $Pt-Sn/Al_2O_3$ catalysts in fluidized bed reactors, with additional catalyst regeneration and product recovery sections. The reaction runs pressures between 1 and 3 bar and temperatures ranging from 525 to 705 °C. On the other hand, chromium oxide supported on aluminum oxide is commonly employed industrially in the latter process. An alkali metal is used as a promoter, influencing both activity and selectivity by reducing the surface acidity of alumina. The reaction is run at approximately 575 °C and pressured between 0.2 and 0.5 bar. A conventional CATOFIN installation consists of 5−8 parallel adiabatic fixed bed reactors, and each reactor alternates between dehydrogenation, regeneration, and purge steps; as each reactor is made to run continuously, there are always some units performing dehydrogenation reactions, while other reactors are being regenerated or purged, resulting in a constant flow of reaction products. Finally, the other three processes have started to operate in the last couple of years; two of them employ Pt-based catalysts supported on modified alumina, and the last one does not contain precious metals or chromium, although the active components remain proprietary information [1, 3–5].

An examination of the patent literature shows the commercial interest in further developing dehydrogenation technologies; over the last decade, there has been a pronounced acceleration in the number of filed patents annually driven by the demand for propylene itself and the necessity for catalyst improvement. Besides, the majority of the filed patents are for non-oxidative dehydrogenation of propane (see Figure 1.2) [5].

1.3. Alkane Dehydrogenation

1.3.1. Non-oxidative Dehydrogenation

The nonoxidative dehydrogenation (non-oxiDH) of alkanes is a one-step reaction and in theory, there is only one by-product (molecular hydrogen), as illustrated below for propane:

$$C_3H_8 \iff C_3H_6 + H_2 \left(\Delta H^{\circ}_{298} = 124 \text{ kJ/mol} \right) \tag{1.1}$$
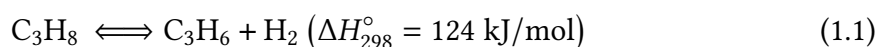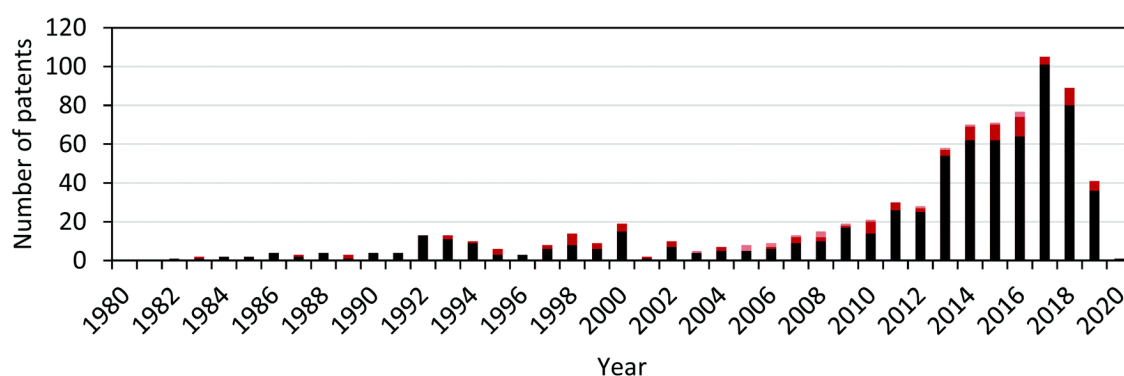
Figure 1.2. The number of patents published per year from 1980–2020 including the breakdown based on sub-reaction (non-oxiDH, black; ODH-O$_2$, medium red and ODH-CO$_2$, light red). Adapted from Ref. [5] with permission from the Royal Society of Chemistry, copyright 2021.

Several primary considerations are needed when dehydrogenating hydrocarbons [1, 5]. The first consideration is that the dehydrogenation reaction is endothermic, which means that heat must be added to the process to accomplish the reaction. Secondly, the chemical equilibrium of the dehydrogenation reaction favors olefins at low pressure and high temperature; therefore, the reactor pressure must be optimized throughout the entire process. The third fundamental is that the high-temperature requirement of the reaction inherently results in the formation of coke on the catalyst, which depresses catalyst activity. The resulting loss of catalyst activity requires regeneration to remove coke. Fourth, the thermal or gas phase reaction has a much lower selectivity to the desired product than the catalytic reaction, requiring the gas residence time at temperature to be minimized. An additional complicating factor is that olefins are considerably more reactive than their paraffinic counterparts, further leading to unwanted side and secondary reactions.

The so-called Horiuti-Polanyi mechanism, which was proposed in 1934 [6], is widely accepted as the mechanism for catalytic non-oxidative dehydrogenation. This mechanism follows the Langmuir-Hinshelwood kinetics, where all of the surface sites of the catalyst are considered to be identical and proceed as follows:

i. Dissociative adsorption of the alkane (cleaving the first C – H bond), formation of 1-propyl or 2-propyl.

ii. C – H cleavage of a second hydrogen from C$_3$H$_7$.

iii. Formation of a hydrogen molecule.

iv. Desorption of both hydrogen and the corresponding alkene.

Notably, both C – H cleavage steps and the dissociative adsorption of the paraffin have been suggested as the rate-limiting steps of the dehydrogenation reaction [7–10].

1.3.2. Oxidative Dehydrogenation

The oxidative dehydrogenation of alkanes with molecular oxygen (ODH-O_2) has some advantages that make it attractive, including the fact that the reaction is exothermic, enabling lower operating temperatures ($450 - 550\,°C$). In addition, this type of reaction is not limited by thermodynamic equilibrium. Although, overoxidation is the main drawback, with CO and CO_2 as by-products. The overall reaction for propane ODH-O_2 is presented below:

$$C_3H_8 + \frac{1}{2}\,O_2 \iff C_3H_6 + H_2O \left(\Delta H^{\circ}_{298} = -117\ \text{kJ/mol}\right) \tag{1.2}$$
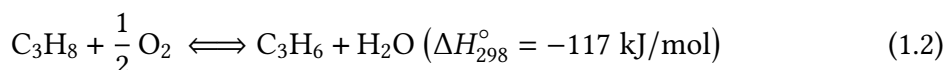
Oxidative dehydrogenation of alkanes in the presence of carbon dioxide (CO_2) is an attractive catalytic route for propylene production. It could have a lower environmental footprint than the ODH-O_2. Alkanes dehydrogenation reactions with CO_2 are complicated because they are thermodynamically limited at low temperatures and high pressures. Much of the discussion presented in the literature is presented in terms of propane ODH-CO_2 since the dehydrogenation mechanisms and kinetics of other alkanes (i.e., ethane and butane) are not entirely different [11–13]. Although the propane ODH-CO_2 $\left(\Delta H^{\circ}_{298} = 164\ \text{kJ/mol}\right)$ is even more endothermic than the propane non-oxiDH, the removal of hydrogen via the reverse water-gas shift (RWGS) reaction favors the thermodynamic equilibrium shifting towards higher propylene yields. Hence, the ODH-CO_2 can proceed at lower reaction temperatures than the non-oxiDH process (e.g., 450-600 $°C$). Under the same conditions, several side reactions can occur, for instance, dry reforming, cracking, hydrogenolysis reactions, and the Boudouard reaction for coke removal [14]. CO_2 is a great co-feed from both circular economic and ecological perspectives. Chemical CO_2 utilization is an attractive prospect for combating climate change; however, it is essential to consider how the CO formed during the ODH-CO_2 reaction (see Eq. 1.3) could be used sustainably in order to maintain a "renewable carbon" cycle, and avoid additional CO_2 emissions.

$$C_3H_8 + CO_2 \iff C_3H_6 + CO + H_2O \left(\Delta H^{\circ}_{298} = 164\ \text{kJ/mol}\right) \tag{1.3}$$

In general terms, the operation conditions for each dehydrogenation reaction are unique and are dictated by its thermodynamics. At the same time, there is a big window to improve, and the challenges that the reaction processes face are distinctive in each case. In the case of non-oxiDH, the coke formation remains the biggest challenge. For the ODH-O_2, being CO_2 the thermodynamically favorable product, overoxidation prevails. Lastly, in $ODH-CO_2$, the alkane dry reforming is a competing pathway; besides, the catalyst should have an affinity for both CO_2 and $C-H$ reactions.

1.4. Catalysts for the (O)DH of Alkanes

There are two main types of formulations used for the (oxidative) dehydrogenation of alkanes: metal- and metal oxide-based catalysts, where Pt- and Cr-based catalysts are the most extensively studied because of the commercial success of the non-oxiDH. Nevertheless, these materials also have been of interest to the ODH of alkanes. In recent years, promising results have been obtained for both reactions using nickel and palladium or metal oxides based on zirconium, gallium, and vanadium. These catalytic materials have been covered in several reviews from a theoretical perspective [10, 15], focusing on the oxidative processes [14, 16–18] or from a general perspective [1, 5, 19]. In addition, these materials are briefly discussed hereinafter.

1.4.1. Transition Metal-Based Catalysts

Albeit most of the noble metals (e.g., Pd, Rh) are active during the alkane dehydrogenation [20], Pt is the primary component in many dehydrogenation catalysts due to its superior ability to activate $C-H$ bonds and low activity to $C-C$ cleavage. Noble metals are active for dehydrogenation in the metallic state. Despite the fact that the dehydrogenation reaction of light alkanes seems to be surface insensitive, small particles are preferred as only the amount of active sites is relevant. The dissociative propane adsorption and the $C-H$ cleavage have been suggested as the rate-limiting steps [8–10]. Due to the reaction conditions, undesired side reactions such as hydrogenolysis, cracking, and isomerization compete with the dehydrogenation reaction. High surface area alumina is the classical support employed in these catalysts due to its high thermal stability, mechanical strength, and exceptional ability to maintain the platinum nanoparticles dispersed, crucial to attaining stable catalyst performance. Moreover, promoters such as Sn are required, and all of the Pt-based catalyst formulations that are industrially applied include this post-transition metal. The addition of Sn modifies both the platinum active-phase and the support. Essentially, Sn suppresses hydrogenolysis and isomerization reactions, minimizes metal sintering, neutralizes the acidity of the support, and facilitates the diffusion of the coke species from the metal surface to the support [21–23].

On the other hand, even though Ni and Pt are in the same periodic table group and possess many similar properties, Ni exhibits poor selectivity and stability for light alkane dehydrogenation. Mostly, due to the strong interaction between hydrocarbon and metal Ni, the main products are H_2, methane, and coke, rather than propylene [24, 25]. Other supported nanoparticles have been investigated, mainly for the ODH of propane. For instance, Nowicka et al. [26] carried out a detailed investigation into Pd/CeZrAlO$_x$ catalysts. It was shown that the presence of Pd facilitated CO_2 dissociation on the catalyst support. At 500 °C the catalyst achieved 9.5 % conversion and 93 % selectivity to propylene. Gomez et al. [27, 28] combined experimental and theoretical calculations to investigate mono- and bi-metallic nanoparticles supported on ceria at a reaction temperature of 650 °C and a CO_2:C_3H_8 ratio of 1:1. Among the catalysts tested were Ni$_1$, Fe$_1$, and FeNi alloys. In all

the cases, they found that the dry reforming reaction competes with the dehydrogenation pathway, limiting the propylene selectivity.

1.4.2. Metal Oxide-Based Catalysts

Chromium oxide is one of the most widely investigated catalysts for the non-oxiDH and ODH – CO$_2$ reactions. It is also one of the earliest reported transition metal oxide catalysts for the soft oxidation of propane to propylene [29]. Generally, the studies of Cr$_2$O$_3$-catalyzed ODH – CO$_2$ reactions are carried out under similar conditions to the non-oxiDH process, but with the addition of CO$_2$ to the gas-feed, typically supplied as a 1:1 ratio or in excess of the partial pressure of propane. The Cr-based catalysts captured one of the recurring themes in catalyst design for ODH – CO$_2$: some catalysts are inhibited by the addition of CO$_2$ while others perform much better.

During the non-oxiDH process, the rate-determining steps activate the propane molecule to form the adsorbed Cr$_3^+$ – C$_3$H$_7$ intermediate, and the β-H transfer to form the Cr$_3^+$ – C$_3$H$_6$ hydride surface species, which can significantly affect the non-oxiDH performance. As a catalyst support component, Al$_2$O$_3$ has been widely used in alkane dehydrogenation processes due to its appropriate chemical properties, high structural stability, and low-cost [30–32]. However, one of the major problems of the CrO$_x$/Al$_2$O$_3$ catalyst system is rapid deactivation, which occurs due to coke formation. Additionally, significant environmental and safety concerns still exist in the preparation, usage, and disposal of CrO$_x$-based catalysts due to the associated toxicity.

An alternative catalyst formulation is a Zr-based catalyst. Kondratenko et al. [33–35] found that ZrO$_2$ is active for non-oxiDH and showed how important are the crystallite size and phase composition in determining its activity. It was found that the propylene formation rate is inversely proportional to the crystallite size; besides, the amorphous ZrO$_2$ was very poorly active. With the help of density functional theory (DFT) calculations, they were able to identify coordinatively unsaturated Zr cations (Zr$_{cus}^{4+}$) as active sites, and the presence of oxygen defect was established to be essential for breaking the C–H bond, as shown in Figure 1.3.

Furthermore, this highly active and selective unsupported catalyst has been modified using dopants (such as V, Cu, and Cr). The concentration of dopant atoms and the temperature of reduction are contributing factors that affect the catalytic behavior of ZrO$_2$-based catalysts, which has a beneficial effect on the concentration of Zr$_{cus}^{4+}$ ions and the concentration of surface lattice oxygen. In tandem, all this plays an active role in propane activation [36–38]. More recently, Han et al. [38] investigated a range of Zr-containing metal oxides as supports for Zn, including ZrO$_2$, TiZrO$_x$, and CeZrO$_x$ (as well as control catalysts without ZrO$_2$, such as Al$_2$O$_3$ and SiO$_2$). Interestingly, it was shown that the formation of H$_2$ could be the rate-limiting step in the catalyst and not the C–H bond activation. Additionally, the presence of Ti in the catalyst support was shown to promote H$_2$ formation, which suggests that Ti, in general, is a good choice for a propane dehydrogenation catalyst. Finally, the
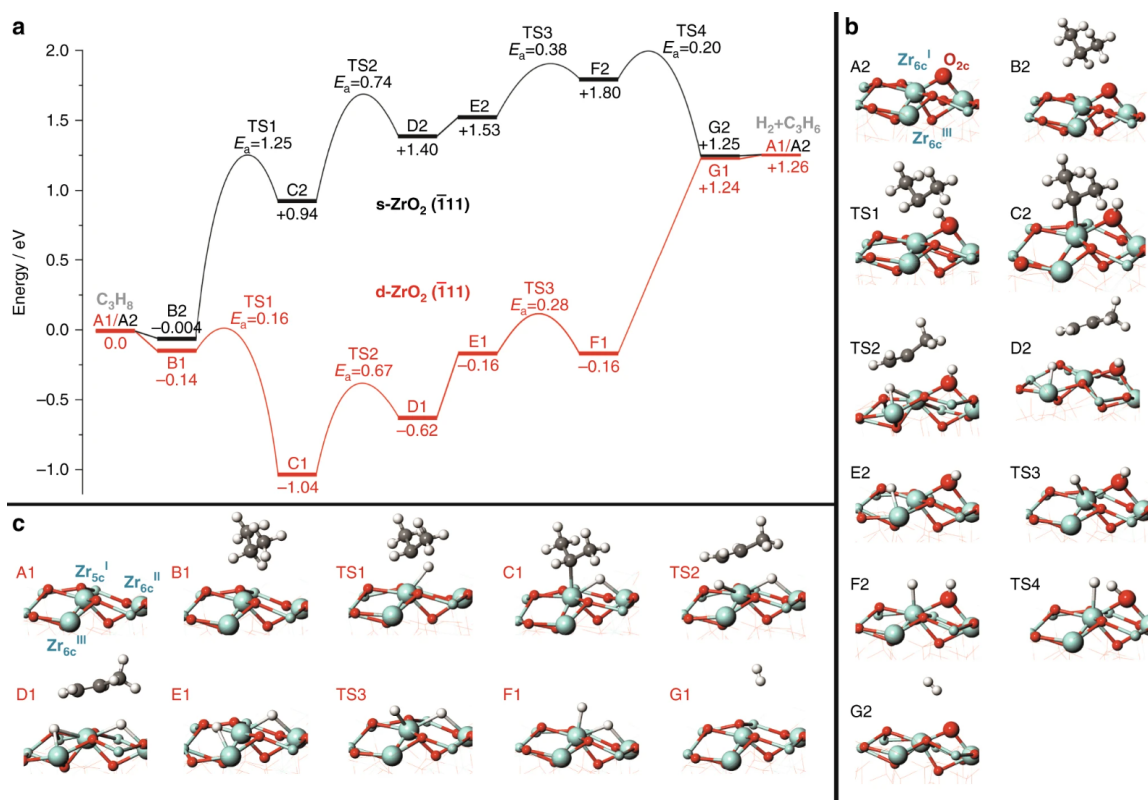
Figure 1.3. Mechanism of non-oxidative dehydrogenation of propane. (a) The calculated energy profiles along the pathways of propane dehydrogenation to propylene and the optimized structures of intermediates and transition states on (b) steocheometric-monoclinic-$ZrO_2(\bar{1}11)$ and (c) defective-monoclinic-$ZrO_2(\bar{1}11)$ surfaces (Cyan, grey, red and white symbols stand for Zr, C, O and H, respectively). Reproduced from Ref. [34] with permission from Springer Nature, copyright 2018.

observation that Zn-Zr catalyzed non-oxiDH is not limited by C – H bond activation is a significant finding.

It is also noteworthy that some metal oxides (e.g., Ga_2O_3 [39], SnO_2 [40], CeO_2 [41]) have evolved to more than just supports and can effectively catalyze a different set of reactions such as methane activation, alkane dehydrogenation, and alcohol dehydration reactions due to its inherent Lewis acid-base surface properties.

In brief, despite non-oxiDH being the only commercial process using Pt- and Cr-based catalysts, common issues have been identified independently of the catalytic reaction pathway, which requires further actions for catalysts improvement, such as C – H bond activation, reducing propane and hydrogen adsorption on surface sites, and coke formation minimization.

1.5. A Theoretical Perspective of the C–H bond Activation

In the early 1920s, the so-called Sabatier principle emerged [42, 43], pointing out that an optimum catalyst should have a suitable bind strength towards the reaction intermediate, which means that a strong binding leads to catalysts poisoning, and a too weak binding fails to activate the reactants. With the development of computational chemistry and, more recently, DFT, the study of heterogeneous catalytic processes and their elementary steps and mechanisms at the atomic scale has allowed the discovery of new catalytic materials throughout the use of activity descriptors [44]. Furthermore, as the reaction rates are essentially governed by only a few descriptors, a large number of potential catalysts can be screened rapidly utilizing computational chemistry [45, 46]. Nevertheless, the fundamental understanding offered by DFT calculations still serves as a cornerstone in the complete process of computer-aided catalytic design.

The alkane $C-H$ bond activation is one of the most active research topics for the industry and the scientific community. It comprises several crucial catalyzed industrial reactions such as dry reforming, steam reforming, partial oxidation, and (oxidative) dehydrogenation. Thus, industrial research has driven the search for new and more effective catalysts because there is still a big window to improve their selectivity and stability. For instance, considering the first dehydrogenation step as the rate-limiting step in the propane dehydrogenation [8, 9, 39], the main challenge is to control the consecutive oxidation of alkanes/alkenes to CO_x due to the much higher reactivity of products than the reactants. Here, the $C-H$ bond activation plays a critical role and how to activate this bond selectively is of prime interest. Within these topics, several comprehensive reviews have been published recently covering the theoretical transformation of methane, ethane, and propane over transition metal (TM) and metal oxide (MO) based catalysts [1, 10, 15, 18, 45, 47].

1.5.1. C–H Bond Activation on TM Surfaces

On metal catalysts, the $C-H$ bond cleavage of short alkanes might occur via three reaction pathways, the non-oxidative, O-, and OH- assisted activation. For instance, for methane, a systematic exploration of these reaction pathways over transition metal catalysts has been carried out [48–50]. Hibbitts et al. [50] found that the DFT calculated activation barriers of the O-assisted CH_4 dissociation are much higher than those of OH-assisted CH_4 dissociation; they also compared the activation barriers for CH_3^* dissociation of the three pathways, where the non-oxidative route exhibited the lowest activation barrier. The C-H bond activation of methane has also been extended to single-atom alloys where Ni-, Pd-, and Pt-doped surfaces have been suggested for activation of catalytically relevant species such as methane, methanol, and CO_2 [47, 51, 52]. In chapter 4, the C–H bond activation on TM surfaces will be further explored and expanded to short alkanes.

For the non-oxidative dehydrogenation of ethane at low conversion reaction conditions over Pt (Figure 1.4), it has been shown that the path to ethylene goes through ethane dehydrogenation to ethyl, $CH_3CH_2^*$, then to ethylene, while the non-selective pathway to

methane and deeply dehydrogenated species is predicted to go through dehydrogenation via CH$_3$CH*, this implies that the desorption step of ethylene is not the limiting step for selectivity [9]. Additionally, it has been identified that the (211) surface with step-edge sites generally shows higher activity than the close-packed (111) surface and alloying Pt with Sn dramatically increases ethylene selectivity by suppressing unwanted side reactions [53].
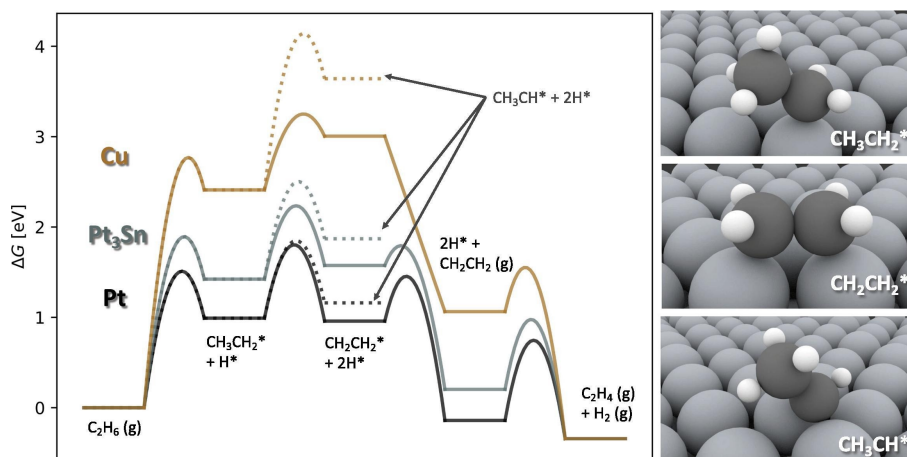
Figure 1.4. Free energy diagrams for the most relevant pathway in conversion of C$_2$H$_{6(g)}$ to C$_2$H$_{4(g)}$ in solid lines, plotted with the branching elementary step to CH$_3$CH* in dotted lines. Both pathways are plotted for Pt, Pt$_3$Sn and for Cu. The free energies are plotted at 873 K, 0.2 bar C2H6, 2×10^{-4} bar C$_2$H$_4$ (0.1% carbon conversion) and 0.6 bar H$_2$. Atomic structure models of key intermediates are rendered in the right panel, where large gray spheres represent surface atoms, black spheres represent C and small white spheres represent H. Reproduced from Ref. [9] with permission from Elsevier Inc., copyright 2019.

In the last few decades, the activation of C-H bonds of propane over transition metal and alloy surfaces using theoretical tools has been extensively studied, with particular attention to Pt surfaces [8, 23, 54–56]. The surface reaction of DH of propane can lead to numerous fragments ranging from C$_1$ to C$_3$ species adsorbed on these surfaces. As for the C$_3$ species, propane and propylene are the reactant and the desired main product. The propane dehydrogenation process involves a relatively complex reaction network and a large number of reaction intermediates, and the elementary steps involved are mainly the C–H and C–C bond-breaking reactions, as shown in Figure 1.5. These elementary steps can be divided into three categories (1) the dehydrogenation steps from propane to propylene (steps 1-4), (2) the deep dehydrogenation steps from propylene to 1-propenyl and 2-propenyl (steps 5 and 6), and (3) the C–C bond cleavage reactions of propane, 1-propyl, 2-propyl, and propylene (steps 7–10). The initial C–H bond cleavage at the methyl (step 1) or methylene (step 2) groups of physisorbed propane are often the rate determinant step that governs the rate of the overall dehydrogenation reaction leading to the 1-propyl, or 2-propyl species [57]. Recently, by using microkinetic analysis in combination with results from DFT calculations, Xiao et al. [58] investigated the implications of a reverse Horiuti-Polanyi mechanism on Pt surfaces finding that the propylene production at the under-coordinated active sites accounts for more than half of total production. In chapter 3, the (oxidative) dehydrogenation of propane on Pd surfaces will be further investigated.
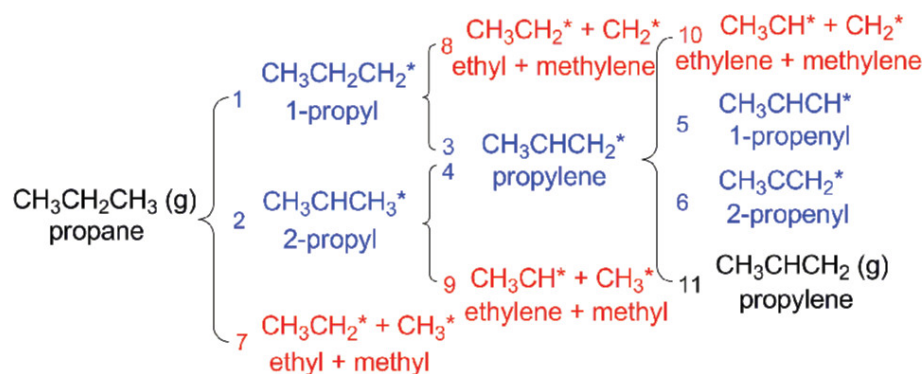
Figure 1.5. Reaction Network for Propane Dehydrogenation to Propenyl. The detached H atoms are not included for clarity. The numbers signify the sequence numbers of the elementary steps. Reproduced from Ref. [23] with permission from American Chemical Society, copyright 2012.

1.5.2. C–H Bond Activation on MO and M_1-MO Surfaces

On metal oxides and single-atom catalysts, alkane activation could occur via either the radical-like transition state (TS) or the surface-stabilized TS structure [59, 60]. The significant difference between the two transition states is the distance between the C atom and the interacted surface metal atom, which illustrates the distinct interaction between the alkane and the metal surface (see Figure 1.6). Regardless of the transition states, the nucleophilic surface oxygen attacks the electrophilic H in the C–H bond to form an OH bond in C–H bond activation.
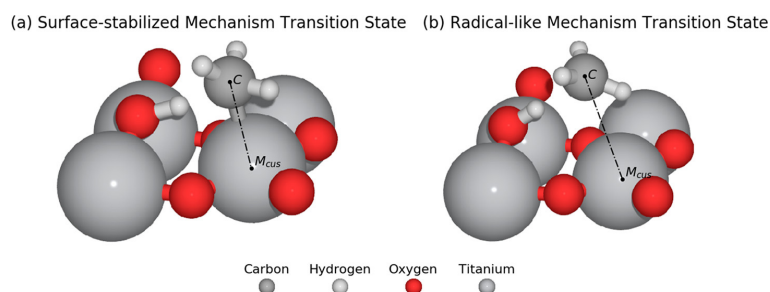
Figure 1.6. Two activation mechanisms on rutile-type metal oxide (110) surfaces are exhibited, (a) the surface-stabilized mechanism TS and (b) the radical-like mechanism TS. Reproduced from Ref. [61] with permission from American Chemical Society, copyright 2019.

The propane dehydrogenation on MOs has been extensively studied in the last decade. Worth to highlight are the studies by Zhu et al. [39, 57, 62–65]. They have studied the catalytic performance of DH of propane systematically on Cr_2O_3, ZnO, V_2O_3, and Ga_2O_3, including single atom-doped systems, identifying and testing several candidates. Furthermore, for the dehydrogenation reaction over some transition metal oxides without oxidants, active lattice oxygen can participate in the C–H bond activation as suggested for ZrO_2 by Kondratenko et al. [34]. The oxygen vacancies may affect the reactivity positively,

as in the case of α-Cr_2O_3, or negatively as in the case of ZnO, mainly due to the weaker Lewis acid-base interaction.

1.6.   Structure-Activity Relationships

Unfortunately, large-scale DFT calculations are computationally expensive, making the catalyst discovery based solely on DFT a very challenging task due to the vast materials space of potential catalysts. As a result, simulating realistic industrial processes involving numerous elementary reaction steps using only DFT becomes very challenging. For each elementary reaction step, a DFT calculation typically involves optimizing reactants and products on the catalyst surface, location of transition states, and verification of these states as energy minima/maxima along the reaction coordinate of interest. As all these calculations are highly computationally demanding, faster approaches to accelerate catalyst screening have always been imperative.
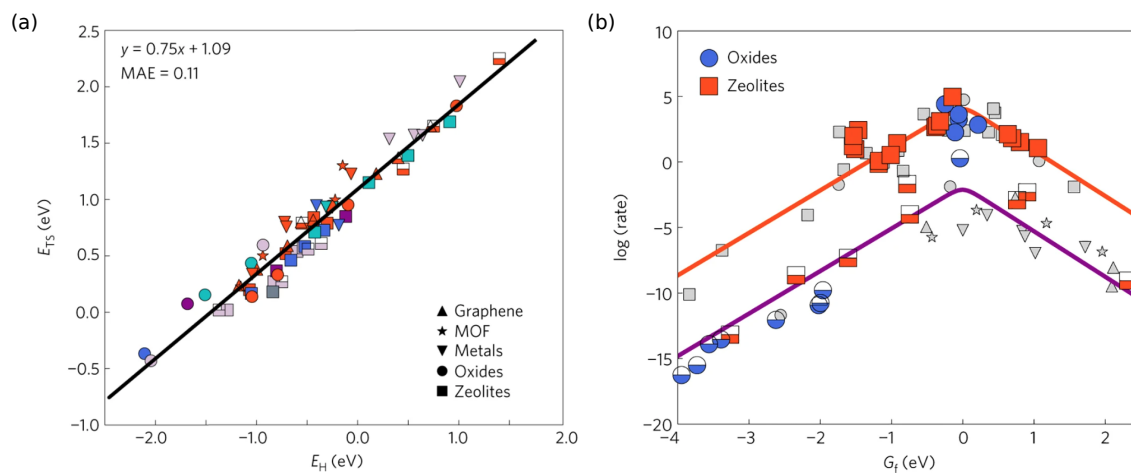
Figure 1.7. (a) Universal scaling relationship for methane C–H bond activation that proceeds via a radical-like TS. Filled symbols correspond to M_mO_x active sites, while half-filled symbols correspond to M–OH active sites. (b) Identifying promising catalysts for methane activation using scaling. Rate volcano for different zeolite topologies for M_mO_x active site motifs (red squares), $4d$ and $5d$ transition metal cations for M–O/CHA (half-filled red squares) and oxides (perovskites and strained IrO_2, blue circles). The filled symbols correspond to systems for which a transition state was explicitly calculated using DFT and half-filled symbols represent the rates predicted by the universal scaling relationship. Adapted from Ref. [59] with permission from Springer Nature, copyright 2017.

A significant step toward establishing high-throughput computational catalyst design tools was the development of the Brønsted-Evans-Polanyi (BEP) scaling relationships and later more general structure-activity relationships (SARs) [66–69], like the one shown in Figure 1.7a using hydrogen binding energy as a descriptor. In essence, SARs are mathematical expressions that correlate catalytic activity with inherent catalyst-adsorbate physicochemical properties and can aid the screening and discovery of new catalysts. Using such descriptors typically results in a description of catalytic performance that follows

a volcano-shaped activity behavior facilitating the identification of superior catalytic materials (Figure 1.7b); in particular, candidates near the volcano maximum exhibit high catalytic activity and moderate adsorption strength of reaction intermediates, in line with the Sabatier principle [59, 68]. The most frequently used descriptors for paraffinic C–H bond activation include the hydrogen adsorption, oxygen vacancy formation (in the case of metal oxides), and final state energies, as shown in Figure 1.8.

Figure 1.8. Word cloud depicting the frequency of reactivity descriptors use in SARs. Reproduced from Ref. [69] with permission from American Chemical Society, copyright 2022.

A step further is the combination of DFT calculations, ASRs, and kinetic models to study complex reaction mechanisms at the molecular level providing a framework that helps the researcher in identifying the bottlenecks for designing materials that may break these scaling relations to outperform traditional catalysts, making possible to improve existing or discover new materials. This methodology has expanded in the last decade, especially for reaction networks constituted by a moderate number of elementary steps and relatively small molecules, e.g., water gas shift reaction, syngas upgrading, methane upgrading, ethane/propane dehydrogenation, and electrochemical reactions [70].

1.7. Aldehydes Hydrogenation[1]

Supported metal nanoparticles have attracted growing attention in the past few decades as active and selective catalysts for several reactions of industrial interest [72, 73]. The hydrogenation and hydrodeoxygenation of aldehydes, in particular, are important industrial processes for the production of a wide range of chemicals used as solvents, fuels, plasticizers, detergents, pharmaceutical precursors, and fine chemicals [74–76]. Aldehydes can be found in several biomass-derived feedstocks; 5-hydroxymethylfurfural and furfural, for example, are the products of dehydration of fructose and xylose, respectively, while vanillin can be found in the complex lignin structure [77–79]. For this reason, the conversion of aldehydes is nowadays playing a crucial role, as the valuing of biomass-derived

---

[1] Section 1.7 is partially reproduced from Ref. [71].

compounds is a critical step toward the replacement of fossil fuel as a source of chemicals [80].

A vast body of work on the hydrogenation and hydrodeoxygenation of aldehydes using Pd-based heterogeneous catalysts is reported in the literature. Pd is considered a suitable catalyst for these reactions due to its capacity to dissociate and easily activate molecular hydrogen [81]. However, several aspects of the reaction mechanism of Pd-based catalysts still remain unclear. For example, the scientific literature is still vague on the effect of the side chains of aldehydes on the hydrogenation and hydrodeoxygenation of the carbonyl group. In addition, the physicochemical properties of the substituent groups on aldehydes can strongly affect their reactivity in several ways, such as increasing/decreasing the substrate adsorption (or modifying its geometry) through steric effects or increasing/decreasing the electronic density on the carbonyl bond.

A steric effect was first addressed by Kobayashi et al. using cyclohexanone and one of its methyl-substituted derivatives (2-, 3-, or 4-methylcyclohexanone) as model substrates [82]. The results clearly showed that the methyl-substituted ketones were less reactive than cyclohexanone over different metal catalysts (including Pd). The decreased reactivity was ascribed to steric hindrance of the methyl group's substrate adsorption on the catalyst surface. Moreover, Santori and colleagues observed a higher benzaldehyde hydrogenation rate than butyraldehyde over Pt-based catalysts, attributing the phenomenon to the lower strength of the $C=O$ bond in aromatic aldehydes than in aliphatic ones [83]. Kieboom also reported that electron-donating groups accelerate hydrodeoxygenation on the aromatic rings of benzyl alcohol derivatives over Pd-based catalysts [84]. Different results were, however, reported by Keane et al., they noticed a decreased rate for the hydrogenation of 2-methylbenzaldehyde compared with benzaldehyde over a Ni-based catalyst and ascribed this effect to the electron-donating property of the methyl group in the ortho position [85]. From a theoretical point of view, the study of long carbon-chain aldehydes requires a high computational effort; therefore, a substitute with a shorter carbon-chain can be selected as a probe molecule, as has been done before for octanal and propanal [86–89]. This approach allows the investigation of complex reaction mechanisms, obtaining valuable information at the atomic level within a reasonable computational time.

1.8.   Scope of the Thesis

By using Density Functional Theory (DFT) calculations, the first part of this thesis aims to gain a deeper understanding of the $C–H$ bond activation of light alkanes on metal and metal-oxide surfaces, a crucial step in several catalyzed industrial processes (e.g., dry reforming, steam reforming, partial oxidation, and (oxidative) dehydrogenation). Additionally, developing highly accurate predictive models can be a first-hand tool in the computational discovery of new and better catalytic materials. The second part aims to untangle the parameters that govern the reactivity of the carbonylic group toward the hydrogenation of aldehydes on Pd-based catalysts.

In line with this, in the third chapter, propane's (oxidative) dehydrogenation on palladium surfaces is taken as a study case. Then, in the fourth chapter, the first $C-H$ bond activation of light alkanes $(C_1 - C_4)$ is extended to eight transition metals, followed by the extension to metal oxide and single atom-doped metal oxide surfaces in chapter five. Finally, the second part (chapter six) investigates the hydrogenation of propanal/octanal and benzaldehyde on palladium catalysts.

- Chapter 3 investigates the non-oxidative and oxidative dehydrogenation of propane on Pd(111) and Pd(211), emphasizing the effect of oxygen and hydroxyl species on the activation energies.

- Chapter 4 focuses on the first (oxidative) dehydrogenation step of light alkanes (ethane, propane, and n-butane) on transition-metal (closed-packed and stepped) surfaces, including promoters and carbon-chain length effects in the transition state energies. Linear scaling relationships are developed for the non-oxidative, O-, OH-assisted reaction pathways.

- Chapter 5 is dedicated to the C–H bond activation of light alkanes (methane, ethane, and propane) on metal oxides and single-atom-doped metal oxides surfaces. The behavior of these systems can be explained based on the Lewis acid-base properties of the surfaces, including the dopants and defects effects. Additionally, previously published data using several functionals is collected and used to generate universal linear scaling relationships using the final state energy as the descriptor.

- Chapter 6 helps identify the factors affecting the hydrogenation of various aldehydes on a Pd-based catalyst, such as the effect of the side-chains, by a combination of DFT calculations and adsorption studies (substrate adsorption and temperature-programmed desorption) performed by our collaborators.

2. Computational Methodology

2.1. Introduction to Density Functional Theory

For the investigation of catalytic systems, density functional theory (DFT) is an essential and powerful tool for quantum mechanical modeling. Its origin can be traced back to the Thomas-Fermi model in the 1920s, and the formulation addressed by Kohn and Sham (KS) in the 1960s became the basis of the current computational methods. This chapter is based on the following references: Ashcroft and Mermin [90], Parr and Yang [91], Dreizler and Gross [92], Laird et al. [93], and Martin [94]. The DFT and electronic structures principles are covered from different perspectives in these books. Here the conventional DFT using plane wave functions will be discussed briefly. Additionally, some key concepts used throughout this thesis are introduced. Finally, in this section, at least otherwise is stated, atomic units are used such that $e^2 = \hbar = m_e = 1$.

Most catalytic systems can be described mainly by the motion of nuclei and electrons as well as their interactions in their stationary states. From a non-relativistic quantum mechanical description, these systems can be represented by the time-independent Schrödinger equation given by

$$\mathbf{H}\Psi_{tot}(\mathbf{r}, \mathbf{R}) = E_{tot}\Psi_{tot}(\mathbf{r}, \mathbf{R}) \tag{2.1}$$

where $\mathbf{H}$ is the multi-electronic-non-relativistic and time-independent Hamiltonian, the solution of the Schrödinger equation with $\mathbf{H}$ is the wave function $\Psi_i(\mathbf{r}, \mathbf{R})$, that depends of the coordinates of all-electrons ($\mathbf{r}$) and nuclei ($\mathbf{R}$), and the total energy of the system (E_{tot}). The Hamiltonian ($\mathbf{H}$) (considering the kinetic and potential energies of electrons and nuclei), is depicted in Eq. 2.2

$$
\begin{aligned}
\mathbf{H} = &- \sum_{A}^{N_{nuclei}} \frac{1}{2M_A} \nabla_A^2 - \sum_{i}^{N_{elec}} \frac{1}{2} \nabla_i^2 - \sum_{A}^{N_{nuclei}} \sum_{i}^{N_{elec}} \frac{Z_A}{|\mathbf{R}_A - \mathbf{r}_i|} \\
&+ \sum_{i}^{N_{elect}} \sum_{j>i}^{N_{elec}} \frac{1}{|\mathbf{r}_i - \mathbf{r}_j|} + \sum_{A}^{N_{nuclei}} \sum_{B}^{N_{nuclei}} \frac{Z_A Z_B}{|\mathbf{R}_A - \mathbf{R}_B|}
\end{aligned}
\tag{2.2}
$$

here first term corresponds to the kinetic energy of the nuclei ($\mathbf{T}_n$) with mass M_A, the second term is the kinetic energy of the electrons ($\mathbf{T}_e$), the third one is the electron-nucleus

attraction ($\mathbf{V}_{ne}$), followed by the electron-electron repulsion (V_{ee}), and the last term is the potential energy due to nucleus-nucleus repulsion ($\mathbf{V}_{nn}$). The equation 2.2 can be written more compactly as

$$H = T_n + T_e + V_{ne} + V_{ee} + V_{nn} \tag{2.3}$$

The Born-Oppenheimer separation of the electronic and nuclear motions [95] is a cornerstone in computational chemistry. It takes leverage of the difference in masses of the nuclei and electrons, assuming that the electrons react instantaneously to the changes in the atomic positions (considering that protons and neutrons are about 1800 times more massive than electrons). Hence, the wave function for a given state of a coupled-electron system can be written as a function of the nuclear coordinates and an electronic wave function, as shown below:

$$\Psi_{tot}(\mathbf{R}, \mathbf{r}) = \sum_i \chi_{n_i}(\mathbf{R})\psi_i(\mathbf{r}, \{\mathbf{R}\}) \tag{2.4}$$

where the curly brackets indicate that $\Psi^{electron}$ depends parametrically on $\mathbf{R}$. Therefore, Eq. 2.1 can be simplify as follows:

$$(\mathbf{T}_e + \mathbf{V}_{ne} + \mathbf{V}_{ee})\psi_i(\mathbf{r}, \mathbf{R}) = E_i\psi_i(\mathbf{r}, \mathbf{R}) \tag{2.5}$$

$$(\mathbf{V}_{nn} + E_i(\mathbf{R}))\chi_{n_i}(\mathbf{R}) = E_{tot}\chi_{n_i}(\mathbf{R}) \tag{2.6}$$

thus, the total energy E_{tot} is the sum of the E_{elec} and the constant nuclear repulsion term $\mathbf{V}_{nn}$.

Within the framework of density functional theory, the attractive potential exerted on the electrons by the nuclei (expected value from $\mathbf{V}_{ne}$ in Eq. 2.3) is also often termed to the external potential $\mathbf{V}_{ext}$, even though the external potential is not necessarily limited to the nuclear field and may include external magnetic or electric fields as well. Thus, the Hamiltonian of a multi-electronic system can be written in terms of the external potential

$$H_{elec} = T_e + V_{ext} + V_{ee} \tag{2.7}$$

from now on, the subscripts *elec* and *e* for the Hamiltonian are drop out, such that when referring to the Hamiltonian, it is the electronic Hamiltonian; the same goes for the kinetic and potential energies.

DFT does not focus on finding the wave functions; instead, DFT puts the electronic density of the system in the spotlight, which is related to the wave function as

$$\rho(\mathbf{r}_1) = N \int \int \dots \int |\psi(\mathbf{r}_1, \mathbf{r}_2, \dots, \mathbf{r}_N)|^2 \, d\mathbf{r}_2 d\mathbf{r}_3 \dots d\mathbf{r}_N \qquad (2.8)$$

The right-hand expression is quite similar to a wave function normalization expression. The difference is that one of the integrals is left out, leaving one index free. It is not important which one of the indices of the wave function is left as the electrons are indistinguishable, and the wave function must reflect this.

2.2. Hohenberg-Kohn Theorems

The heart of DFT are the two Hohenberg-Kohn theorems [96]. The first theorem states that the external potential is an unique functional of the electron density, $E[\rho(\mathbf{r})]$ (if the functional dependency is denoted with bracket parenthesis []). Additionally, it implies that the ground state density uniquely determines all properties, including the ground state's energy and function. The second Hohenberg-Khon theorem defines an important property of the functional and says that an universal functional of energy $E[\rho(\mathbf{r})]$ can be defined, and the global minimum represents the exact ground state energy of the system for a particular V_{ext}.

Therefore, the first useful conclusion is that the ground state wave function can be considered as a functional of the ground state density : $\psi[\rho]$. Further, the existence of an unapproximated energy functional is clear, $E[\rho]$:

$$E[\rho] = F[\rho] + V_{ext}[\rho] = \langle \psi[\rho] | \mathbf{H} | \psi[\rho] \rangle \qquad (2.9)$$

with $F[\rho]$ grouping the electronic contributions $T[\rho] + V[\rho]$.

2.3. Kohn-Sham Equations

In 1965 it became clear how to turn the theoretical framework of DFT into a practical computational tool as Kohn, and Sham [97] proposed a method for computing the most important part of the kinetic energy functional to good accuracy. The idea was to rewrite the problem of many interacting electrons to make it possible to use an analog with a system of many non-interacting electrons. The schemes proposed by Kohn and Shan can now be considered as approximations of a rigorous theory rather than just models.

It approximates the system of interacting electrons into a system of non-interacting electrons. The basic idea is to use the non-interacting kinetic energy as a new kinetic energy term and "put aside" all other energy contributions into the potential term as follows

$$v_{eff}(\mathbf{r}) = v_{ext}(\mathbf{r}) + \int \frac{n(r')}{|\mathbf{r} - \mathbf{r}'|} d\mathbf{r}' + v_{xc}(\mathbf{r}) \tag{2.10}$$

where the first term corresponds to the interaction between an electron and the collection of atomic nuclei ($v_{ext}(\mathbf{r})$), the second term is the Hartree potential that describes the repulsion between the electron been considered in one of the KS equations and the total electron density defined by all the electrons in the problem, the Hartree potential includes a so-called self-interaction contribution because the electron describes in the KS equation is also part of the total electron density, so part of it involves a Coulomb interaction between the electron and itself. The self-interaction is unphysical, and the correction is implicit in the next term v_{xc}; the last term defines all the contributions to the exchange and correlation of the single-electron equations and it is defined as a functional derivative

$$v_{xc}(\mathbf{r}) = \frac{\delta E_{xc}[\rho]}{\delta \rho(\mathbf{r})} \tag{2.11}$$

Therefore, by solving the corresponding non-interacting one particle orbital Schrödinger equation the correct density can be obtained

$$\left(-\frac{1}{2}\nabla^2 + v_{eff} \right) \psi_i = \epsilon_i \psi_i \tag{2.12}$$

the orbital obtained, ψ_i, are called KS-orbitals, while their corresponding energies, ϵ_i, are called KS-orbital energies. The density for the real system through the density of the non-interacting orbital system (accounting with a factor of two for a double degeneracy in each orbital because of the electron spin)

$$\rho(\mathbf{r}) = 2 \sum_i^N |\psi_i(\mathbf{r})|^2 \tag{2.13}$$

Finally, the real energy is obtained by inserting the density into Eq. 2.9 above. This is an iterative process because the effective potential (v_{eff}) depends on the density, which is the final goal; hence, the KS-equations have to be solved iteratively for self-consistency.

It is also important to highlight that the KS-orbitals are obtained from a mathematical trick and have very little to do with the actual electronic orbitals in the interacting multi-electron system. The same goes for the KS-orbital Schrödinger equation and energies. Despite this, it is pretty common to take the KS-orbitals and energies as approximations for the real orbitals and energies, and the results are usually surprisingly good [98, 99].

2.4. **Exchange and Correlation Energy**

In principle, the mechanism proposed by Kohn and Sham is exact; unfortunately, the true form of the exchange-correlation functional whose existence is guaranteed by the Hohenberg-Kohn theorem is simply not known. The oldest and simplest model is the Local (Spin) Density Approximation (L(S)DA), provided in its simple form by Kohn and Sham [97, 100], in which the exchange-correlation energy is an integral overall space with the exchange-correlation energy density at each point assumed to be the same as in a homogeneous electron gas density, this energy can be written as the sum of the exchange and correlation energies

$$E_{xc}^{LSDA}[\rho^{\uparrow}, \rho^{\downarrow}] = \int d\mathbf{r} \rho(\mathbf{r})[\epsilon_x^{hom}(\rho^{\uparrow}(\mathbf{r}), \rho^{\downarrow}(\mathbf{r})) + \epsilon_c^{hom}(\rho^{\uparrow}(\mathbf{r}), \rho^{\downarrow}(\mathbf{r}))] \qquad (2.14)$$

in this expression, only the exchange part is known analytically, and the correlation part is obtained from Quantum Monte Carlo calculations [101, 102].

Despite the success of the LSDA, the search for more accurate results has led to the development of various Generalized Gradient Approximations (GGAs), where a dependence on the gradient of the density is included

$$E_{xc}^{GGA}[\rho^{\uparrow}, \rho^{\downarrow}] = \int d\mathbf{r} \rho(\mathbf{r}) \epsilon_x^{hom}(\rho) F_{xc}(\rho^{\uparrow}, \rho^{\downarrow}, |\nabla \rho^{\uparrow}|, |\nabla \rho^{\downarrow}|, \ldots) \qquad (2.15)$$

where F_{xc} is a dimensionless enhancement factor depending on the local density as well as its gradient, and ϵ_x^{hom} is the exchange energy of the unpolarized gas.

One of the most frequently functional used in DFT calculations is the one developed by Perdew-Burke-Ernzerhof (PBE functional), which parameterizes F_{xc} such that the local approximation is recovered for low values of density gradients ($F_{xc}(0) = 1$), at large density gradients is constant and fulfills specific conditions. Additionally, it only makes use of fundamental constants for all the parameters.

On the other hand, Grimme's dispersion corrections model [103] describes the van der Waals (vdW) interactions (also called London dispersion interactions), which are multipolar interactions between molecules that are not directly bonded. If two atoms are very close, vdW interactions are repulsive because of the repelling forces between the negatively charged electrons. However, for intermediate distances, the induced dipole-dipole interactions are attractive.

The total energy , including the dispersion correction (DFT-D3), is given by

$$E_{DFT-D3} = E_{KS-DFT} - E_{disp} \qquad (2.16)$$

where E_{KS-DFT} is the usual self-consistent KS energy as obtained from the chosen density functional and E_{disp} is the dispersion correction as a sum of two- and three-body energies, $E^{(2)}$ and $E^{(3)}$, respectively. The most important two-body-term given by

$$E^{(2)} = \sum_{AB} \sum_{n=6,8,10,\dots} s_n \frac{C_n^{AB}}{r_{AB}^n} f_{d,n}(r_{AB}) \tag{2.17}$$

The first sum is over all atom pairs AB, C_{AB}^n denotes the dispersion coefficients of order $n = 6, 8, 10, \dots$ for atom pair AB, r_{AB} their internuclear distance, and s_n a scaling factors, which are adjusted for $n > 6$ and equal unity for $n = 6$. Finally, in order to avoid near singularities for small r_{AB} and (mid-range) double-counting effects of correlation at intermediate distances, damping functions $f_{d,n}$ are used which determine the range of the dispersion correction.

The long-range part of the interaction between three ground-state atoms is not precisely equal to the interaction energies taken in pairs, but applying the same concept of short-range damping analogously as for the pairwise term, it can be represented by

$$E^{(3)} = \sum_{ABC} f_{d,(3)}(\bar{r}_{ABC}) E^{ABC} \tag{2.18}$$

where the sum is over all atom triples ABC in the system, $f_{d;(3)}(\bar{r}_{ABC})$ is the damping function, used with well-defined parameters and with a geometrically averaged radii $\bar{r}_{ABC}$, and E_{ABC} is the dispersion term as derived from the third-order perturbation theory for three atoms ABC.

Throughout this document, the main functional employed is the Bayesian error estimation functional with van der Waals (BEEF-vdW). The BEEF-vdW functional is a general-purpose density functional for surface science and catalysis studies that describe bond breaking and formation and also includes non-local van der Waals dispersion interactions [104]. The choice of the BEEF-vdW functional is motivated by its performance concerning adsorption energies[105] and transition states [106] on transition metal surfaces. The GGA exchange energy density is conveniently expressed in terms of the exchange energy density of the uniform electron gas (ϵ_x^{hom}), and an exchange enhancement factor expanded in a basis M_x Legendre polynomials

$$E_{xc}^{GGA}[\rho, \nabla\rho] = \sum_m a_m \int d\mathbf{r} \epsilon_x^{hom}(\rho) B_m[t(s)] \tag{2.19}$$

where a_m are expansion coefficients, B_m is the Legendre basis function of orders 0 to $M_x - 1$ in a transformed reduced density gradient, denoted as $t(s)$. Although the BEEF-vdW functional includes van der Waals dispersion interactions, those contributions can not be explicitly obtained. When that was needed, single-point calculations were performed using the PBE functional with Grimme's dispersion corrections "D3" [103, 107].

2.5. Hubbard-Corrected DFT Energy

In materials in which electrons tend to be delocalized and strongly interact, such as transition metals oxides, rare earth elements, and compounds associated with strongly correlated systems (e.g., metal-insulator transitions), the traditional functionals do not incorporate such effects. Hence, to improve the prediction of electron localization and thus qualitatively understand the excessive delocalization of electrons induced by approximate energy functionals, the LDA+U method has been developed. This name indicates a Hubbard, "+U" correction to approximate DFT functionals such as, e.g., LDA, LSDA, or GGA. The LDA+U idea consists in describing the "strongly correlated" electronic states of a system (typically, localized d or f orbitals) using the Hubbard model. In contrast, the rest of the valence electrons are treated at the level of "standard" approximate DFT functionals. Within the LDA+U approach, the total energy of a system can be written as follows

$$E_{LDA+U} = [\rho(\mathbf{r})] = E_{LDA}[\rho(\mathbf{r})] + E_{Hub}\left[\left\{n_{mm'}^{l\sigma}\right\}\right] - E_{dc}\left[\left\{n^{l\sigma}\right\}\right] \tag{2.20}$$

where E_{LDA} represents the approximate DFT total energy functional being corrected, and E_{Hub} is the term that contains the Hubbard Hamiltonian to model correlated states. E_{dc} is the so-called "double-counting" (dc) term that models the contribution of correlated electrons to the DFT energy as a mean-field approximation of E_{Hub}, $n_m^{l\sigma}$ are the occupation numbers of localized orbitals identified by the atomic site index l, state index m (e.g., running over the eigenstates of L_z for a certain angular quantum number l) and by the spin σ [108]. In this study, the simplified approach introduced by Dudarev et al. [109] has been used.

2.6. Bloch's Theorem and Plane Waves

DFT has initially been tested for atomic and molecular systems with a finite, integer number of electrons [110, 111]. With the help of Bloch's theorem [112], the proof has been carried over to an infinite, periodic crystal of a semiconducting or insulating material using plane-waves as the basis set to expand the KS orbitals [113]. The wave function for an electron can be expressed as the product of a plane-wave and a function with the lattice periodicity.

$$\psi_{n,\mathbf{k}}(\mathbf{r}) = \exp(i\mathbf{k} \cdot \mathbf{r})u_{n,\mathbf{k}}(\mathbf{r}) \tag{2.21}$$

where $\mathbf{r}$ is a position vector, $\mathbf{k}$ is a so-called wave vector and may be considered a 'quantum number' that will only have certain allowed values defined by the size of the unit cell, $u(\mathbf{r})$ is a lattice-periodic factor, which is the same in each unit cell, $u(\mathbf{r} + \mathbf{R}) = u(\mathbf{r})$

If the periodic function $u_{n,\mathbf{k}}(\mathbf{r})$ is also expanded in terms of plane-waves determined by wave vectors of the reciprocal lattice vectors, $\mathbf{G}$, then the wave function can be entirely expressed in terms of a sum of plane-waves

$$\psi_i(\mathbf{r}) = \sum_{\mathbf{G}} c_{i,\mathbf{k}+\mathbf{G}} \exp(i(\mathbf{k}+\mathbf{G}) \cdot \mathbf{r}) \tag{2.22}$$

where $c_{i,\mathbf{k}+\mathbf{G}}$ are now coefficients that can be varied to determine the lowest energy solution. This also converts Eq 2.12 from an integral equation to a set of algebraic equations that can readily be solved using matrix algebra.

In practice, only a finite number of plane waves can be used. That is sufficient because there exists only discrete $\mathbf{G}$ because of the lattice periodicity, and the coefficients of small kinetic energy are usually most crucial [111]. The cut-off energy of the plane waves corresponds to the highest kinetic energy of all basis functions and determines the number of basis functions:

$$E_{cut-off} = \frac{\hbar^2}{2m} |\mathbf{G}_{max}|^2 \tag{2.23}$$

thus the convergence of the calculated total energy can be systematically investigated by increasing $E_{cut-off}$. Furthermore, plane-waves imply that periodic boundary conditions (PBC) are implemented, which are extremely useful to model periodic systems such as crystal bulks but inconvenient when atoms/molecules and surfaces are studied. Therefore, surfaces and molecules should be modeled using a *supercells* in order to create a vacuum between the periodic images, and the "non-periodicity" should be evaluated with a convergence test of the vacuum distance avoiding interactions between the unit cells.

2.7.   Core-electrons Treatment

The core-electrons of an atom are computationally expensive with plane-wave basis sets because they are highly localized and a very high cut-off energy would be necessary. In fact, the primary role of the core-electron wave-functions is to ensure proper orthogonality between the valence electrons and core states. Many modern plane-wave softwares employ effective potentials such as ultrasoft pseudopotentials [114] or the projector-augmented wave [115, 116] to describe the core-electrons, as the contributions of the core-electrons to bonding compared to those of the valence electrons is usually negligible. For more information, please, refers to Ref. [94].

2.8. Thermochemistry in Catalysis

In practice, it is reasonably straightforward to convert the potential energy determined from an electronic structure calculation into thermodynamic data, all that is required is an optimized structure with its associated vibrational frequencies. In this section, the most common procedures for augmenting electronic-structure calculations in order to convert single-molecule potential energies to ensemble thermodynamic variables are detailed [110, 117]. This thesis employs two standard approaches: the first is the ideal gas limit, and the second is the harmonic approximation.

2.8.1. Ideal-gas limit

In the ideal gas approximation, it is assumed that the $3N$ atomic degrees of freedom (DOFs) can be treated independently, and it is possible to separate them into translational, rotational, and vibrational components. For three-dimensional gases, there are three translational DOFs. Polyatomic molecules have three rotational DOFs extra, linear molecules have two, and monoatomic gases have none. The remaining DOFs are vibrations that are treated harmonically. The above allows the calculation of properties such as enthalpy H, entropy S, and Gibbs free energy G. The ideal-gas enthalpy is calculated from extrapolation of the energy at 0 K to the relevant temperature (for an ideal gas, the enthalpy is not a function of pressure):

$$H(T) = E_{elec} + E_{ZPE} + \int_0^T C_P \, dT \tag{2.24}$$

where the first two terms are the electronic energy and the zero-point energy (ZPE), and the integral is over the constant-pressure heat capacity. The E_{ZPE} is defined by

$$E_{ZPE} = \sum_i^{N_{nodes}} \frac{1}{2} h\omega_i \tag{2.25}$$

The heat capacity is separable into translational, rotational, vibrational, and electronic parts (plus a term of k_B to switch from constant-volume to constant-pressure):

$$C_P = k_B + C_{V,trans} + C_{V,rot} + C_{V,vib} \tag{2.26}$$

The translational heat capacity is $3/2k_B$ for a 3-dimensional gas. The rotational heat capacity is 0 for a monatomic species, k_B for a linear molecule, and $3/2k_B$ for a nonlinear molecule. The vibrational heat capacity contains $3N - 6$ DOFs for nonlinear molecules and $3N - 5$ DOFs for linear molecules (where N is the number of atoms). The integral of the vibrational heat capacity takes the form:

$$\int_0^T C_{V,vib} \, dT = \sum_i^{vib\ DOF} \frac{\epsilon_i}{\exp(\epsilon_i/k_B T) - 1} \tag{2.27}$$

where ϵ_i are the energies associated with the vibrational frequencies $\epsilon_i = h\omega_i$.

The entropy is found from

$$S(T,P) = S_{trans}^\circ + S_{rot} + S_{vib} + S_{elec} - k_B \ln \frac{P}{P^\circ} \tag{2.28}$$

where the translational (calculated at a reference pressure P°), rotational, electronic, and vibrational components are calculated as below

$$S_{trans}^\circ = k_B \left\{ \ln \left[\left(\frac{2\pi M k_B T}{h^2} \right)^{3/2} \frac{k_B T}{P^\circ} \right] + \frac{5}{2} \right\} \tag{2.29}$$

$$S_{rot} = \begin{cases} 0 & \text{, if monoatomic} \tag{2.30} \\ k_B \left[\ln \left(\frac{8\pi I k_B T}{\sigma h^2} \right) + 1 \right] & \text{, if linear} \tag{2.31} \\ k_B \left\{ \ln \left[\frac{\sqrt{\pi I_A I_B I_C}}{\sigma} \left(\frac{8\pi^2 k_B T}{h^2} \right)^{3/2} \right] + \frac{3}{2} \right\} & \text{, if nonlinear} \tag{2.32} \end{cases}$$

$$S_{vib} = k_B \sum_i^{vib\ DOF} \left[\frac{\epsilon_i}{k_B T \left(\exp(\epsilon_i/k_B T) - 1 \right)} - \ln \left(1 - \exp(\epsilon_i/k_B T) \right) \right] \tag{2.33}$$

$$S_{elec} = k_B \ln \left[2 \times (spin\ multiplicity) + 1 \right] \tag{2.34}$$

In the above, I_A, I_B, and I_C are the three principle moments of inertia for a non-linear molecule. I is the degenerate moment of inertia for a linear molecule. σ is the molecule's symmetry number. Finally, the ideal-gas Gibbs free energy is calculated from the combination of the enthalpy and entropy

$$G(T,P) = H(T) - TS(T,P) \tag{2.35}$$

2.8.2. Harmonic limit

A common example of this limit is the examination of the thermodynamics of an adsorbed species on a catalytic surface [118]. The $3N$ DOFs of the adsorbate are then assumed to be harmonic and independent of the modes in the surface. This allows the calculation of properties such as internal energy U and entropy S at a specified temperature T with the Helmholtz energy $F = U - TS$. If it is assumed that the PV term in $H = U + PV$ is negligible, then the Helmholtz free energy can be used to approximate the Gibbs free energy, as $G = F$. The internal energy and the entropy of the adsorbate are calculated as

$$U(T) = E_{elec} + E_{ZPE} + \sum_i^{harm\ DOF} \frac{\epsilon_i}{\exp(\epsilon_i/k_B T) - 1} \tag{2.36}$$

$$S = k_B \sum_i^{harm\ DOF} \left[\frac{\epsilon_i}{k_B T(e^{\epsilon_i/k_B T} - 1)} - \ln\left(1 - e^{\epsilon_i/k_B T}\right) \right] \tag{2.37}$$

2.8.3. Normal Modes

To determine the full set of normal modes in a DFT calculation, the main task is to calculate the elements of the Hessian matrix ($\mathbf{H}$), which is a square matrix of second-order partial derivatives . The Hessian matrix is defined as

$$H_{ij} = \left.\frac{\partial^2 E}{\partial u_i \partial u_j}\right|_0 = \frac{\partial F_j}{\partial u_i} \tag{2.38}$$

In the above expression, F_j denotes the force along the atomic coordinate axis j. Usually, the second derivatives that appear in the Hessian matrix can be estimated using finite-difference approximations.

2.9. Transition State Search

Transition state structures can be determined by searching for saddle points on the potential energy surface of the chemical species of interest. A first-order saddle point is a position on the PES corresponding to a minimum in all directions except one. In order to find these saddle points, two different methods have been used in this study: the nudged elastic band (NEB) and the DIMER methods. The NEB is a method for finding saddle points and minimum energy paths between known reactants and products [119, 120], the NEB method works by creating a series of Atoms objects between two local minima. These Atoms objects, images, are then relaxed in order to determine the lowest-energy pathway.

Unlike NEB, the DIMER method only requires a seed structure and is useful for finding most or all relevant pathways out of that guess. The DIMER method is a minimum mode following method which estimates the eigenmode corresponding to the lowest eigenvalue of the Hessian (minimum mode) and traverses the potential energy surface uphill in that direction [121]. Eventually, it reaches a first order saddle point with exactly one negative eigenvalue [117].

2.10. Miscellaneous

Figure 2.1 illustrates a potential energy diagram showing the reference energy levels used in throughout this document for the calculations of the the the ΔE_{IS}, ΔE_{TS}, ΔE_{FS}, ΔE_{ads}, ΔE_{act}, and ΔE_{rxn} for C–H bond activation of alkanes on transition metal (TM) and metal oxide (MO) surfaces.
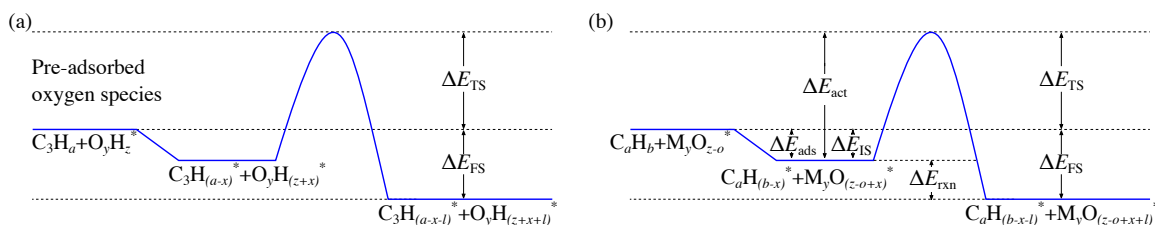
Figure 2.1. Potential energy diagrams for calculations depicting the different reference levels used for the ΔE_{IS}, ΔE_{TS}, ΔE_{FS}, ΔE_{ads}, ΔE_{act}, and ΔE_{rxn} on (a) TM and (b) MO surfaces.

The adsorption energy is defined as follows:

$$\Delta E_{ads} = E_{X+surf} - E_X - E_{surf} \tag{2.39}$$

in Eq. 2.39, all energies refer to systems with optimized structures; E_{X+surf} stands for the total energy of the molecule/species adsorbed, E_X is the energy of the adsorbate calculated in the gas phase, and E_{surf} is the energy of the slab. By this definition, a negative value corresponds to an exothermic process. The isolated molecules involved in the (oxidative) dehydrogenation of light alkanes (methane, ethane, propane, propylene, hydrogen, water, oxygen, and CO_2) were structurally relaxed inside a large simulation box of $15 \times 15 \times 15$ Å^3.

The dopant biding energy E_{bind} is defined as follows

$$\Delta E_{bind} = E_{M_1-MO} - E_{def-M_{x-1}O} - E_{gas}^M \tag{2.40}$$

where E_{M_1-MO} is the total energy of the doped system, $E_{def-M_{x-1}O}$ refers to the slab energy with a cation vacancy, and E_{gas}^M is the dopant energy at gas-phase.

The oxygen vacancy formation energy (OVFE) is calculated as follows

$$\text{OVFE} = E_{def} - E_{O_2}/2 - E_{nondef} \tag{2.41}$$

in Eq. 2.41, E_{def} refers to the slab without a surface oxygen, E_{O_2} is the oxygen gas-phase energy, and E_{nondef} is the energy of the pristine slab.

3.   (Oxidative) Dehydrogenation of Propane to Propylene on Palladium Surfaces

3.1.   Introduction

The markets for propylene derivatives have grown rapidly over the last few years and are likely to continue doing so [122, 123]. This demand is thought to be met by dehydrogenation of propane (DHP), with variants thereof being oxidative dehydrogenation using O_2 (ODHP) [124, 125] or CO_2 (CO_2-ODHP) [1, 11, 12]. Although the ODHP in the presence of molecular oxygen, as an oxidizing agent, favors low-temperature reactions and is exothermic, deep oxidation to CO_x is a significant drawback, which often results in loss of propylene selectivity and yield. To circumvent these issues, milder oxidants such as CO_2 are also explored [14].

Among the many catalysts tested for the DHP there are supported metal particles such as platinum [126, 127], nickel [25, 56], and palladium [26, 128], whereas metal oxides, such as chromium oxide [129], vanadium oxide [130, 131], and gallium oxide [132], but also carbon-based materials [124] and zeolites [133] have been proposed for ODHP. Among metal-based catalysts, only platinum has advanced to commercial applications of the DHP thanks to its superior activation of paraffinic C–H bonds and low activity toward undesired C–C bond cleavage [1]. The high cost of Pt, as well as the poisoning of the active sites by coke at high temperatures (showing poor propylene selectivity and fast deactivation), are the main limitations of the Pt-based catalysts [134].

On the other hand, studies on palladium-based catalysts have been scarce, although interest in these catalysts has increased in recent years [26, 128, 135–137]. Recently, Nowicka et al. [26] synthesized a Pd/CeZrAlO$_x$ material for CO_2-ODHP with long-term stability and high activity and selectivity. Additionally, selective DHP catalysts of PdM (M=Zn, In, Fe) alloys for olefin production showing improved stability compared to bare Pd nanoparticles have been reported [128, 136–138]. These studies suggest that the isolation of active metal sites by inactive atoms is responsible for high olefin selectivity, as it has been presented before for PtSn alloys [23].

While the reaction mechanism of DHP on Pt-based catalysts has been the subject of many computational studies [8, 23, 54, 134], theoretical investigations targeting Pd-based catalysts have not been reported to date. Herein, a mechanistic study of DHP and ODHP

---

over palladium (111) and (211) surfaces using density functional theory (DFT) calculations is reported. It is shown the mechanism by which propane is converted into propylene, how the structure of the metal surface is influencing activity, and the role of surface oxygen that would be present in ODPH is explored.

3.2. Computational Details

DFT calculations were carried out using the Vienna Ab Initio Simulation Package (VASP) [139, 140] and the Atomic Simulation Environment (ASE) [117] employing the generalized gradient approximation (GGA) using the Bayesian error estimation functional with van der Waals corrections (BEEF-vdW) [104, 141] and the projector-augmented wave (PAW) potentials [115, 116]. The kinetic energy cutoff and the k-point mesh were 450 eV and $4 \times 4 \times 1$, respectively. When specified, single-point calculations were performed using the PBE functional, including Grimme's dispersion corrections (PBE-D3) using the same parameters [103, 142].

Four-layer slabs with $p(3 \times 3)$ and $p(1 \times 3)$ supercells are used to represent the palladium (111) and (211) surfaces, with dimensions of 8.44×8.44 and 6.89×8.44 Å, respectively (see Figure 3.1). The two bottom layers of the slabs were fixed during the relaxations. In order to avoid interaction between periodic images, the Pd slabs are separated by ~ 15 Å of vacuum along the z-direction. In order to investigate possible interactions between periodic images, bigger supercells were used with four-layer slabs and sizes of (4×4) and (6×6) for the Pd(111) and Pd(211) surfaces (the k-points meshed were $3 \times 3 \times 1$ and $2 \times 2 \times 1$), respectively.
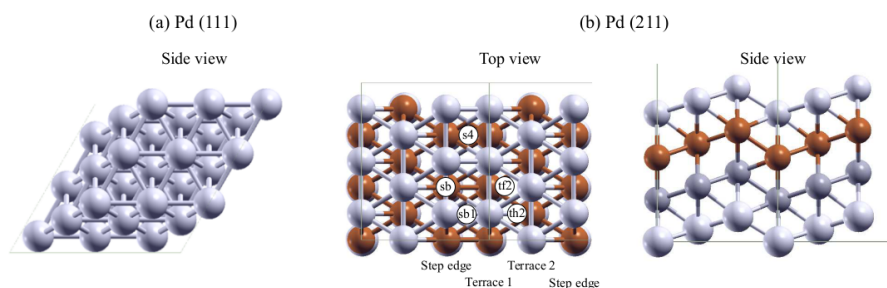
Figure 3.1. Pd(111) and Pd(211) surfaces. Adsorption sites are abbreviated as: **tf2**, fcc hollow site between terrace2 and step edge; **th2**, hcp hollow site between terrace2 and step edge; **sb1**, bridge site perpendicular to step edge; **s4**, fourfold hollow site in step; **sb**, bridge site parallel to step edge. Based on Orita et al.[143]

The reference systems used for the calculations of the adsorption, activation, initial, transition, final state, and D3 contribution energies were presented in section 2.10, including the methods used for the transition state searching and how the contributions to the free energy were calculated.

3.3. Adsorption of Species of Interest

In the first part of this study, the adsorptions of hydrogen, oxygen, and hydroxyl species were studied to identify how strong they are and prepare the pre-covered oxygen Pd surfaces. The adsorption energies of hydrogen over the Pd(111) and (211) surfaces are presented in Table 3.1. On the Pd(111) surface, atomic hydrogen prefers to adsorb on the fcc site; the most stable adsorptions over Pd(211) is the tf2 site. These values are in good agreement with previous theoretical studies [144, 145].

Table 3.1. Adsorption energies of hydrogen over Pd surfaces

Site	Pd(111) E_{ads} [eV]	Site	Pd(211) E_{ads} [eV]
fcc	-0.35	tf2	-0.28
hcp	-0.31	th2	-0.27
atop	+0.12	sb1	-0.16

The adsorption energies of atomic oxygen and hydroxyl on Pd(111) are investigated and compared with those on Pd(211); the results are listed in Table 3.2. The adsorption of atomic oxygen is preferred on fcc sites over both surfaces, fcc on Pd(111) and tf2 on Pd(211), respectively. In the case of hydroxyl, the bridges of the surfaces are preferred as adsorption sites. There is a good agreement between the results obtained here and the values reported previously [49, 146, 147].

Table 3.2. Adsorption energies of atomic oxygen and hydroxyl over Pd surfaces

Site	Pd(111) E_{ads} [eV]		Site	Pd(211) E_{ads} [eV]	
	O	OH		O	OH
fcc	-1.75	-2.25	tf2	-1.73	-2.29
hcp	-1.58	-2.09	sb/sb1	-1.55	-2.70/-2.67
atop	-0.24	–	s4	-1.37	–
bridge	–	-2.28	th2	-1.64	–

The calculated propane adsorption energies on Pd(111) and Pd(211) were -0.30 and -0.34 eV, respectively. This compares to the experimentally measured value of -0.46 eV for the Pd(111) surface [148] and presents an error of the same order of magnitude as that obtained for propane adsorption on other surfaces such as Pt [23, 149]. The differences in energy (for the adsorptions and transition states of C_3 species) between the supercells of different sizes are negligible, as reported in Table 3.3. Thus, the smaller supercells were used throughout the study. The effect of the oxygen and hydroxyl species on propane adsorptions is small on both surfaces ($\sim$ 0.02 eV), while the propylene adsorption energies are -0.73 and -0.95 eV on Pd(111) and Pd(211), respectively (see Figure 3.2).

The propane dehydrogenation was investigated on the clean Pd surfaces and in the presence of surface oxygen and hydroxyl species. Scheme 3.1 shows the reaction mechanism and intermediates involved in both processes. The reaction consists in two dehydrogenation steps: the first step is the conversion of propane (C_3H_8) into either 1- or 2-propyl (C_3H_7), followed by the conversion into propylene (C_3H_6). In the O (or OH)-assisted DHP mechanism, a surface oxygen atom (or OH) abstracts the hydrogen from propane and its intermediates, forming hydroxyl (or water).

Table 3.3. Difference in energy [eV] of initial, transition, and final states between $(3 \times 3)/(3 \times 3)$ and $(4 \times 4)/(6 \times 6)$ supercells of Pd(111)/Pd(211) for the direct and OH-assisted first dehydrogenation steps

		Propane	TS1	1-Propyl
Pd(111)	Non-oxidative	0.02	0.03	0.02
	OH-oxidative	-0.01	-	-0.04
Pd(211)	Non-oxidative	0.00	-	0.00
	OH-oxidative	-0.02	-	0.00

Pd(111)	(a) Propane	(b) Propane (O hcp)	(c) Propane (OH hcp)	Propylene
E_{ads} [eV]	-0.30	-0.32	-0.33	-0.73
Pd(211)	(a) Propane	(b) Propane (O tf2)	(c) Propane (OH sb1)	Propylene
E_{ads} [eV]	-0.34	-0.35	-0.36	-0.95
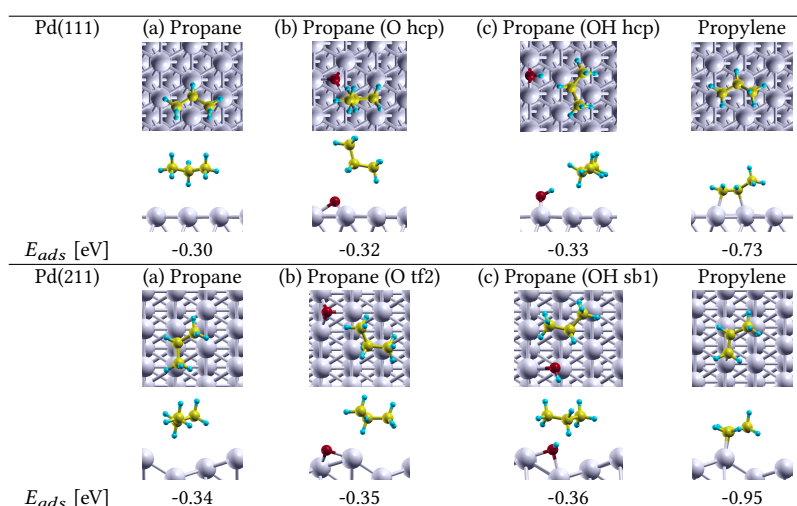
Figure 3.2. Top and side views of the most stable configuration of propane (a, e) on clean, (b, f) oxygen preadsorbed, (c, g) hydroxyl preadsorbed, and (d, h) propylene over Pd(111)/Pd(211) surfaces

Scheme 3.1. Reaction Mechanism of DHP (black) abd Oxidative DHP (ODHP, blue/red). The color code used in this scheme (black, blue, and red lines/markers represent the direct, O-, or OH- assisted dehydrogenation of C_xH_y species) is the same as in all of the other figures in this chapter.
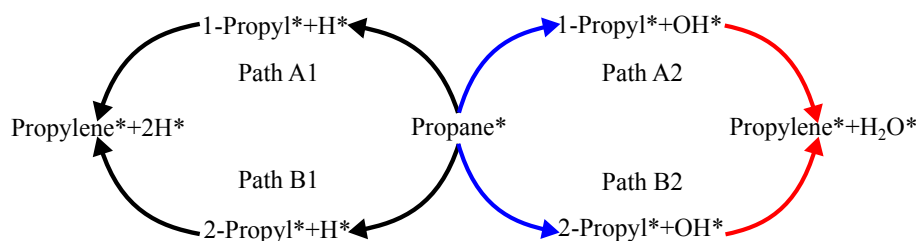
3.4. Mechanism of the Dehydrogenation of Propane over Pd Surfaces

Free energy diagrams at a temperature of 600 °C are shown in Figure 3.3, along with structures of intermediates and transition states. The temperature selection is due to the typical reactions conditions for DHP at an industrial scale [1]. As shown in Figures 3.3a and b, the energy barriers for the first dehydrogenation step are slightly higher for path B, where 2-propyl is formed as an intermediate. It can also be seen that Pd(211) has slightly

lower barriers, although the slight differences compared to Pd(111) show that the structure sensitivity of this reaction is not pronounced as commonly observed for dehydrogenation reactions [150]. Interestingly, the energy barriers for the second dehydrogenation step are lower for Pd(211) compared to Pd(111). For Pd(211), both dehydrogenation barriers are similar, with the first barrier being lower for path A1 and higher for path B1. Finally, the desorption of both hydrogen and propylene involves no effort for both surfaces at 600 °C, indicating that the reaction takes place in the low-coverage regime (within which all intermediates and reaction barriers have been calculated in the present study).
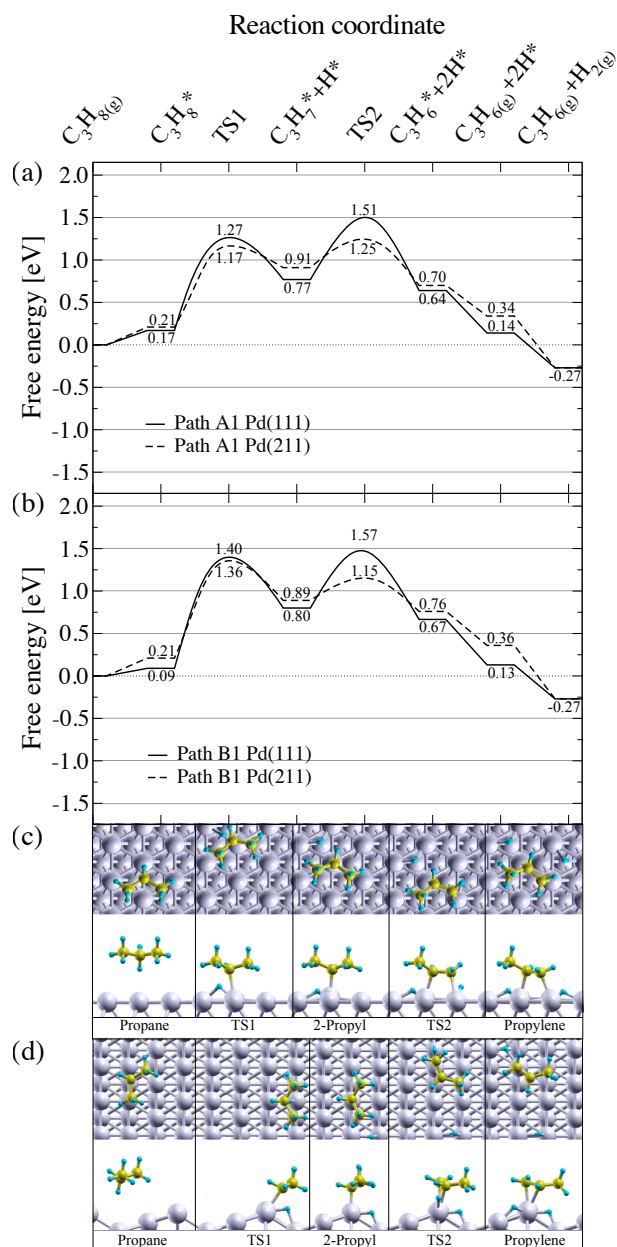

Figure 3.3. Free energy profile of DHP through (a) 1-propyl and (b) 2-propyl at 600 °C. Elementary steps of the reaction pathway B1 over (c) Pd(111) and (d) Pd(211) surfaces.

3.5.   Mechanism of Oxidative Dehydrogenation of Propane over Pd Surfaces

The free energy profiles for the ODHP over both Pd surfaces are shown in Figures 3.4a and b, and the elementary steps of the pathway B2 assuming a 2-propyl intermediate are presented in Figures 3.4c and d. The first dehydrogenation step is O-assisted (blue lines), while the second DH step is OH-assisted (red lines). Interestingly, the differences between the two reaction pathways of the ODHP are negligible between both Pd surfaces. The energy barriers of the first dehydrogenation step on the Pd surfaces are over 1.5 eV, 0.2-0.4 eV higher than the corresponding energy barriers for the non-oxidative DH process. The energy barrier of the second DH step is much lower: for the Pd(111) surface, around 0.7 eV for the direct route, and around 0.4 eV for the ODPH. For the Pd(211) surface, in the second DH step for ODHP, the energy barriers are slightly higher than those over the Pd(111) surface, which is in clear contrast with the direct route.

The previous results are further elaborated in Figure 3.5. If the first DH step proceeds via an OH-assisted pathway, the activation energies are comparable to the nonoxidative DHP (but the final states are always lower in energy), and the O-assisted steps are higher in energy barriers (Figure 3.5a and b). On the other hand, for the second DH step, it is clear that OH-assisted DH has the lowest energy barriers, while the barriers for direct and O-assisted DH steps are comparable (Figure 3.5c and d).

Figure 3.6 correlates the transition state energies (ΔE_{TS}) of all dehydrogenation steps expressed as a function of the final state energies (ΔE_{FS}) for reactions on clean, O*, and OH* covered surfaces (the reference energy levels are defined as shown in Figure 2.1a). The solid lines represent scaling relations between the transition state of methane activation calculated for clean (black), O* (blue), and OH* covered (red) transition metal (111) surfaces as described in an earlier study [49]. This study employed the RPBE [151] functional, which does not include dispersion forces. Hence, single-point calculations using the PBE-D3 [103, 142] functional to extract the D3 dispersion contributions of the final and transition states were performed. It was found that the transition and final states are stabilized by roughly the same amount (about 0.55 eV; see Table 3.4). Therefore, it is assumed that the results of DHP and ODHP can be compared to those calculated for CH_4 activation and be plotted against the corresponding transition-state scaling relations. The difference in correlations between (ΔE_{TS}) and (ΔE_{FS}) on clean transition metal surfaces and oxygen-assisted dehydrogenation is due to the different transition state scaling lines for dehydrogenation. These phenomena can be explained by compensation effects, as described earlier [146]. Interestingly, despite the use of different functionals, propane dehydrogenation follows almost the same scaling relation determined for methane dehydrogenation over (111) transition metal surfaces (re-scaled relations are presented in Figure 3.6 as well), indicative of a more general scaling relation independent of the functional used or the C_xH_y species considered [152]. Apparently, these results can also be extended to propane dehydrogenation over (211) transition metal surfaces, this will be extended in the next chapter.
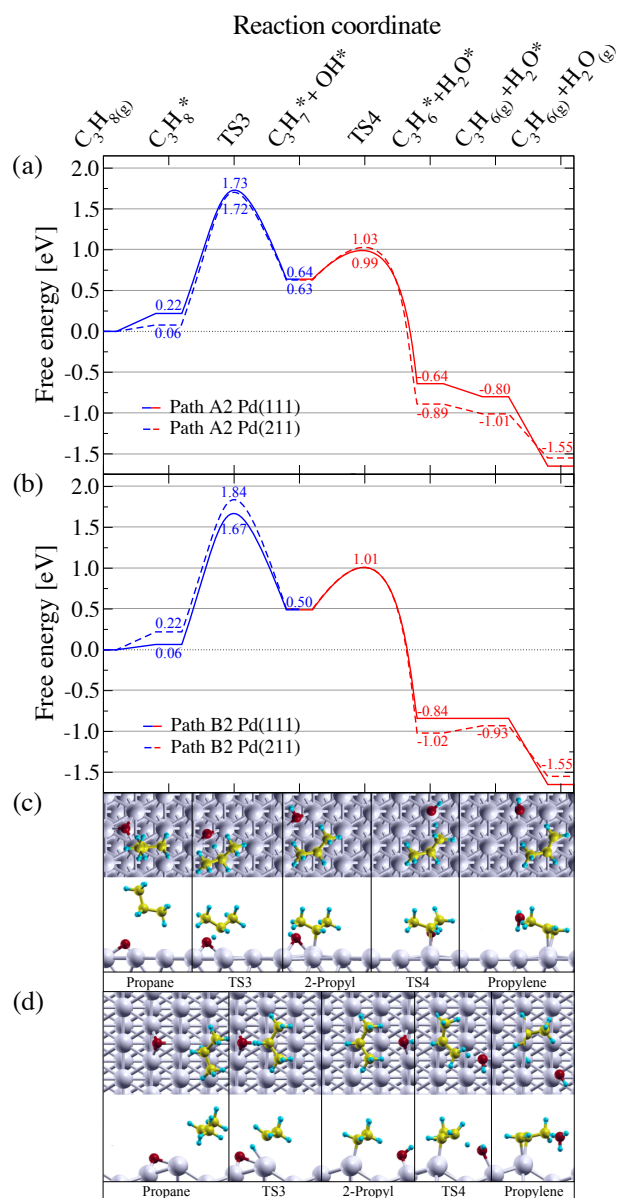
Figure 3.4. Free energy profile of ODHP through (a) 1-propyl and (b) 2-propyl at 600 °C. Elementary steps of the reaction pathway B2 over (c) Pd(111) and (d) Pd(211) surfaces.

Figure 3.6 shows that the O-assisted DHP has overall higher dehydrogenation barriers when compared with the direct dehydrogenation for Pd surfaces, even though the ΔE_{FS} is lower in energy; independently of the DH step and the position of the carbon from where the hydrogen is subtracted, O* does not favor DHP, as can be seen in Figure 3.7. On average, the OH-assisted dehydrogenation has the lowest activation energy but also the lowest final state energies, suggesting strong exothermicity. Here, the first (at ca. -0.5 eV) and the second (at ca. -1.0 eV) DH steps can be identified, wherein the first DH steps have comparable ΔE_{TS} to the direct DHP but lower ΔE_{FS}, whereas the second DH steps have the lowest ΔE_{TS} and ΔE_{FS}.
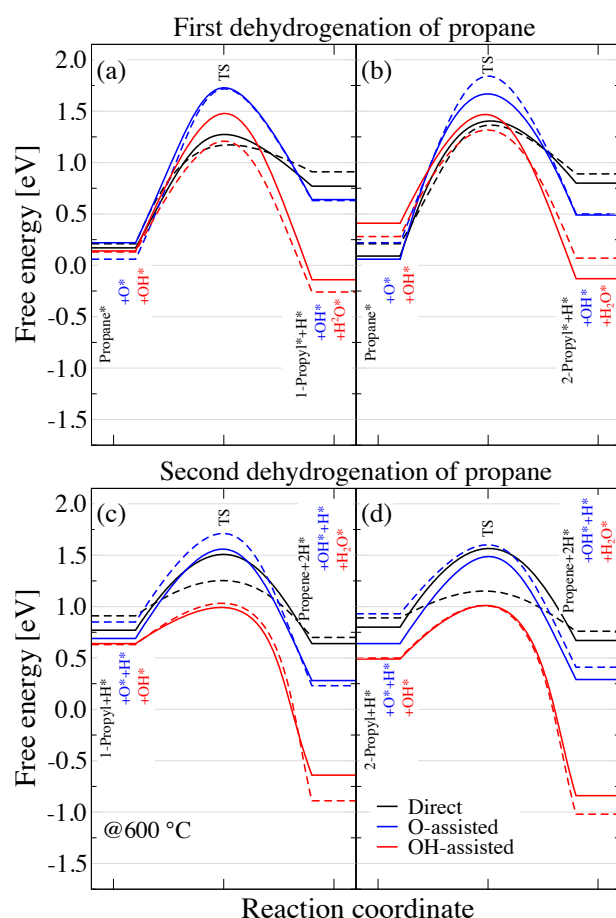
Figure 3.5. Direct, O-, and OH-assisted dehydrogenation of propane through (a) 1-propyl and (b) 2-propyl intermediate; and dehydrogenation of (c) 1-propyl and (d) 2-propyl intermediates. Solid/dashed lines correspond to Pd(111)/Pd(211) surfaces.

Table 3.4. D3 energies [eV] (relative to the gas-phase) of the PBE-D3 single point calculations

		TS1	Propyl	TS2	Propylene
Pd(111)	Path A1	-0.50	-0.50	-0.63	-0.65
	Path B1	-0.61	-0.61	-0.63	-0.67
Pd(211)	Path A1	-0.46	-0.48	-0.54	-0.59
	Path B1	-0.58	-0.51	-0.60	-0.61

		TS3	Propyl	TS4	Propylene
Pd(111)	Path A2	-0.53	-0.55	-0.53	-0.59
	Path B2	-0.60	-0.64	-0.60	-0.59
Pd(211)	Path A2	-0.51	-0.51	-0.52	-0.56
	Path B2	-0.55	-0.60	-0.55	-0.56

This analysis shows that while surface oxygen coverage will decrease the activity of palladium toward DHP, there might be an improvement overall when surface hydroxyl groups participate in the reaction. The extent to which this promotional effect of hydroxyl dominates the overall reaction mechanism depends crucially on the OH* coverage (and the corresponding coverage of O*). These coverages, in turn, depend on the type of oxidant
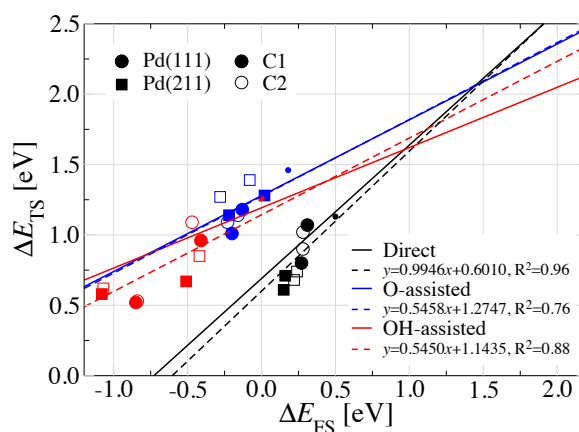
Figure 3.6. Transition state scaling relations for $C_3H_{8(g)}$ dehydrogenation on clean, O*−covered, and OH*−covered Pd(111) surfaces. Filled circles/squares, dehydrogenation from C_1 carbon on Pd(111)/Pd(211) surfaces; open circles/squares, dehydrogenation from C_2 carbon on Pd(111)/Pd(211) surfaces. Solid lines and small circles were taken from Yoo et al. [49] for CH_4 activation on transition metals (111) and Pd(111) surfaces, respectively.
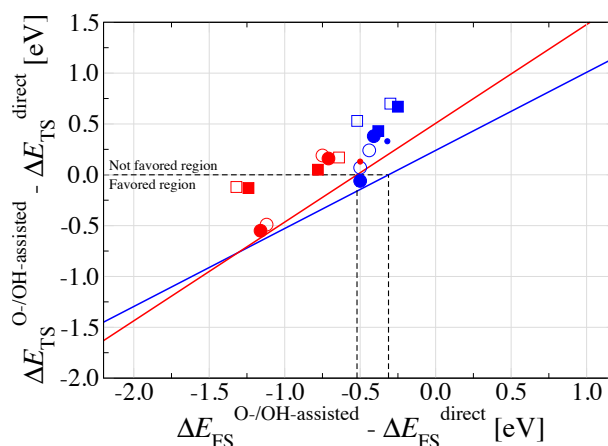
Figure 3.7. Difference in ΔE_{TS} between the O-(blue) or OH-(green) assisted, and the direct C_3H_8 dehydrogenation reactions as a function of the difference in ΔE_{FS}. Legends descriptions as in Figure 3.6. Solid lines taken from Yoo et al. [49] for CH_4 activation on (111) surfaces.

used and the corresponding reaction conditions. A detailed analysis of the steady-state coverages, however, is possible only with elaborate microkinetic models.

3.6. Chapter Conclusions

The reaction mechanisms of propane's (oxidative) dehydrogenation to propylene over palladium surfaces were analyzed using DFT calculations. It was found that the energy barriers of the oxidative dehydrogenation steps are always higher than those of the

nonoxidative route. This strongly indicates that oxygen does not considerably change the kinetics of this reaction on Pd surfaces. Furthermore, it was shown that the transition state energy scales with the final state energy (on Pd(111) and Pd(211) surfaces), both for the oxidative and nonoxidative dehydrogenation, in analogy to an earlier study on methane activation. To fully explore the potential of Pd-based catalysts, further studies concerning side reactions and catalyst deactivation would be needed.

4. Trends in the Activation of Light Alkanes on Transition Metal Surfaces

4.1. Introduction

The conversion of alkanes in the non-oxidative DH is limited by the production of hydrogen which shifts the thermodynamic equilibrium to the reactant side, and high temperatures are required to reach reasonable reaction rates [1, 125]. On the other hand, the oxidative DH (ODH) of alkanes using O_2 or CO_2 represents an attractive option, but is still in the early stages of development with catalyst design and process economics needing improvement. The use of molecular O_2 leads to an overoxidation, a low alkene yield and a fast deactivation of the catalyst, which is still very poorly understood. However, coupling this reaction with CO_2 (as a softer oxidant) which removes hydrogen through the reverse water-gas shift (rWGS) reaction moves the reaction again to the product side, thereby increasing the alkene yield [11, 14, 16, 26, 153]. The promoting/poisoning effect of the surface O* and OH* intermediates (formed during the ODH of alkanes) play an essential role in C-H bond activation, both in the functionalization of hydrocarbons and their partial oxidation. The first DH step herein has been shown to play a significant role as a rate-determining step [8–10, 154–157].

C–H bond activation and the DH process on transition metal (TM) surfaces have been widely investigated for light alkanes, both experimentally and theoretically. For instance, the activation of methane under moderate conditions was only observed on oxygen-pre-covered Cu surfaces, and by using DFT calculations, it was shown that the activation energy of methane is decreased by using promoters such as O*, OH*, O_2*, and OCH_3 [158–161]. Promoters for methane activation have also been evaluated on Pd and Au as well as their alloys [162, 163]. Alkane DH has been studied primarily on Pt catalysts for the non-oxidative process, and investigations targeted Ni and Pd for the ODH process [9, 23, 26, 27, 51, 54, 126, 164–168]. The direct dissociative chemisorption of propane and *iso*-butane and their fully deuterated isotopes was studied on the Pt(110) surface, where it was found that the difference in activation energies of C–H and C–D bond cleavage can be attributed to differences in zero-point energy stemming from the two isotopes [169–171].

The combination of explicit DFT calculations and simple modeling methods such as scaling relationships has proven to be an essential tool in the computational search for new and promising catalysts [44, 45, 47, 68, 172]. The scaling relationships can be viewed as the correlation between a descriptor and the transition-state (TS) energy of a specific reaction [66, 67, 173–177], with descriptors typically being the final-state (FS) or adsorption energies of one or a few key intermediates [45, 178, 179]. For the C–H bond activation and (de)hydrogenation reactions of alkanes several scaling relationships have been proposed [8, 9, 47–50, 59, 134, 146, 150, 168, 173, 180–182]. One of the first attempts to generalize a set of de(hydrogenation) reactions for several reactants including methane, ethane, and propane over close-packed and stepped surfaces of TMs was proposed by Wang et al. [150] Therein, with a suitable choice of reference systems, the transition state scaling relationship was approximated to just one single linear scaling relationship (LSR). LSRs between the final state energies and the corresponding transition state energies have been used to understand the effect of co-adsorbed species on metal surfaces. For instance, it was found that the X–H bond activation (with X=C, N, O, S) does not only depend on the binding strength of the X/X–H species, but also of the H atom being extracted during X–H bond activation [48–50, 182]. Based on trends observed for the C-H bond activation of methane on TMs it has been possible to understand the origin of the promoting/poisoning effect of non-metals (B, C, N, P, O, S, and Se) and to describe the C–H, N–H, and O–H bond activation across a range of reactions [146]. Other LSR studies include methane activation on single-atom alloys [52] and the C–H bond activation of the non-oxidative dehydrogenation of ethane and propane on TMs [8, 9, 134, 168].

For larger alkanes, the effect of co-adsorbed species such as oxygen and hydroxyl in the C–H bond activation on TMs surfaces has not been investigated in detail yet. In this paper, a systematic study of the first (oxidative) dehydrogenation step of light alkanes (ethane, propane, and *n*-butane) over close-packed and stepped TM surfaces (Scheme 4.1) has been performed using DFT calculations. As these (O)DH reactions can be catalyzed by a vast range of materials including noble metals and transition metal oxides, herein, the TMs most frequently used have been chosen: Ag, Au, Cu, Ni, Co, Pd, Rh, and Pt.

4.2. Computational Details

DFT calculations were carried out using the Vienna Ab Initio Simulation Package (VASP) [139, 140] and the Atomic Simulation Environment (ASE) [117] employing the generalized gradient approximation (GGA) Bayesian error estimation functional with van der Waals corrections (BEEF-vdW) [104, 141] and the projector-augmented wave (PAW) potentials [115, 116]. A similar setup, as well as, the reference energy levels for the final states (FS) and the transition states (TS) of the LSR are defined as in the previous chapter, where the gas-phase molecules (ethane, propane or *n*-butane) and the TM surfaces (with or without the preadsorbed oxygen species) were taken as the reference. When specified, single-point calculations were performed using the PBE functional, including Grimme's dispersion corrections (PBE-D3) using the same parameters [103, 142]. The transition state (TS)

Scheme 4.1. (a) Overview of reaction pathways for the non-oxidative (green), O-assisted (blue), and OH-assisted (red) DH of alkanes, and (b) Illustration of the first (O)DH step of propane on close-packed (top) and stepped (bottom) TM surfaces
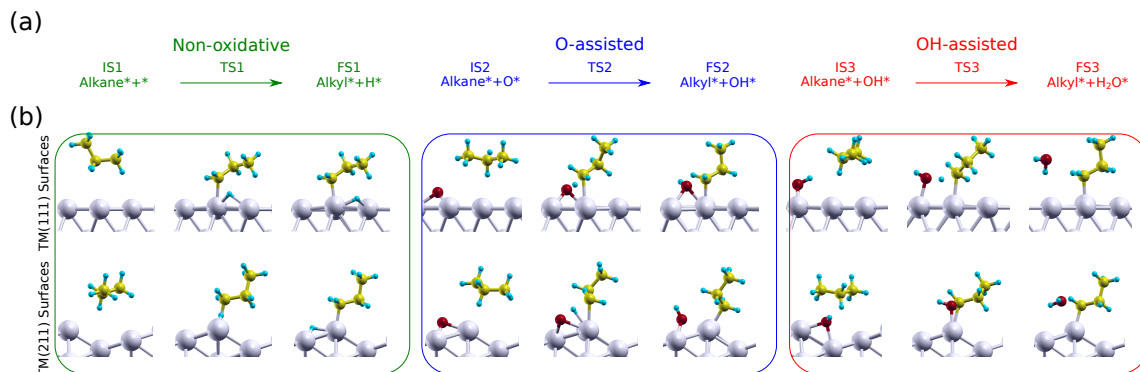
searches along the reaction path were systematically performed using the nudged elastic band (NEB) [119] and DIMER [121] methods at the same theoretical level as those for the reactants and products. A single imaginary frequency along the reaction coordinate confirmed the final TS structures, the frequencies were calculated with a normal mode analysis by using a finite-difference approximation of the Hessian matrix.

The lattice constants of the all transition metal (TM) bulks have been optimized with BEEF-vdW functional using 450 eV and 21×21×21 as the energy cutoff and k-point sampling, respectively. The lattice constants are in good agreement with the experimental values, as shown in Table 4.1). For the (O)DH of ethane and propane, a four-layer slab with a p(3×3) and p(1×3) supercells (with k-point meshes of 4×4×1) are used to represent the TM(111) and (211) surfaces, respectively. As reported previously, the difference in energy (for the adsorptions and transition states of C3 species) between supercells of different sizes are negligible, therefore the smaller supercells (3×3) are used.1 In the case of the (O)DH of n-butane, a (4×4) supercell (with a k-point mesh of 3×3×1) of the TM(111) surface is used. For all the calculations a kinetic energy cutoff of 450 eV was used and the two bottom layers of the slabs were fixed during the relaxations. Geometry optimization and transition state searches were conducted until the forces on each atom were below 0.01 eV/Å. In order to avoid interaction between periodic images, the TM slabs are separated by ~15 Å of vacuum along the z-direction. Only the surfaces involving Ni and Co were computed including spin-polarization.

Table 4.1. Optimize lattice parameters of the TM bulks

	a [Å]			a [Å]	
	Calc.	Exp.		Calc.	Exp.
Ag	4.202	4.069 [183]	Co	3.531	3.544 [184]
Au	4.208	4.078 [185]	Pd	3.979	3.878 [186]
Cu	3.658	3.603 [183]	Rh	3.847	3.789 [183]
Ni	3.534	3.517 [187]	Pt	3.994	3.924 [185]

41

The reference systems used for the calculations of the adsorption, activation, initial, transition, final state, and D3 contribution energies were presented in section 2.10, including the methods used for the transition state searching and how the contributions to the free energy were calculated.

An analysis for validation of the statistical significance and physical meaning of the parameter estimates was performed, as explain by Toch et al. [188] The significance of every individual parameter was tested employing a t-test, as well as, the 95% confidence intervals (CI), mean absolute error (MAE), and maximum residual error were calculated.

In the previous chapter the dehydrogenation of propane over Pd(111) and Pd(211) surfaces and the effect of promotion with surface oxygen and hydroxyl was investigated. It was found that the transition state energies (ΔE_{TS}) scale linearly with the final state energies (ΔE_{FS}), for both the non-oxidative and the oxidative dehydrogenation steps. Herein, this analysis is extended to the first (O)DH step of ethane, propane, and n-butane over a range of TM surfaces.

4.3. Nonoxidative Dehydrogenation of Ethane on Transition Metal Surfaces

Figure 4.1 shows the linear relationship between the ΔE_{TS} for the first DH step of ethane following the non-oxidative pathway, and the corresponding ΔE_{FS} on several TM(111) and (211) surfaces relative to gas-phase ethane. The calculated ΔE_{TS} range from 0.37 eV (Pt) to 2.28 eV (Ag), and the energy barriers to activate the adsorbed molecules (initial state, IS) are in fair agreement with recent reports for Pt, Ni and Cu surfaces [13, 51, 164, 168, 189–191]. Comparing the (111) to (211) surfaces (with the intercepts being different by app. 0.1 eV) a weak geometric effect is observed, which is in line with other studies on dehydrogenation reactions [150, 192] and also points to the reaction being rather surface insensitive (see Figure 4.2a for a more quantitative analysis of the scaling relations).

4.4. Oxidative Dehydrogenation of Ethane on Transition Metal Surfaces

Transition state scaling relationships (similar to those obtained for non-oxidative DH) are observed for the oxygen and hydroxyl assisted DH of ethane, as shown in Figure 4.3. Overall, the results presented here for the TM(111) surfaces are in line with what has been found previously for methane activation assisted by oxygen and hydroxyl species [48–50, 146, 182]. For the first ODH step of ethane on O- and OH- modified surfaces, the ΔE_{TS} are directly correlated with the oxygen/hydroxide adsorption energies (Table 4.2 and Figure 4.4). Generally, it is found that metals that adsorb the oxygen and hydroxide species strongly, such as Co, Cu, and Ni, have higher ΔE_{TS}. For metals with weak adsorption
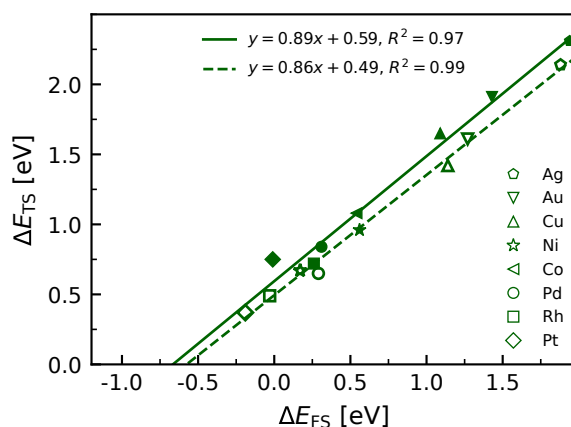
Figure 4.1. Transition state energies as a function of the final state energies for the non-oxidative DH of ethane on TM surfaces. Filled and open markers correspond to TM(111) and (211) surfaces, respectively.
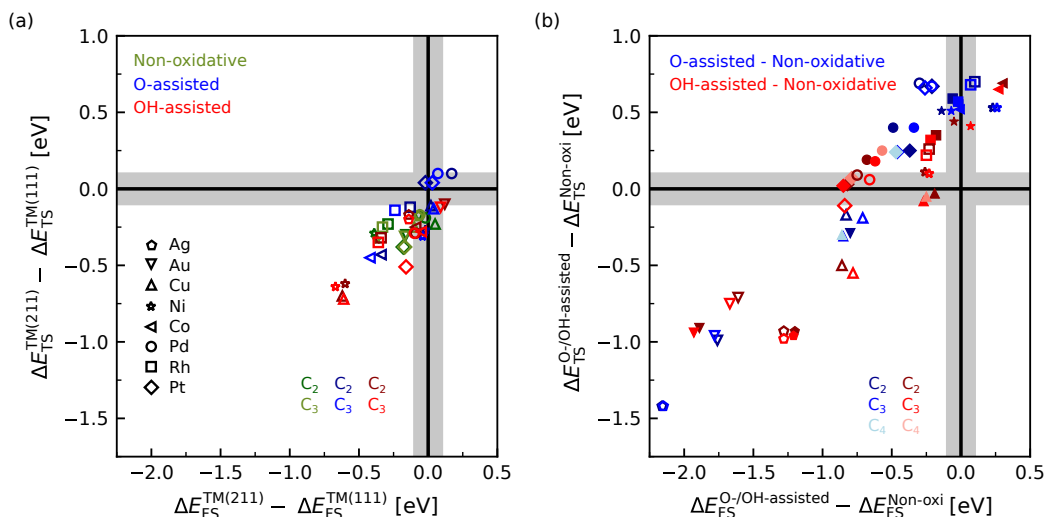
Figure 4.2. (a) Difference between the ΔE_{TS} of the alkane C−H bond activation on TM(211) and TM(111) surfaces as a function of its ΔE_{FS}. (b) Difference in ΔE_{TS} between the O-/OH- assisted and the non-oxidative DH of alkanes as a function of its ΔE_{FS}, filled and open markers correspond to TM(111) and (211) surfaces, respectively.

energies such as Au, Ag and Pt it is observed a much lower ΔE_{TS} compared to the non-oxidative pathway and hence a strong promotional effect of O* and OH* (see also Table 4.2 and Figure 4.4 for all metals).

Regarding the effect of under-coordinated surface sites such as steps and kinks, as can be seen in Figure 4.2a, the O-assisted DH on Co and Rh on the (211) surface is more favorable than on the (111) terrace. The same effect is seen for the process with the assistance of co-adsorbed OH on Cu, Ni, Rh, and Ag. In this figure, a gray area of ±0.1 eV has been included to indicate energy differences that are below the accuracy of our calculations
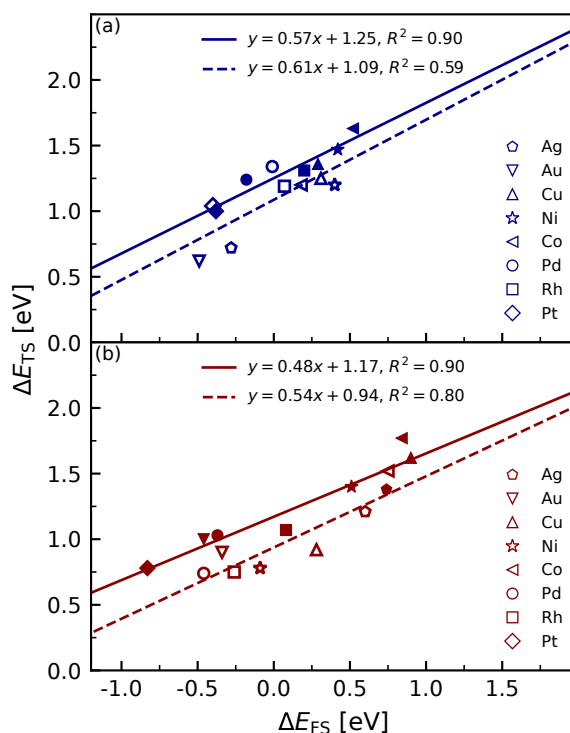
Figure 4.3. Transition state energies as a function of the final state energies for the (a) O- and (b) OH-assisted dehydrogenation of ethane on TM surfaces. Filled and open markers correspond to TM(111) and (211) surfaces, respectively.

Table 4.2. Adsorption energies (in eV) of oxygen species on TM surfaces. Molecular oxygen[a] and hydrogen/water[b] in the gas phase were taken as the reference point for atomic oxygen and hydroxyl, respectively.

	O		OH	
	TM(111)	TM(211)	TM(111)	TM(211)
Ag	-0.34 (hcp)	-0.20 (th1)	+0.48 (fcc)	+0.42 (s4)
Au	+0.25 (hcp)	+0.09 (sb)	+1.26 (hcp)	+0.99 (sb1)
Cu	-1.48 (hcp)	-1.49 (tf2)	+0.04 (fcc)	+0.21 (sb1)
Ni	-2.10 (hcp)	-2.08 (tf2)	+0.02 (bridge)	+0.02 (sb1)
Co	-2.40 (hcp)	-2.27 (tf2)	-0.33 (fcc)	-0.84 (sb)
Pd	-1.03 (hcp)	-1.17 (tf2)	+0.63 (bridge)	+0.60 (sb1)
Rh	-1.89 (hcp)	-1.78 (tf2)	+0.17 (bridge)	+0.11 (sb1)
Pt	-0.72 (hcp)	-0.93 (tf2)	+0.82 (bridge)	+0.74 (sb1)

[a] $E_O = E_{O+surf} - E_{O_2}/2 - E_{surf}$
[b] $E_{OH} = E_{OH+surf} - E_{H_2O} + E_{H_2}/2 - E_{surf}$
Adsorption sites are abbreviated as: **hcp**, **fcc**, and **bridge** for terrace surfaces. **th1** hcp hollow site between terrace1 and terrace2; **sb** bridge site parallel to step edge; **tf2** fcc hollow site between terrace2 and step edge; **s4** fourfold hollow site in step; **sb1** bridge site perpendicular to step edge for stepped surfaces. See previous chapter and Orita et al. [143] for more details.

[105, 106, 193]; (among those are Ni, Cu, Pt, and Pd for O-assisted, and Pd, Co, and Au for OH-assisted). For Au(111) and Ag(111), the LSR presented in Figure 4.3 and the calculated ΔE_{FS} were used to determine the ΔE_{TS}, which are around 1.0 eV, the ΔE_{TS} for the O-assisted DH of ethane on Ag and Au (211) surfaces, on the other hand, are significantly lower.
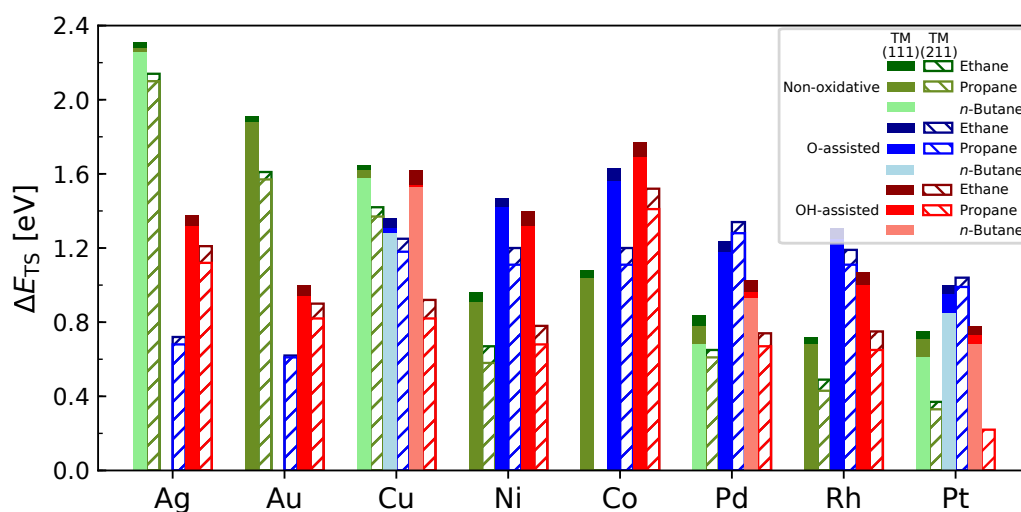
Figure 4.4. ΔE_{TS} for the (O)DH on TM surfaces.

The oxygen/hydroxyl species effect on each surface can be illustrated in a similar manner by analyzing the ΔE_{TS} difference between the O-/OH-assisted and the non-oxidative DH as a function of the difference in ΔE_{FS}, as shown in Figure 4.2b. An inspection of Figure 4.2b reveals that the C–H bond activation of ethane is significantly enhanced on coinage metals (Cu, Ag, and Au) by surface oxygen and hydroxyl species on both surfaces. On Ni, Co, and Rh, the strong oxygen and hydroxide adsorption energies seem to poison the surfaces, increasing the ΔE_{TS} and the ΔE_{FS}. For those metals, dehydrogenation is more favorable in the absence of adsorbed oxygen and hydroxide adsorbed species. This effect has been showed previously by Tsai et al. [146] for methane activation, where the electronic structure of the surface and the bond order of the promoter were found to establish the trends in bond activation. For Pd and Pt, on the other hand, the ΔE_{TS} for the O- and OH-assisted DH of ethane are higher than those for the non-oxidative DH, although the ΔE_{FS} are lower and stabilized by surface oxygen and hydroxyl species. In absolute terms, as expected from its use in commercial PDH technologies, Pt is calculated to perform best for the non-oxidative C-H bond activation of ethane, although it has quite favorable energetics for the ODH of ethane (both O- and OH-assisted) as well. From a statistical point of view, so far there is no strong motivation for the use of two separate LSRs for the (111) and (211) surfaces in each reaction pathway, because the combine LSRs for both surfaces are statistically significant. A detailed analysis can be found in the section 4.6.

4.5. (Oxidative) Dehydrogenation of Alkanes on TM Surfaces

Next, until what extent the (O)DH of propane and *n*-butane are similar to that of ethane is investigated. Figure 4.5 shows the energy diagram of the first DH step of ethane, propane,

and *n*-butane over the Pt(111) surface. The initial (ΔE_{IS}), transition (ΔE_{TS}), and final (ΔE_{FS}) state energies decrease as the chain length of the reactant increases in all reaction pathways; this interesting fact was pointed out before from non-oxidative DH experiments of propane and iso-butane on Pt(110) [169–171]. In those experiments, a systematic decrease in activation energy of the DH of alkanes as well as their fully deuterated isotopes was found.
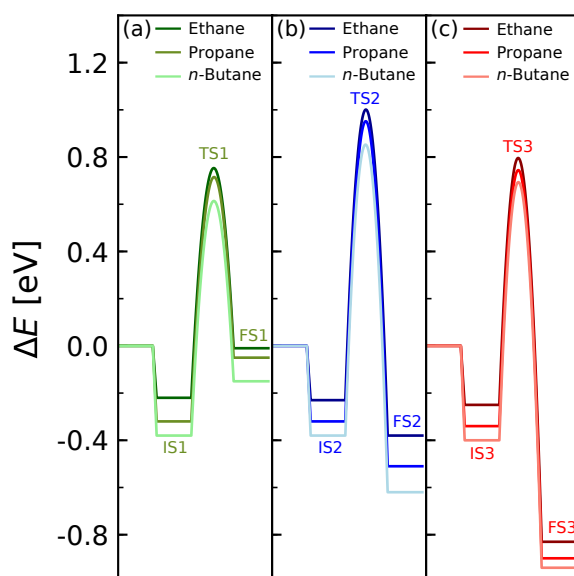
Figure 4.5. Potential energy diagram including initial, transition, and final states of the first dehydrogenation step of light alkanes on Pt(111) surface: (a) non-oxidative, (b) O-, and (c) OH-assisted pathways.

Table 4.3 shows the ΔE_{TS} of the alkane C-H bond activation and the dispersion interactions between the TS of the alkanes and the Pt(111) surface, as well as their average differences to those of ethane. The vdW forces were obtained through single-point calculations using the PBE-D3 functional and subtracting D3 contributions of surface species from those of gas-phase molecules. These calculations reveal that the D3 contributions of the TS increase as a function of the carbon-chain length, and that differences in these contributions correspond approximately to the ΔE_{TS} changes of the corresponding TS.

Table 4.3. TS Energies and D3 Contributions (with Respect to the Gas-Phase Values) for the (O)DH of Alkanes on the Pd(111) Surface

		non-oxidative	O-assisted	OH-assisted	average diff*
Ethane	ΔE_{TS}	0.75	1.00	0.78	
	E_{disp}	-0.56	-0.59	-0.57	
Propane	ΔE_{TS}	0.71	0.95	0.73	-0.05
	E_{disp}	-0.62	-0.66	-0.64	-0.07
n-Butane	ΔE_{TS}	0.61	0.85	0.68	-0.13
	E_{disp}	-0.80	-0.71	-0.68	-0.16

*Differences with respect to ethane values

As the differences in the energies shown in Table 4.3 can mainly be ascribed to the size of the reacting molecule, one might expect a similar result for all other TM surfaces studied

in this work. Indeed, this is observed in Figure 4.6, where the calculations are extended to propane (O)DH on TM(111) and (211) surfaces, and *n*-butane (O)DH on Pd, Cu, and Ag (111) surfaces. As shown in Figure 4.6a andc, the ΔE_{TS} of propane and n-butane are linearly correlated with the ΔE_{TS} of ethane regardless of the TM surface and promoter present (oxygen or hydroxyl). The resulting intercepts (-0.06 and -0.10 eV) are in line with the average values of the differences in ΔE_{TS} between propane/*n*-butane and ethane being -0.06 and -0.11 eV, respectively (Figure 4.6b and d). These values compare quite well with the average differences in dispersion contributions (the D3 part) between propane/*n*-butane and ethane, which are -0.07 and -0.19 eV. Therefore, the difference in ΔE_{TS} between alkanes is mainly attributed to their differences in dispersion contributions dictated by the carbon-chain length.

Figure 4.6. Linear correlation between the ΔE_{TS} of the first (O)DH steps of (a) propane-ethane and (c) *n*-butane-ethane on TM surfaces. Changes in ΔE_{TS} and dispersion contributions of the TS between (b) propane-ethane and (d) n-butane-ethane for the non-oxidative, O-, and OH-assisted DH on TM surfaces. The dashed lines represent the intercepts of the equations in (a) and (c).

The general correlations found between the ΔE_{TS} and ΔE_{FS} for all reactants and metal surfaces studied in the non-oxidative, oxygen- and hydroxyl-assisted DH are shown in Figure 4.7. In addition to our calculated data for ethane, propane, and *n*-butane, the values for the activation of methane on TM(111) surfaces from earlier work [49] are included. These general LSRs for alkanes are very similar to those obtained earlier for only ethane (see Figures 4.1 and 4.3), even when a different functional (such as RPBE) [151] was used for the methane data. This is rationalized by a more or less equal shift of $\Delta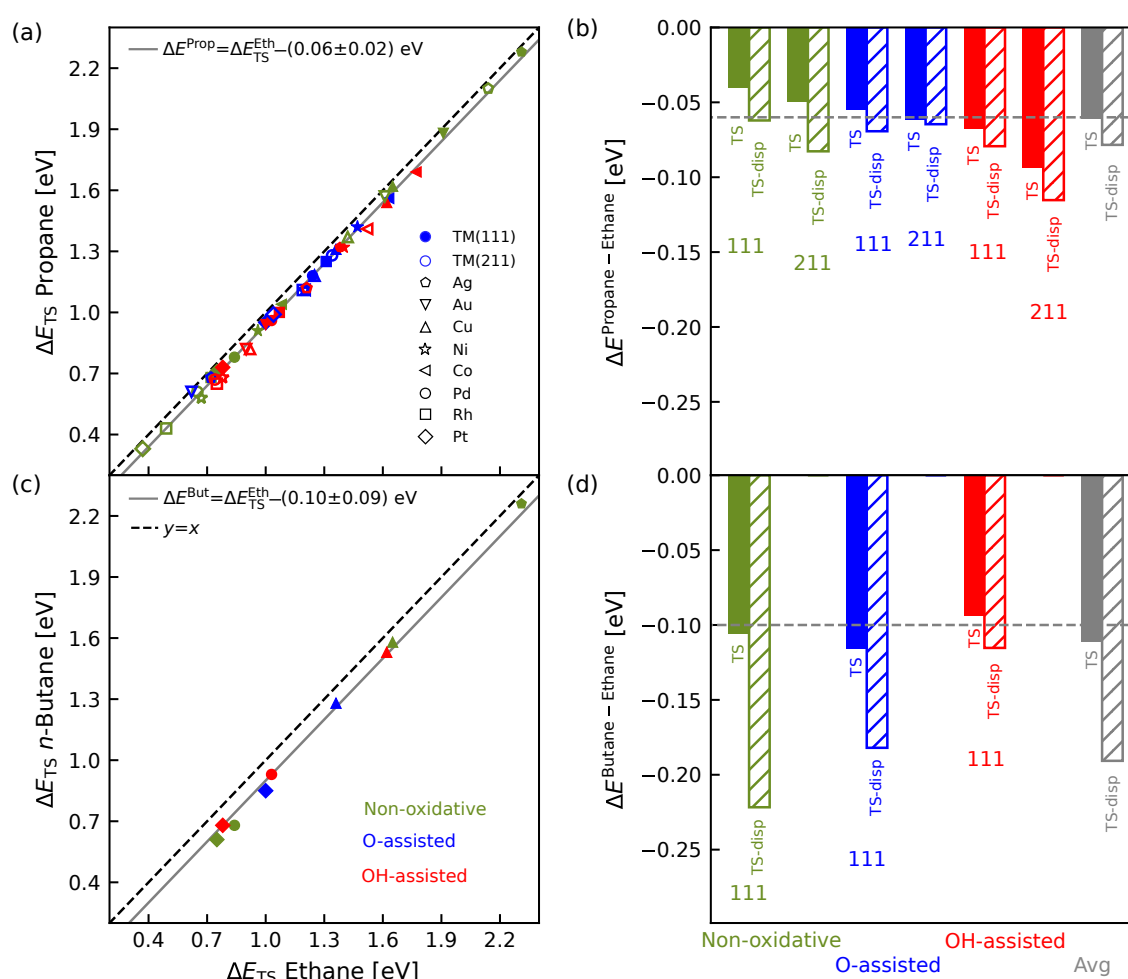 E_{TS}$ and ΔE_{FS} by the dispersion contributions resulting in all data points coinciding on the same scaling line. Therefore, conclusions drawn earlier on TM surfaces and surface geometries in ethane (O)DH can be easily extended to methane, propane, and *n*-butane, showing that the C−H bond activation for each studied alkane is affected in a similar way by surface oxygen/hydroxyl species. Importantly, the slopes of the LSR for non-oxidative DH are slightly lower than 1, while the slopes for the oxygen and hydroxyl assisted DH are all in the range of 0.5 − 0.6. This can be related to simple bond-counting arguments, with the oxygen (and hydroxyl) bond to the TM surface weakened upon abstraction of a hydrogen from the reacting alkane. The scaling relations for all (O)DH pathways were obtained across various TM surfaces and include different reactants, and could therefore be considered as predictive models for alkane C−H bond activation on metal surfaces. This is demonstrated in Figure 4.8 which shows a parity plot between our model based on the scaling relations from Figure 4.7 and the actual DFT data. Quite remarkably, the model agrees well with the DFT data leading to a MAE of only 0.08 eV. Complementarily, an in-depth statistical analysis was performed showing the significance of established scaling relations for the full data-set. It was found that the use of individual scaling relations per surface provided a better representation of the results obtained. A more extended discussion of the statistical analysis can be found in the next section. Therefore, our model is suggested for the initial screening of transition metal surfaces for alkane DH in the presence or absence of oxygen promoters.

4.6. Statistical Analysis of Data

The initial statistical analysis of the LSR obtained for the O(DH) of ethane (see Table 4.4 shows that despite parameters differentiating for each surface (especially the intercepts), some of the values for the slopes might be within the CIs. For the non-oxidative DH of ethane, the slopes and intercepts are within the confidence interval 95% (CI) of the parameters, and if a single LSR is used for both TM surfaces, the obtained MAE is only 0.08 eV with a maximum deviation of 0.21 eV. When a single line is used for the scaling relationships, in the case of the O-assisted DH, the maximum error slightly increases to 0.25 eV, and the *t*-, *p*-values, and R^2 adopted intermediate values compared to those for the individual functions. For the OH-assisted DH, if a single line is used for the TM(111) and (211) surfaces, despite that, the CIs are low, and the *p*-values increase, the R^2, MAE and maximum deviation deteriorate. The LSRs for each surface will be further discussed in the next sections.
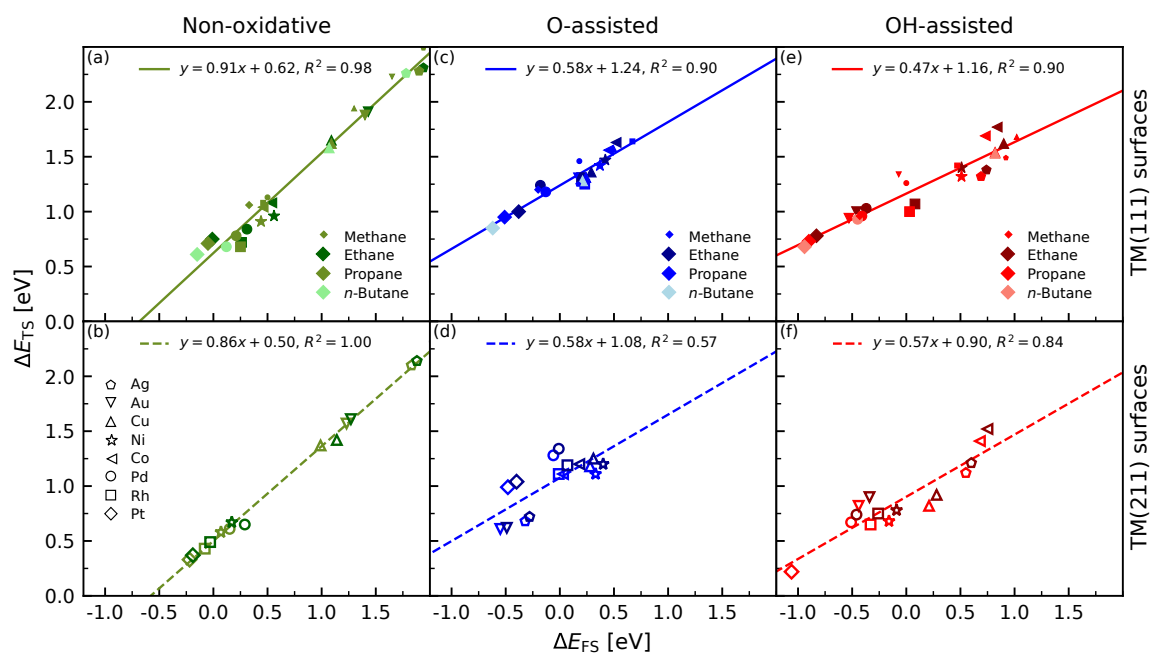
Figure 4.7. Transition state scaling relationships for the C−H bond activation of methane, ethane, propane, and *n*-butane for (a, b) non-oxidative, (c, d) O-, and (e, f) OH-assisted reaction pathways on transition metal surfaces. A detailed statistical analysis of the LSR is given in the next section. Small markers for methane activation were taken from Yoo et al. [49]
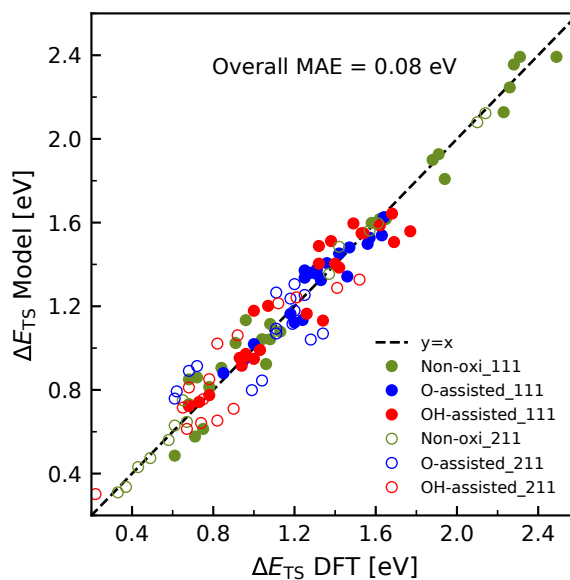
Figure 4.8. Parity diagram for the accuracy of the models. Calculated DFT ΔE_{TS} compared with the predictions from our models presented in Figure 4.7 for the (O)DH of alkanes on TM surfaces.

Bringing back the discussion about the use of a single or two LSRs for the alkane (O)DH process over both surfaces, (111) and (211), Table 4.5 shows the CIs of the intercepts and

Table 4.4. Statistical analysis of the scaling relationships for ethane (O)DH

		Variable	Conf. Int.	*t*-value	tab.95 *t*-value	*p*-value	R^2	MAE	Max dev	Data points
				Non-oxidative DH						
TM(111)	slope	0.89	0.12	14.95	1.76	5.6E-06	0.97	0.07	0.16	8
	intercept	0.59	0.11	10.10		5.5E-05				
TM(211)	slope	0.86	0.06	29.05	1.78	9.1E-07	0.99	0.04	0.09	7
	intercept	0.49	0.06	17.23		1.2E-05				
TM(111)/	slope	0.88	0.07	22.07	1.70	1.1E-11	0.97	0.08	0.21	15
TM(211)	intercept	0.54	0.07	13.92		3.5E-09				
				O-assisted DH						
TM(111)	slope	0.57	0.20	5.97	1.81	4.0E-03	0.90	0.06	0.09	6
	intercept	1.25	0.07	36.88		3.2E-06				
TM(211)	slope	0.61	0.40	2.97	1.86	2.5E-02	0.59	0.13	0.24	8
	intercept	1.09	0.12	17.02		2.4E-06				
TM(111)/	slope	0.66	0.23	5.07	1.76	2.8E-04	0.68	0.12	0.25	14
TM(211)	intercept	1.15	0.08	26.92		4.2E-12				
				OH-assisted DH						
TM(111)	slope	0.48	0.13	7.23	1.86	3.6E-04	0.90	0.08	0.19	8
	intercept	1.17	0.08	27.02		1.7E-07				
TM(211)	slope	0.54	0.24	4.48	1.89	6.5E-03	0.80	0.11	0.18	7
	intercept	0.94	0.11	17.27		1.2E-05				
TM(111)/	slope	0.52	0.14	6.49	1.75	2.0E-05	0.76	0.14	0.28	15
TM(211)	intercept	1.06	0.08	23.39		5.2E-12				

slopes, *t*-values, *p*-values, MAE and maximum deviation for the C−H bond activation of alkanes in the two cases: individual LSRs for each surface (TM(111) and (211)) or a combined LSR for the TM(111)/TM(211) surfaces. For the non-oxidative DH of alkanes, all the CIs have become narrower, and now the individual lines do not cross each other anymore; all the parameters are estimated to be significant, proven by the t-values obtained for the three cases. As a consequence, the three scaling relationships (one for each surface, and one LSR for the combined surfaces) differ mainly in the intercept, while the slopes are determined by bond-counting. Although the use of just a single LSR provides good performance, the maximum deviation obtained is slightly higher when using individual scaling relationships. Hence, it is preferred to use a single scaling relationship for each surface, as shown in Figure 4.7a-b, however the LSR combined for both surfaces is nonetheless statistically significant. In the case of the O-assisted DH of alkanes on the (111) surfaces (Figure 4.7c), after the inclusion of data for methane, propane, and *n*-butane, the CIs of the fitting parameters improve considerably, with calculated *t*-values higher than the tabulated *t*-values (Table 4.5). Due to the small range of values calculated for the O-assisted DH on TM(211) surfaces (Figure 4.7d), a rather large scattering of data points is observed as it is evident from the low R^2 coefficient of 0.57, the large maximum deviation of 0.25 eV, and also the smaller CIs obtained (Table 4.5). Hence, the interpretation of these data should be done with care. As it was pointed out earlier, if just a single scaling relationship is used for both surfaces in O-assisted C−H bond activation, the R^2 and the maximum deviation deteriorate badly, with values of 0.72 and 0.28 eV, respectively. The use of just a single LSR for the O-assisted DH of alkanes for both surfaces is not recommended. The OH-assisted DH of alkanes is very well described by the two LSR model system (Figure 4.7e-f), the values obtained from the statistical analysis (Table 4.5) show superior performance compared to the single

(111) and (211) surface models. However, a unique LSR is not recommended in view of the lower R^2 and the larger maximum deviation.

Table 4.5. Statistical analysis of the scaling relationships for alkane (O)DH

		Variable	Conf. Int.	t-value	tab.95 t-value	p-value	R^2	MAE	Max dev	Data points
				Non-oxidative DH						
TM(111)	**slope**	0.91	0.05	31.70	1.68	4.2E-21	0.98	0.08	0.17	26
	intercept	0.62	0.05	20.81		7.3E-17				
TM(211)	**slope**	0.86	0.03	59.67	1.71	3.2E-16	1.00	0.03	0.10	14
	intercept	0.50	0.02	36.57		1.1E-13				
TM(111)/	**slope**	0.91	0.04	35.56	1.66	8.9E-31	0.97	0.09	0.19	40
TM(211)	**intercept**	0.57	0.04	22.27		2.1E-23				
				O-assisted DH						
TM(111)	**slope**	0.58	0.08	13.01	1.69	1.4E-10	0.90	0.05	0.12	20
	intercept	1.24	0.03	75.54		5.6E-24				
TM(211)	**slope**	0.58	0.24	4.30	1.70	7.3E-04	0.57	0.13	0.25	16
	intercept	1.08	0.07	25.41		4.1E-13				
TM(111)/	**slope**	0.64	0.12	9.31	1.67	7.1E-11	0.72	0.11	0.28	36
TM(211)	**intercept**	1.16	0.04	48.63		5.1E-33				
				OH-assisted DH						
TM(111)	**slope**	0.47	0.06	14.13	1.68	8.0E-13	0.90	0.07	0.21	25
	intercept	1.16	0.04	53.79		1.1E-25				
TM(211)	**slope**	0.57	0.12	8.36	1.70	1.4E-06	0.84	0.11	0.20	15
	intercept	0.90	0.06	26.05		1.3E-12				
TM(111)/	**slope**	0.53	0.08	11.55	1.66	5.4E-14	0.78	0.14	0.35	46
TM(211)	**intercept**	1.06	0.05	38.44		5.0E-32				

4.7. Chapter Conclusions

The first (oxidative) dehydrogenation step of light alkanes (ethane, propane, and n-butane) on transition metal closed-packed and stepped surfaces were analyzed using DFT calculations. It was shown that the transition state energies (ΔE_{TS}) of the C−H bond activation scale linearly with the corresponding final state energies (ΔE_{FS}), and all alkanes studied (including methane) share the same linear relationships (LSR) for the non-oxidative, O-assisted, and OH-assisted reactions. This is because the ΔE_{TS} and ΔE_{FS} of the alkanes are equally shifted by the dispersion interactions with the transition metal surfaces. Variations in ΔE_{TS} between alkanes were primarily attributed to differences in dispersion contributions determined by the carbon-chain length. As the carbon chain increases, the ΔE_{TS} of the alkane C−H bond activation decreases. As a result, the ΔE_{TS} of the first (O)DH steps of propane and *n*-butane are linearly correlated with the ΔE_{TS} of ethane and it is expected that this also applies to longer alkanes.

The current analysis also evaluated the impact of oxygen and hydroxyl adsorption on the transition metal surfaces on promoting (e.g., for Au and Ag) and poisoning (e.g., for Co, Ni and Rh) the reaction. Finally, it is shown that simple models based on the LSRs are able to predict ΔE_{TS} with a minimal MAE for a wide range of metals, alkane reactants and DH pathways. It is suggested that these LSRs are universal and can therefore pave the way towards the computational design of improved (O)DH catalysts.

5. Universal Linear Scaling Relationships for the C–H Bond Activation of Alkanes on Metal Oxides and Single-atom-doped Metal Oxides

5.1. Introduction

Industrial research has driven the search for new and more effective catalysts as there is still a large window to improve their selectivity and stability, mainly due to the cost and environmental issues of the Pt- and CrO_x-based catalysts[1, 5]. Considering the first dehydrogenation step as the rate-limiting step [39], the main challenge is controlling the consecutive oxidation of alkanes/alkenes to CO_x due to the much higher reactivity of products than the reactants. Here, the C-H bond activation plays a critical role and how to activate this bond selectively is of prime interest. On metal catalysts, the C–H bond cleavage might occur via three reaction pathways, the non-oxidative, O-, and OH-assisted activation [49]. Several comprehensive reviews on methane, ethane, and propane conversion over metal-based catalysts can be found in the literature [1, 15, 18].

Moreover, some metal oxides (MOs) such as Ga_2O_3 [39, 63, 194], V_2O_3 [195], IrO_2 [59, 196], ZrO_2 [34, 35, 37], and CeO_2 [64, 197] are promising candidates for alkane C–H bond activation at low and high temperatures, depending on the reaction of interest. The promising MO catalytic properties have been attributed to their inherent Lewis acidity and basicity, among other physical-chemistry properties. Historically, there are several accepted definitions and classifications of Lewis acid-base pairs; here, the one proposed by Metiu et al. [60] using Bader charges is taken: in a reaction, the Lewis acid gains Bader charge, while the Lewis base loses it, in line with the generally accepted concept where a molecule whose electron charge increases during a reaction is a Lewis acid, and the one that loses electrons is a Lewis base. Previous studies have proposed that the active-sites responsible for the C–H bond activation are the metal cation and neighboring lattice oxygen or the metal cations located at an oxygen vacancy [34, 35, 39, 198]. From a theoretical point of view, two types of transition state (TS) structures have been proposed; one resembles the final state co-adsorbed structures, and another has a radical-like transition state structure [15, 60, 69]. Furthermore, the catalytic properties of MOs can be enhanced by doping the structures (with a transition metal (TM) such as Pt, Pd, Au, Ni, Co, and more) by either adsorption, insertion, or substitution [199–202], generating

---

so-called single-atom catalysts (SACs). These SACs are highly dispersed systems with properties distinctly different from supported nanoclusters systems. However, these SACs are often rather unstable as their surfaces have a high surface free energy due to the low coordination environment, such that single atoms tend to migrate and aggregate to form clusters [200, 203]. Investigations of SACs need therefore be conducted carefully to confirm that the measured rates correspond to the SACs themselves rather than to the clusters formed during the reaction [204].

Consequently, several research efforts have been devoted to synthesizing thermally stable SACs combined with theoretical studies to predict and design new catalysts [15, 200, 205, 206]. For instance, Xiong et al., [41] showed that isolated Pt single atoms could be steadily trapped on CeO_2 catalysts, although the catalyst is non-selective towards propylene using propane as a feedstock. DFT calculations suggested that the strongly adsorbed propylene is expected to undergo further reactions, leading eventually to C – C bond cleavage. Nevertheless, if Sn is added to the Pt-SAC, undesired reactions are prevented. Consequently, a higher selectivity is obtained on the Pt–Sn–CeO_2 catalyst. In the same line, Zhu et al. have performed a series of studies on some of the most promising MOs and their SACs for the DHP. Using DFT calculations in conjunction with microkinetic analysis, several candidates have been identified and subsequently tested, with $Ir_1 – Ga_2O_3$ as one of the most promising candidates [39]. Additionally, individual linear scaling relationships (LSRs) to predict the TS energies using several descriptors have been proposed for most of the catalysts studied. For instance, for single-atom-doped Ga_2O_3, Chang et al. [39] established a correlation between the co-adsorbed 2-propyl and H (i.e., FS energy) at the M – O site with the TS energies of propane activation. On the other hand, Nørskov et al. [59, 207] choose the hydrogen affinity for the C – H bond activation on alkaline MOs and other classes of materials where the TS has a radical-like behavior. The established LSRs are, however, often specific for each MO and their corresponding doped systems [15, 57, 59, 65, 207].

Notably, the rapid development of structure-activity relationships (SAR) based on DFT data in recent years, combined with microkinetic models, makes it easier to address complex computational systems [39, 68, 208, 209]. These SARs are primarily linear and are widely used for TM surfaces; recently, their use for MO surfaces is also gaining importance [180, 210, 211]. These LSRs have been used for several reducible, irreducible oxides as well as promoted MOs. Unfortunately, these LSRs are limited by the investigated systems and descriptors used [207, 212–214]. Therefore, combining the LSRs for both radical and surface-stabilized transition states through a common descriptor for all the MOs and SACs could establish new guidelines for a rational screening and design of new catalysts systems.

In this chapter, a systematic study of the propane C – H bond activation over four of the most interesting MOs used currently (monoclinic-ZrO_2 ($mZrO_2$), tetragonal-ZrO_2 ($tZrO_2$), CeO_2, and MgO) and some of their single-atom-doped catalyst has been performed using DFT calculations. There is a vast range of dopants that can be potentially used; however, this work focus on Pt, Pd, and Au as these are the most common dopants used experimentally. As will be shown in the following sections, the behavior of these

oxides surfaces can be explained based on their Lewis acid-base properties [60, 69]. These calculations are complemented with data obtained from previous studies on the C – H bond activation of light alkanes over MOs and SACs of industrial interest. The correlations for the transition state energies established here are expected to pave the way toward the computational development of new and better catalysts guiding future experiments as a first-hand tool in heterogeneous catalysis.

5.2. Computational Details

DFT calculations were carried out using the Vienna Ab Initio Simulation Package (VASP) [139, 140] and the Atomic Simulation Environment (ASE) [117] employing the generalized gradient approximation (GGA) using the Bayesian error estimation functional with van der Waals corrections (BEEF-vdW) [104, 141] and the projector-augmented wave potentials [115, 116]. For all calculations, a kinetic energy cutoff of 450 eV (including spin-polarization) was used and the Brillouin zone was sampled using a Monkhorst-Pack sampling. The unit cell size, the k-point numbers being specified in Table 5.1. Additionally, the number of units keeps fixed at their crystal lattice positions while the adsorbate and the remainder of the slab were allowed to relax fully are in parenthesis. In order to avoid interaction between periodic images, a vacuum of 20 Å was used to separate successive slabs. In addition, a DFT+U approach with a U_{eff}-value of 5 eV was chosen for ceria [204]. To form the SACs, single-atom-doped MO (M_1–MO) surfaces were constructed by substituting a metal cation with dopants such as Pt, Pd, and Au; the calculations were performed using the same parameters as the ones used for the pristine surfaces. The single metal dopants were always substituted in the cation site of their host, as it has been proven to be the most convenient site before [215]. How the dopant binding, molecule adsorption, and oxygen vacancy energies were calculated are shown in section 2.10. By their definition, a negative value corresponds to an exothermic process.

Table 5.1. Surface, unit size cell, and k-point meshes used in the MO/SAC calculations

	Surface	Unit cell size	k-point mesh
$mZrO_2$	$\bar{1}11$	4×4×3(2)	2×2×1
$tZrO_2$	101	2×3×3(2)	2×2×1
CeO_2	111	3×3×3(2)	2×2×1
MgO	100	3×3×4(2)	3×3×1

The reference systems used for the calculations of the adsorption, activation, initial, transition, and final state energies were presented in section 2.10, including the methods used for the transition state searching and how the contributions to the free energy were calculated. The structures used to search the TS in each activation step were chosen based on the most stable adsorbed alkane structure over the MOs/M_1–MOs surfaces.

Finally, after an exhaustive search of DFT data for the C – H bond activation of alkane on MOs and SACs in the literature, the use of several functionals such as BEEF-vdW [15, 57, 62, 63, 65, 207, 216], PBE-D3 [196, 213, 217–222], PBE [34, 35, 37, 194–196, 220, 221, 223–227], PW91 [130, 198, 220, 228], optB88-vdW [217, 226], vdW-DF2 [229], and PBE-sol

[230] have been found. All our data and the values extracted from the literature have as the activate site either the metal cation and neighboring lattice oxygen or the metal cation at an oxygen vacancy, such that the alkyl group is mainly adsorbed in the cation, and the hydrogen forms an O – H bond with one of the surrounded oxygens of the active metal.

5.3. Characterization of MOs and M_1-MOs surfaces

In the previous chapter it was shown how light alkanes (methane, ethane, propane, and *n*-butane) share the same LSRs for the non-oxidative, O-, and OH-assisted C – H bond activation on TM surfaces. Herein, that is extended to MO and M_1 – MO systems. Calculations were performed for ZrO_2 (monoclinic and tetragonal phases), CeO_2, and MgO. Additionally, data from the literature were taken. Slab models were used to represent the monoclinic($\bar{1}$11) and tetragonal(101) surfaces of ZrO_2, the CeO_2(111), and the MgO(100) surfaces, as well as their corresponding M_1 – MOs systems. The periodic slab models of the MOs used in this study, including some lengths, are depicted schematically in Figure 5.1. The supercell size was chosen such that the biggest molecule studied (propane ~ 4.3Å) is not affected by its periodical image.

| (a) mZrO$_2$($\bar{1}$11) | (b) tZrO$_2$(101) | (c) CeO$_2$(111) | (d) MgO(100) |

10.92 Å — 14.65 Å; 9.65 Å — 12.62 Å; 9.73 Å — 11.63 Å; 8.93 Å — 9.04 Å
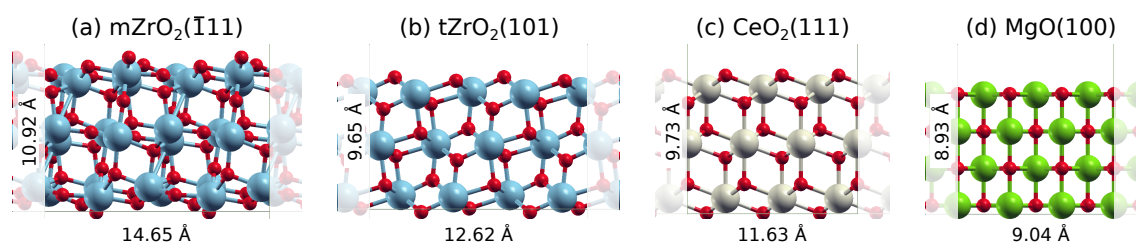
Figure 5.1. Side views of the (a) mZrO$_2$($\bar{1}$11), (b) tZrO$_2$(101), (c) CeO$_2$(111), and (d) MgO(100) surfaces.

The structural stability of all the M_1 – MOs surfaces is assessed by calculating the binding energy of a single dopant atom to the deficient cationic surfaces (see Eq. 2.40). The difference between their binding energies and the bulk cohesive energies measures how readily the single atoms can aggregate to form a metal cluster. As shown in Figure 5.2, in all the M_1 – MOs studied systems, the dopants have a more negative binding energy than their corresponding cohesive energy, where Pt has the lowest binding energies for mZrO$_2$, tZrO$_2$, CeO$_2$; and mZrO$_2$ forms the most stable SACs. This also applies to the defective systems, which still have a strong dopant biding energy, as shown in Figure 5.2. Besides, the dopants carry fewer positive charges than the metal on the pristine surface, causing the surfaces to be electron-deficient, and the substitution turns the surfaces into Lewis acids. Table 5.2 presents the effective Bader charges after the dopant substitution for each M_1 – MO system; as the dopants have lower valance electrons than the original surface cations, the neighbor oxygens lose their Bader charges.

For both systems (MOs and M_1 – MOs), the oxygen vacancy effect was also analyzed by removing an oxygen atom from the upper layer of the surfaces. In the case of the M_1 – MOs,
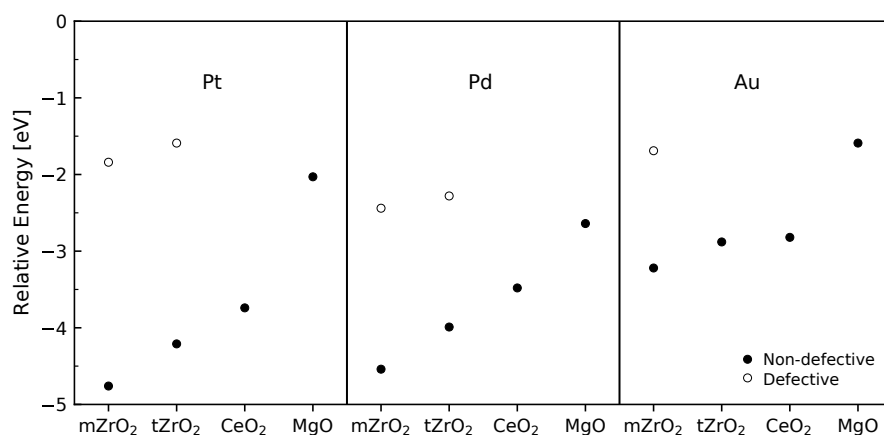
Figure 5.2. Difference between the binding energy of the dopants on MOs and its bulk cohesive energy. The dopant binding energies can be found in Table 5.3. The experimental cohesive energies were taken from Kittel [231].

Table 5.2. Calculated effective Bader charges on the MOs and $M_1 - MOs$ surfaces. M refers to the metal cation or dopant and O to the oxygen involved in the $C - H$ bond activation

		M	O
$mZrO_2$	Pristine	2.56+	1.17-
	def	2.16+	1.29-
	Pt	1.41+	0.94-
	Pd	1.30+	0.89-
	Au	1.26+	0.89-
$tZrO_2$	Pristine	2.60+	1.29-
	def	2.20+	1.31-
	Pt	1.38+	1.10-
	Pd	1.26+	1.09-
	Au	1.23+	1.04-
CeO_2	Pristine	2.38+	1.20-
	def	2.19+	1.22-
	Pt	1.38+	0.99-
	Pd	1.22+	0.98-
	Au	-	-
MgO	Pristine	1.66+	1.66-
	def	-	-
	Pt	-	-
	Pd	0.67+	1.44-
	Au	0.65+	1.44-

one of the dopant's neighbor oxygen atoms was selected. Under the definition of Eq. 2.41, the more positive the oxygen vacancy formation energy (OVFE), the higher the energy that is needed to form an oxygen vacancy, and hence the more stable is the doped surface. The calculated OVFEs are shown in Table 5.3. In the case of non-doped MOs, with ca. 6 eV, the two ZrO_2 phases have similar OVFEs and are the least reducible surfaces, and CeO_2 is the most reducible surface with 1.91 eV. Here the oxygen vacancy acts as a Lewis base [60], which donates electrons that are transferred to the cations of the oxide, as is shown in the Bader charge analysis in Table 5.2, where the effective Bader charge of the metals is lower

in the defective systems compared to the effective Bader charge on the pristine surfaces. In the case of the $M_1 - MOs$, the dopants facilitate the creation of oxygen vacancies, with $Au_1 - MOs$ having the smallest OVFEs. For the $M_1 - MgO$ systems, Pt and Pd have a similar effect on the reducibility of the surface. As all our dopants have a lower valance than the cations of the metal oxides, the electron deficit created with the substitution facilitates the generation of an oxygen vacancy, resulting in a considerable reduction of the OVFE.

Table 5.3. Oxygen vacancy formation energy and dopant biding energy on MOs and $M_1 - MO$ surfaces

	Dopant	ΔE_{bind}	OVFE
$mZrO_2$	-	-	6.03
	Pt	-10.60	1.38
	Pd	-8.43	0.56
	Au	-7.03	-0.01
$tZrO_2$	-	-	6.00
	Pt	-10.05	2.14
	Pd	-7.88	1.24
	Au	-6.69	0.87
CeO_2	-	-	1.91
	Pt	-9.58	0.68
	Pd	-7.37	0.35
	Au	-	-
MgO	-	-	6.31
	Pt	-7.87	4.15
	Pd	-6.53	4.15
	Au	-5.40	-

Finally, it is worth highlighting that all the dopants have positive charges, indicating a flow of electrons from the single atom to the surfaces, as indicated in Table 5.2. The substitution of a metal atom at the surface by a dopant makes the slab model non-stoichiometric and electrically charged; therefore, a charged compensation (for instance, with hydrogen) would be the most recommended path, but as has been discussed for ZnO [57], compensating the charges has a negligible or even negative effect on the structural stability of the doped systems. Hence, a non-compensating charge approach was taken for the C – H activation on the doped systems. As a final remark, in our study, for the non-defective cases, the M-O site (unless otherwise stated) was taken as the active site for the C – H bond cleavage. In the defective cases, either the M-O or M-sites were taken as the active sites, as specified for each case in Appendix A.

5.4. Adsorption Properties of MOs and M_1-MOs

Propane, propylene, and hydrogen adsorptions on the MOs and $M_1 - MOs$ of interest were calculated as a representation of the species involved during the dehydrogenation reaction (see Table 5.4). The calculations for the defective metal oxides (d-MOs) and the $M_1 - MOs$ were performed in the defect/dopant vicinity, and the adsorption energy (ΔE_{ads}) is calculated using the Eq. 2.39. As shown in Figure 5.3 for $mZrO_2$ and CeO_2 (non-defective, defective, and Pt-doped surfaces), the propane molecules are physisorbed, and the bond

lengths are almost the same in all the cases; on $tZrO_2$ and MgO surfaces similar results were found. These physisorptions are mainly due to dispersion forces; hence, the modification of the MO surfaces by either defects or dopants has almost no effect on the adsorption energy of propane, with adsorption energies being typically around -0.25 eV; a similar adsorption behavior on TM surfaces has been observed in the previous chapter.

Table 5.4. Adsorption energies of propane, propylene, and atomic hydrogen on the MOs and $M_1 - MOs$ surfaces. The reference values are the gas-phase molecules for propane and propylene, and H_2

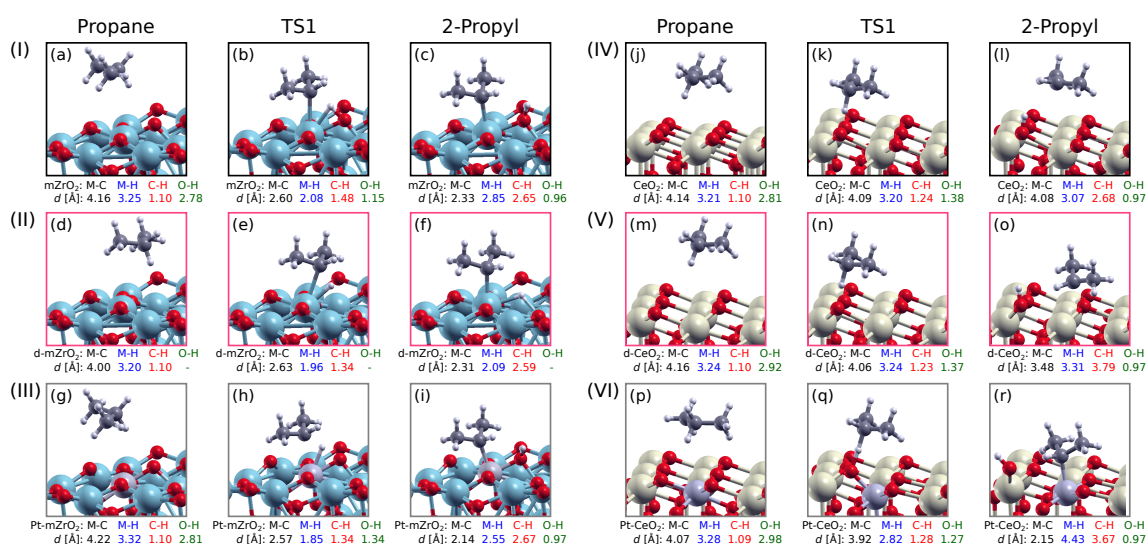|		ΔE_{ads}		
		Propane	Propylene	H
$mZrO_2$	Pristine	-0.21	-0.38	1.64
	def	-0.25	-0.70	
	Pt	-0.25	-0.46	-1.21
	Pd	-0.29	-0.29	-1.73
	Au	-0.26	-0.34	-1.93
$tZrO_2$	Pristine	-0.25	-0.33	1.00
	def	-0.25	-1.73	1.09
	Pt	-0.10	-0.26	-1.10
	Pd	-0.25	-0.30	-1.71
	Au	-0.26	-0.31	-2.01
CeO_2	Pristine	-0.25	-0.33	-1.63
	def	-0.14	-0.90	-1.79
	Pt	-0.27	-1.59	-1.73
	Pd	-0.27	-1.78	-2.15
	Au			
MgO	Pristine	-0.23	-0.27	1.70
	def			
	Pt	-0.20	-0.19	0.96
	Pd	-0.19	-0.19	0.50
	Au	-0.20	-0.18	-0.28

Figure 5.3. Geometries of the IS, TS, and FS structures for the C – H bond activation of propane on (I) $mZrO_2$, (II) d-$mZrO_2$, (III) $Pt – mZrO_2$, (IV) CeO_2, (V) d-CeO_2, and (VI) $Pt – CeO_2$.

Propylene has been suggested as a selectivity descriptor; the stronger the adsorption energy, the less selective the catalyst will be due to a drive toward further reactions such as C – C bond breaking and deep dehydrogenation [23, 134]. While the propylene molecule is physisorbed with adsorption energies around -0.35 eV (see Table 5.4), on pristine MO and most of the doped surfaces, the interaction between the surfaces and the propylene molecules is higher in comparison with propane adsorption and the average M – C distance is 3.7 Å compared to 4.1 Å for propane. In the case of doped-CeO_2, chemisorption is calculated to exhibit an aver4age M – C distance of 2.1 Å. The high adsorption energies of propylene on $Pt_1 – CeO_2$ and $Pd_1 – CeO_2$ (-1.59 and -1.79 eV, respectively) suggest a very low selectivity towards propylene, as has been shown in the previous studies [41, 64, 232]. This effect is rationalized based on the magnitude of the adsorption energies with the Lewis base character of the defective surfaces, where propylene acts as a moderate Lewis acid, generating chemisorptions with adsorption energies higher than 0.70 eV in all the cases.

The hydrogen adsorption could be indicative of propane activation as it has been previously established that there is a correlation between the hydrogen adsorption strength and the catalyst activity for C-H bond activation. While weak adsorption might hint at the C–H bond activation as the limiting step, a strong hydrogen binding energy might indicate that the reaction is limited due to the poisoning of the active site. $mZrO_2$, $tZrO_2$, and MgO have positive adsorption energies implying an endothermic process. On the contrary, CeO_2 has highly exothermic adsorption energy of -1.63 eV. Also, the defects created on the MO surfaces have a small effect on the hydrogen adsorption energies (see Table 5.4), an expected behavior considering that both the d–MO exhibit Lewis base character. On the other hand, the Lewis acidity of doped ZrO_2 and MgO surfaces renders hydrogen adsorption more exothermic than the hydrogen adsorption on pristine ZrO_2 and MgO surfaces, with changes in the adsorption energies up to 1 eV in comparison the adsorption energies on pristine MOs. The hydrogen adsorption on CeO_2 and single-atom-doped CeO_2 does not change as much as in the other systems, mainly because of the weak Lewis acid character of CeO_2 [60]. The correlation of these changes with the C–H bond activation will be discussed in the following sections.

5.5. C–H Bond Activation of Propane on MOs and M_1-MOs

The successive removal of two hydrogen atoms from the methylene and methyl groups, followed by the desorption of propylene and H_2 from the catalysts surface, is generally accepted as the main reaction pathway of the non-oxidative DHP. The methylene group happens to be the one that initiates the activation of propane to produce 2-propyl, as it is known that the methylene group is more readily activated than the methyl group [194]. Therefore, this study focused only on propane's first C-H bond activation because it is considered the rate determinant step of the dehydrogenation reaction [39].

Figure 5.3, besides the geometries of the initial state, also illustrates the transition and final state geometries for the first C – H bond activation of propane on $mZrO_2$ and CeO_2.

As discussed elsewhere [39, 60, 69], there are two types of TS structures; on the one hand, a surface-stabilized TS resembles the FS co-adsorbed structures (e.g., ZrO$_2$), indicating a late TS (Figures 5.3b and c, respectively). The other structures are radical-like (e.g., CeO$_2$), where the interaction between the molecule and the surface is mainly due to dispersion forces, and the TS structures are very much similar to the physisorption of propane, as can be seen from the bond distances of the IS and TS structures on CeO$_2$ in Figures 5.3j and k, respectively.

Figure 5.4 shows the free energy diagram of the first C – H bond activation of propane on MOs and M$_1$ – MOs at 550 °C. As discussed in the previous section, for MOs, a simple correlation between the hydrogen binding and propane activation energy can be identified (see Table 5.4). Nondefective mZrO$_2$ and tZrO$_2$ have intermediate activation energies (see Figures 5.4a and b), with tZrO$_2$ having the lowest activation energy with ca. 2.2 eV. On both surfaces, the C – H bond cleavage occurs via dual Lewis acidic oxygen and Lewis basic Zr sites, as confirmed by the Bader charge analysis in Table 5.5, where the Zr atom donates electrons to the reacting acid (2-propyl), and the O atom takes electrons from the reacting base (H atom). On the other side, CeO$_2$, despite not having a Lewis acid-base (LAB) pair, has the lowest activation energy of the investigated pristine MOs (1.25 eV, Figure 5.4c); this is due to the high hydrogen adsorption energy that promotes a charge transfer from the substrate to the CeO$_2$ surface (see Table 5.5). Considering the inactivity of the Ce atom towards bond formation shown in Figure 5.3l, the charge donated by the 2-propyl to the Ce cation is almost negligible (see Table 5.5). Finally, it can be seen in Figure 5.4d that the activation energy on MgO is quite uphill with ca. 3 eV; it is well known that the reactivity and bond formation ability of Mg atoms are fairly low [207]. In Figure 5.5, the projected density of states (PDOS) for one Mg surface atom and its oxygen near-est neighbors confirmed a very weak interaction between the 3s magnesium and 2p oxygen states. Moreover, Lewis acidic and basic sites (O and Mg atoms, respectively) stabilize the C – H bond TS structure on the MgO surface, as the two species involved in the reaction exhibit opposite charges (2-propyl and H), as shown in Table 5.5.

The oxygen vacancy effect on the C – H bond activation of propane has been studied for ZrO$_2$ and CeO$_2$. For the evaluated MOs, the oxygen vacancies positively affect the reactivity of the surfaces, decreasing the activation energy until as e.g., seen for d-tZrO$_2$ (see Figure 5.4b). For both ZrO$_2$ phases, propane activation by two Zr cations located at an oxygen vacancy was studied as these have been suggested as the active sites [34, 35]. Structurally, the main effect is seen on the metal-hydrogen bond, which on the d-mZrO$_2$ is reduced substantially (Figure 5.3e). Comparison of the pristine and defective mZrO$_2$ PDOS (Figures 5.5a and b) indicates the highest occupied molecular orbital of Zr 4d orbital is up-shifted to the Fermi level and can therefore interact more strongly with the adsorbate's orbital, which could be responsible for the catalytic activity improvement. The same behavior is observed in the pristine and defective tZrO$_2$ surfaces. This kind of C – H bond cleavage follows a non-LAB interaction because the defective surface donates electrons behaving as a Lewis base; this behavior is seen clearly in the effective Bader charge transfer between the d-ZrO$_2$ surfaces and the hydrogen atoms shown in Table 5.5. On the contrary, the oxygen vacancy on CeO$_2$ facilitates a LAB interaction on the d-CeO$_2$ surface during the C – H breaking bond. The H (2-propyl) specie donates (accepts) electrons to (from) the
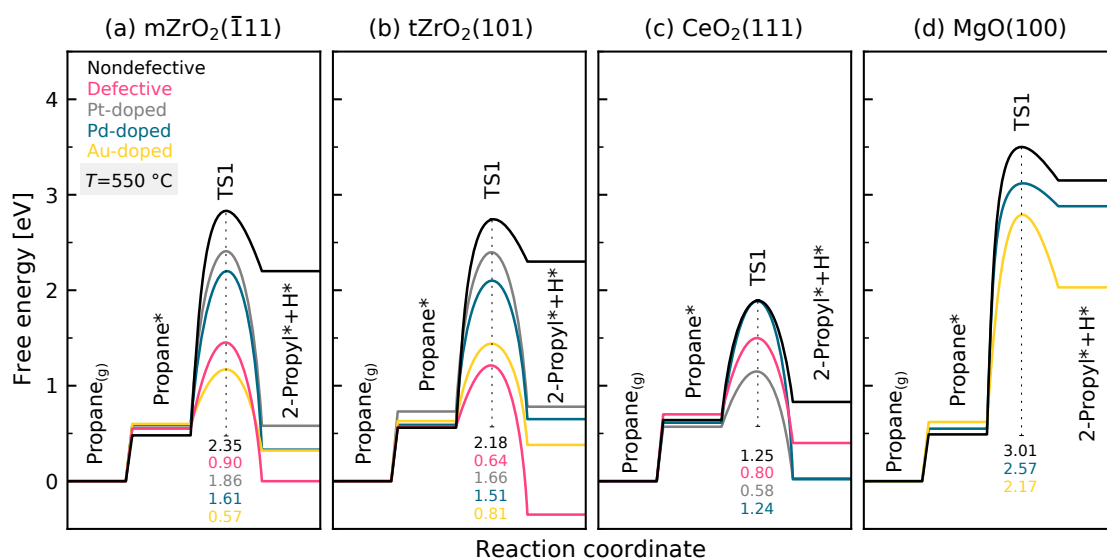
Figure 5.4. Free energy diagrams for the C–H bond activation of propane on pristine and defective MOs and M_1–MOs of (a) $mZrO_2$, (b) $tZrO_2$, (c) CeO_2, and (d) MgO at 550 °C.

Table 5.5. Effective Bader charges of the propane C–H bond TS structures on the MOs and M_1–MOs surfaces. M refers to the metal cation/dopant, O to the oxygen involved in the C–H bond activation, 2-propyl and H are the adsorbent species

		M	2-Propyl	O	H
$mZrO_2$	Pristine	2.53+	0.43-	1.22-	0.47+
	def	2.21+	0.18-	1.27-	0.23-
	Pt	1.27+	0.02-	0.97-	0.35+
	Pd	1.17+	0.02+	0.94-	0.34+
	Au	1.15+	0.06+	0.83-	0.25+
$tZrO_2$	Pristine	2.54+	0.42-	1.26-	0.41+
	def	2.35+	0.25-	1.28-	0.35-
	Pt	1.27+	0.03-	1.04-	0.38+
	Pd	1.15+	0.04+	1.01-	0.34+
	Au	1.18+	0.09+	0.94-	0.30+
CeO_2	Pristine	2.38+	0.02+	1.07-	0.23+
	def	2.11+	0.01-	1.09-	0.25+
	Pt	1.44+	0.02+	0.85-	0.30+
	Pd	1.28+	0.05+	0.79-	0.23+
	Au	-	-	-	-
MgO	Pristine	1.67+	0.64-	1.52-	0.41+
	def	-	-	-	-
	Pt	-	-	-	-
	Pd	0.64+	0.12-	1.51-	0.21+
	Au	0.56+	0.09-	1.51-	0.22+

surface, as shown in Table 5.5. For d-CeO_2, the C–H bond cleavage occurs adjacent of the oxygen vacancy; therefore, an O–H bond formation is involved during the reaction, this distance does not differ too much from the non-defective activation of propane, being ~1.37 Å, as shown in Figures 5.3k and n, but the activation energy is reduced compared to the non-defective case. This positive effect of oxygen vacancies has been described
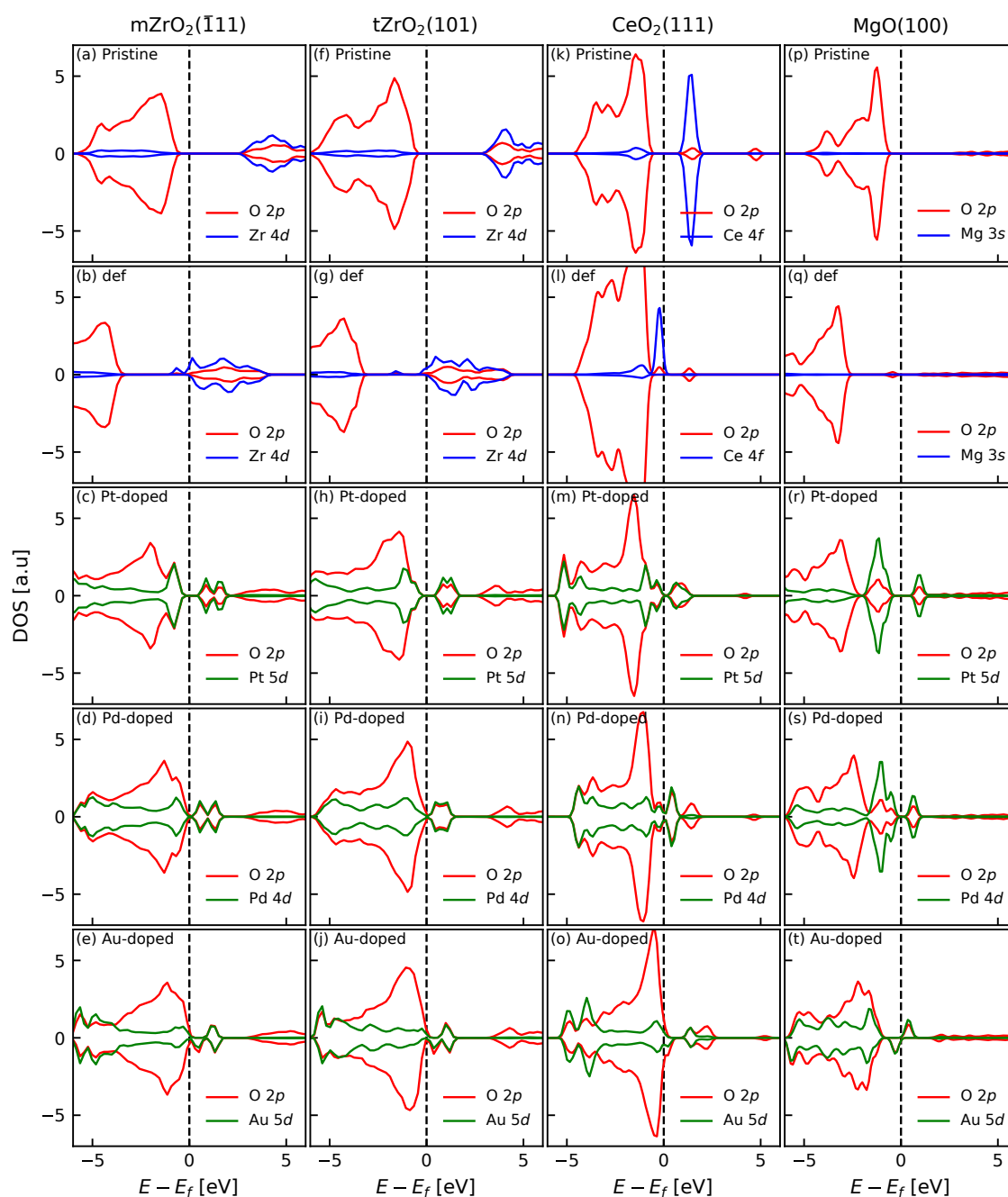
Figure 5.5. Projected DOS of the MO and $M_1 - MO$ surfaces. For MOs $d/f/s$-orbital of the metal and the p-orbital of oxygen nearest neighbors are projected. For the $M_1 - MOs$ the d-orbital of the dopant and the oxygen nearest neighbors are presented.

before on d-MO surfaces [34, 233], an exception being d-ZnO because the LAB interaction is suppressed and both the Lewis base and the Zn ion donate electrons to the Lewis acid [62].

In addition, SACs formed by the four MOs listed above in connection with Pt, Pd, and Au were also investigated. Figure 5.4 shows the free energy reaction pathways of the first C–H bond activation at 550 ℃ calculated for the doped systems. Previously, it has been shown that the catalytic activity of an oxide can be improved by substitutional doping [39, 204, 205, 234], and as discussed by Metiu et al. [60], in most cases, doped MOs can be turned into Lewis acid surfaces if the dopant has lower valence electrons than the substituted metal cation This reasoning has been supported by a density of states (DOS) analysis, that revealed that the lowest unoccupied molecular orbital (LUMO) is shifted to a state of lower energy, increasing the ability of the surface to accept electrons, hence making the $M_1 - MO$ systems a stronger acid. These changes are observed in all the doped system PDOS investigated herein (see Figure 5.5).

Interestingly, the Au_1-doped systems show a high activity towards C – H bond activation, although metallic gold surfaces are typically very inactive for this reaction. This can be attributed to the asymmetry of the PDOS (Figures 5.5e, j, o, and t), which is present in all $Au_1 - MO$ systems and is located close to the Fermi level, thus allowing the doped surfaces to interact strongly with the adsorbates. It should be noted, however, that $M_1 - MOs$ are not very stable (see Figure 5.2). While MgO surface is not a very active material, the dopants (Pd and Au) have a prominent effect in reducing the activation energy on $M_1 - MgO$ surfaces, although the activation energies are still over the 2 eV. On the other hand, with very low hydrogen adsorption energies (or even endothermic reactions. While MgO itself is not a very active material, doping of MgO with either Pd or Au reduces the activation barrier to about 2 eV. This renders M_1-MgO surfaces the least active materials among those studied herein.

Next, M_1-CeO_2 are considered. For $Pt_1 - CeO_2$ (5.3q), a radical-like type TS was found; the Pd doped CeO2 has the same kind of TS structure as Pt. As in the case of the pristine MOs, the doped systems have very low activation energies of 0.58 and 1.24 eV for Pt_1- and $Pd_1 - CeO_2$, respectively. Although, as discussed in the previous section and somewhere else [41, 64], these systems could potentially suffer from selectivity issues due to the high propylene and hydrogen adsorption energies. Even though the $M_1 - CeO_2$ systems have low activation energies, propane activation on doped CeO_2 systems is characterized by the absence of LAB interactions between the surfaces and the adsorbates. These charge transfer considerations have been examined before, finding that the absence of LAB interactions for this type of surface is because the single metal ions are too electron-deficient, which limits the ability of the adjacent O atoms to transfer electrons to the adsorbates on top of the M site [39].

Finally, in the case of metal doped ZrO_2 systems, radical-like TS structures and no LAB interaction are found (see Table 5.5). There is a good balance between stability and reactivity in the cases of Pt_1- and $Pd_1 - ZrO_2$ systems with average activation energies around 1.70 eV. The systems doped with Pt and Pd have surface-stabilized TS structures (Figure 5.3h), similar to those of the pristine MOs. Indeed, the $Pt_1 - ZrO_2$ surfaces are the only $M_1 - ZrO_2$ systems presenting a pure LAB pair interaction (see Table 5.5), though these systems have a higher activation energy than the Pd_1- and $Au_1 - ZrO_2$ catalysts. Overall, all the studied dopants positively affect the TS energy, and the Au-systems exhibit

the most prominent effect with the lowest TS energies. Considering all the properties described, doped ZrO_2 systems seem to be the most promising SAC candidates for propane activation among all the systems studied herein. The Gibbs free energy profiles shown here provide a first overview of the differences between the various catalysts investigated herein. In the next section, it is shown that there are also universal LSRs for these classes of surfaces.

5.6. Linear Scaling Relationships

Scaling relationships are often used in the search for new catalytic materials. These are established after descriptors have been identified that describe a chemical reaction in approximate ways. While these might be dependent on the computational method used, universal scaling relationships that are independent of the employed density functional have also been reported. We therefore included previously pub-lished data for alkane C-H bond activation on diverse MO catalysts in our analysis. The collected data cover more than ten MOs, a good number of dopants, and more than 100 barriers (for pure MOs and SACs) calculated with seven different functionals. For more information about the collected data, such as MOs, dopants, slab surfaces, and the number of points per functional, please see the Appendix A

Figure 5.6a shows an initial analysis entirely based on the collected BEEF-vdW data. The TS and FS energies of the C – H bond activation for methane, ethane, and propane on several MO surfaces correlate linearly quite well. The data has been taken from our calculations (4 catalysts) and other theoretical studies using the BEEF-vdW functional. A complete list of the MOs used is presented in Tables A.1 and A.2. As can be noticed, all the MOs share the same LSR with a small mean absolute error (MAE) of 0.14 eV. The fact that radical-like and coadsorbed-like TS structures and surfaces with different LAB properties share the same LSR broadens the scope of previously reported ASRs for individual or group like MOs, showing that the FS energy is among the best and more general descriptors within the C – H bond activation group correlations for catalyst materials. The same analysis was performed for the collected TS and FS energies calculated with PBE-D3, PBE, and (with some limitations) PW91, as shown in Figures 5.6b-d. These LSRs follow the same trend and are similar to those obtained using BEEF-vdW data.

Following the analysis and the implications above, a single universal LSR for the C – H bond activation covering all the functionals and MO surfaces found in the literature is developed, as shown in Figure 5.7a. A quick comparison with the LSRs presented in Figure 5.6 shows only slight changes, but in principle, this LSR (in just one correlation) assembles all the characteristics of the individual correlation from Figure 5.6, which now works for all the functionals studied here (BEEF-vdW, PBE-D3, PBE, PW91, optB88-vdW, vdW-DF2, and PBEsol). The defective C – H bond activation data were also expanded, giving more confidence in applying this new correlation to these systems. To the best of our knowledge this is the first time that, the C – H bond activation on defective surfaces is included in a general LSR of this kind. The existence of a universal ASR for the prediction
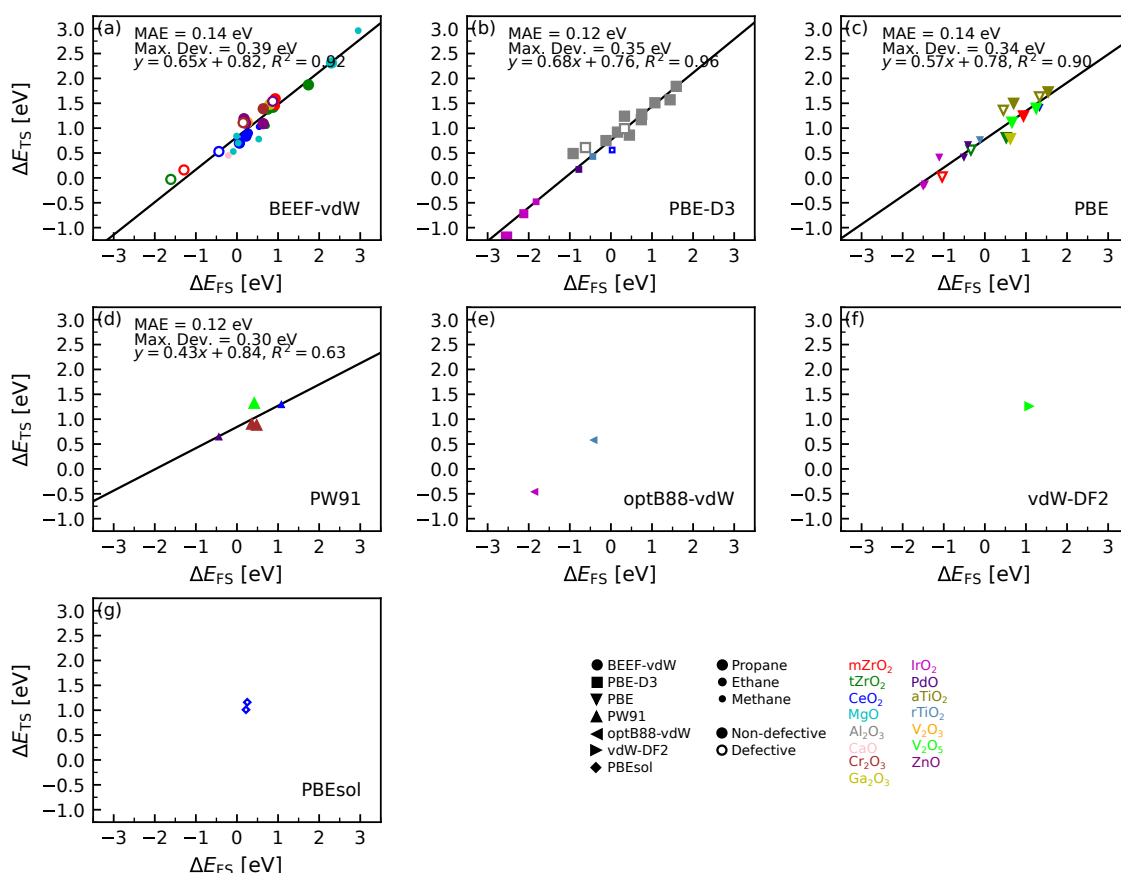
Figure 5.6. Transition-state LSRs for the C – H bond activation of alkanes on non-defective and defective MO surfaces for each functional.

of (de)hydrogenation TS energies on TM or MO surfaces has been postulated before [150, 176, 212]. Accordingly, the inclusion of several functionals and MO surfaces shows the universality of this LSR for predicting the TS energy of the C – H activation of alkanes, with MAE and maximum deviation values within the typical accuracy of DFT calculations, 0.19 and 0.34 eV, respectively. Further, it might even be possible to extend the prediction of the TS energies to longer alkanes such as *n*-butane, based on the data reported by Li et al. [235] This was already shown in chapter 4 for the C – H bond activation of alkanes on TM surfaces. For ZrO$_2$ and CeO$_2$ surfaces (among others), data for the activation of the first three alkanes are included, despite the TS energies not following the same trend as on TM surfaces (decreasing as the carbon-chain length increases), the data still follows the universal LSR for C – H bond activation on MOs. Finally, it is worthwhile to highlight the high density of data points for the TS energy around the $1.0 - 1.5$ eV interval, which suggests that only the FS energy as a descriptor is not enough to screen the selectivity of the catalysts and emphasizes the necessity for other descriptors to account for the selectivity of the catalyst, like the ones suggested in previous studies [134, 168, 191, 208].
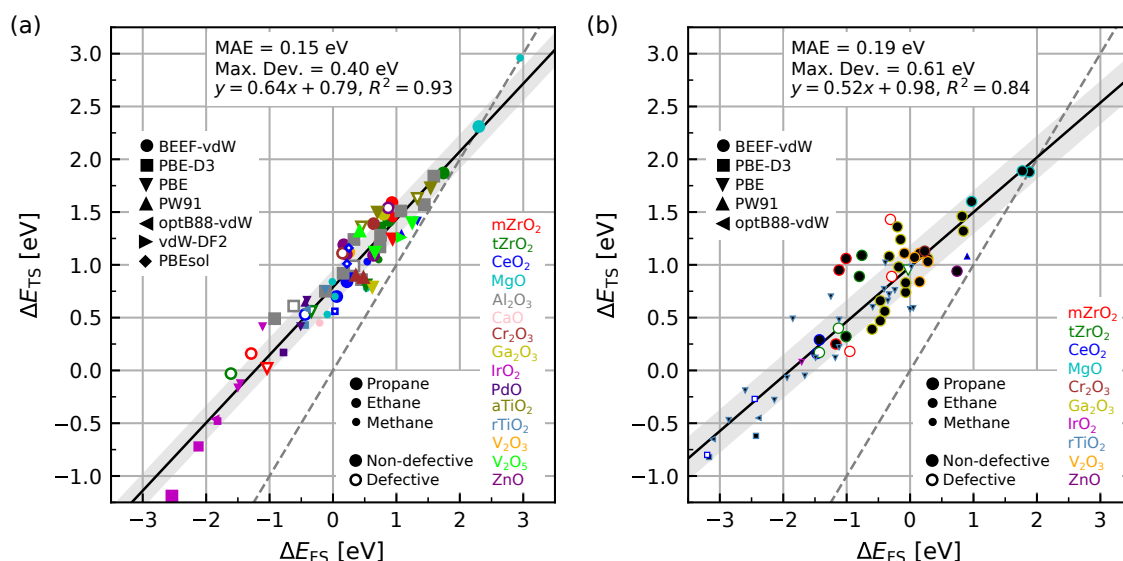
Figure 5.7. Transition-state LSRs for the C–H bond activation of alkanes on non-defective and defective (a) MOs and (b) SACs surfaces. The dashed line represents the $y = x$ function.

Consequently, a universal LSR between the TS and FS energies for alkane (methane, ethane, and propane) C–H bond activation on the single-atom-doped systems ($M_1 - MO$) is also developed and shown in Figure 5.7b. A complete list of the M1-MO catalysts is presented in Tables A.1 and A.2. The systems covered by this LSR include dopants with lower and higher valence electrons than the replaced cations (i.e., $Pt_1 - CeO_2$ and $Ni_1 - V_2O_3$), reducible and non-reducible oxides (i.e., $M_1 - TiO_2$ and $M_1 - ZrO_2$). Data for the C–H bond activation on $d-M_1 - ZrO_2$ was also calculated and included in the LSR (see Table A.1). Despite a maximum deviation of 0.60 eV, an MAE of 0.19 eV is relatively small considering the high degree of surface heterogeneity (quite high for the doped oxide surfaces) with several functionals, dopants, and MOs included in this correlation. Individual correlations for BEEF-vdW and PBE functionals are shown in Figures 5.8a and c, and follow the same trend as shown in Figure 5.7b. For the other functionals included in the universal LSR in Figure 5.7b, the lack of data does not produce reliable individual correlations. Nevertheless, that data falls into the general LSR for SACs.

Further, the differences of the TS and FS energies have been plotted for the C–H bond activation of the SACs and their MO surfaces(see Figure 5.9) showing how the dopants affect the TS and FS energies. For instance, Pt (one of the most common dopants) always has a positive effect on reducing the TS energies. Also, it is possible to see how the TS energy increases on TiO_2 dopants with higher valance electrons. However, Au's effect as dopant decreases the TS energies substantially for the studied systems, despite being the least stable dopant. Pd has a similar effect as Pt, but it is typically more stable than Pt-systems.

Finally, Figure 5.10 demonstrates the excellent agreement be-tween the predictions of our models (see Figure 5.7) and the calculated DFT values for the TS energies of the C–H

Figure 5.8. Transition-state LSRs for the C–H bond activation of alkanes on non-defective and defective M_1–MO surfaces for each functional.

Figure 5.9. Difference between the TS energies of the alkane C–H bond activation on SACs and MOs surfaces as a function of their FS energies.

bond activation of alkanes across a wide variety of reactants, catalyst, and functionals. Considering the number of variables involved in these simple correlations, the mean absolute error (MAE) and maximum deviation are small. Therefore, they could be considered predictive models for the C-H bond activation on MOs and M_1–MOs, serving as a tool for preliminary screening of catalysts for C–H bond activation of alkanes.
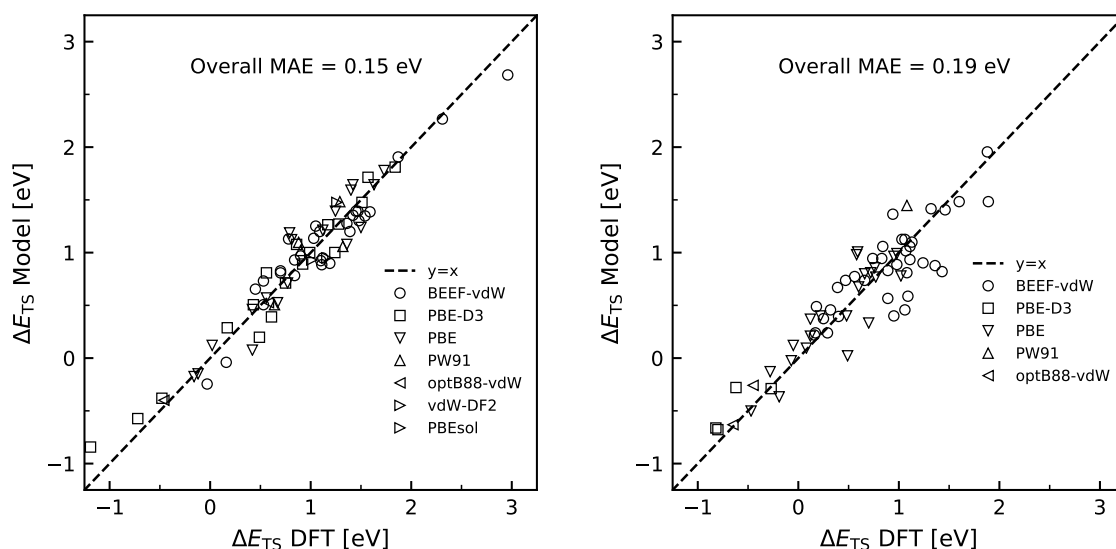
Figure 5.10. Parity diagram for the accuracy of the models. Calculated DFT TS energies compared with the predictions from the models presented in Figure 5.7 for the C – H activation of alkanes on MOs and SACs surfaces.

5.7. Chapter Conclusions

The C – H bond activation of light alkanes (methane, ethane, and propane) on MOs and single-atom-doped-MOs surfaces was analyzed using DFT calculations. In the first part of this investigation, the C – H bond activation of propane on pristine and doped (Pt, Pd, and Au) monoclinic and tetragonal ZrO_2, CeO_2, and MgO surfaces were studied. The effect of oxygen vacancies was included as well. It was found that the C – H bond activation on MOs and $M_1 – MOs$ can be explained based on the Lewis acid-base properties of the surfaces, as also shown in previous studies. Among the analyzed pristine and defective surfaces, ZrO_2 presented the best combination of properties for propane activation. On the other hand, the analyzed dopants have lower valance electrons than the substituted metal cations; therefore, the surfaces became Lewis acid surfaces behaving differently than the pristine surfaces, the atomic hydrogen and propylene adsorptions are stronger, and independent, if during the reactions there is a Lewis acid-base interaction, the TS energies are reduced in all cases. The systems with radical-like TS structures and no LAB interaction (e.g., $Au_1 – CeO_2$) have the lowest transition state energies, but the stability of the single atom is usually low. Considering all the properties analyzed, the doped ZrO_2 systems seem to be the most promising SACs among the studied systems.

In the second part, by collecting previously published data, structure-activity relationships represented by linear correlations between the TS and FS energies were developed for the C – H bond activation of alkanes on MOs and $M_1 – MOs$ systems, covering some of the most common functionals used in periodic DFT calculations. These universal LSRs for the C – H activation of light alkanes cover a broad structural diversity of MOs and $M_1 – MOs$

catalyst surfaces, including the effect of superficial oxygen vacancies, several dopants, and more than one phase of the same MO, and different active sites. Besides, it is confirmed that the FS energy is one of the most general descriptors to estimate TS energies on MOs and M_1–MOs, which previously was demonstrated for the C–H bond activation on TMs surfaces. Therefore, the LSRs developed for the C–H bond activation of alkanes on MOs and M_1–MOs are universal with no functional restrictions.

These LSRs are expected to pave the way toward the computational development of new and better catalyst materials guiding future experiments as a first-hand tool in heterogeneous catalysis. Moreover, in computational catalysis, many challenges are ahead, and it is still necessary to incorporate the dynamic nature of heterogeneous catalysis under realistic experimental conditions either in the LSR or the microkinetic modeling in order to provide a more effective screening of materials with a potential industrial application such as dry reforming, steam reforming, partial oxidation, and (oxidative) dehydrogenation. Even though the LSRs ease the computational cost of complex reaction networks, the DFT calculations needed to obtain them are time-consuming and cost-ineffective. Hence, the computational-assisted discovery of materials should go through the application of universal LSRs and machine learning synergistic approaches. While this study covers the activity of catalysts towards C-H bond activation, selectivity descriptors as well as stability measures are also needed in future studies.

6. Hydrogenation of Aldehydes on Palladium Surfaces

6.1. Introduction

One of the fundamental steps in heterogeneous catalysis is the adsorption of the substrate onto the active site. In the case of molecules containing a carbonylic group, such as aldehydes, the adsorption can happen in two modes: η_1–(O) mode and η_2–(C, O) mode [236]. The former implies the interaction of the lone pair of oxygen with the catalyst surface, while the latter involves interaction with the double bond of the carbonyl group. These adsorption modes are affected not only by steric hindrance but also by electronic effects. In the case of furfural and 5-hydroxymethylfurfural, for example, a strong interaction between the catalyst and the π-bonds of the aromatic furan ring directs the adsorption of the substrate to a flat η_2–(C, O) position [237]. This, in turn, can strongly affect the selectivity of the reaction, increasing the rates of side reactions such as decarbonylation and furan ring hydrogenation, as demonstrated by Duarte et al. [238].

It is clear that despite the paramount importance of hydrogenation and hydrodeoxygenation reactions of aldehydes, fundamental studies on parameters that rule the reactivity of the carbonyl group are limited. Besides, they often fail to consider the catalytic system as a single ensemble constituted by catalyst (metal and support) and substrate. Therefore, this work presents a systematic analysis of the main roles played by the nature of carbonyl-bearing substrates in the hydrogenation reaction on Pd-based catalysts, intending to shed light on their entangled mechanisms. By selecting aromatic (benzaldehyde) and aliphatic (octanal/propanal) aldehydes differing not only in structure but also in electron density of the carbonyl group, it is possible to study (i) the substrate adsorption, which in turn is an indication of the proximity of the substrate to the active site and its retention by the catalyst; (ii) the electronic structure of the reducible group (C = O), which interacts with the electronic properties of the catalytic site. These two effects were studied using a combination of analytical tools (such as substrate adsorption and temperature-programmed desorption-TPD analysis) and DFT calculations. This study can unravel

the main factors governing the reaction mechanism, providing a guideline for the future synthesis of materials with high activity and selectivity in the framework of aldehydes hydrogenation.

6.2. Computational Details

Density functional theory (DFT) calculations were carried out using the Vienna Ab Initio Simulation Package (VASP) [139, 140] and the Atomic Simulation Environment (ASE) [117] employing the generalised gradient approximation (GGA) with Bayesian error estimation functional with van der Waals corrections (BEEF-vdW) [104, 141] and the projector-augmented wave (PAW) potentials [115, 116]. The computational setup for the Pd(111) surface is similar to the one used in chapter 3. Briefly, a four-layer slab of palladium with varying supercell sizes and k-point meshes were used (see Table 6.1). During the relaxations, the two bottom layers of the slabs were kept fixed at the bulk positions. A kinetic energy cutoff of 450 eV was used for all calculations. In order to avoid interaction between periodic images, the Pd slabs are separated by approximately 20 Å of vacuum along the z-direction. Additional, single-point energy calculations using the PBE functional, including Grimme's dispersion corrections (PBE-D3, zero damping), were performed [103, 142]. The reference systems used for the calculations of the adsorption, activation, initial, transition, final state, and D3 contribution energies were presented in section 2.10, including the methods used for the transition state searching and how the contributions to the free energy were calculated.

6.3. Benchmarking of Functionals

In order to understand and quantify the differences in adsorption strengths between the two substrates (benzaldehyde and octanal), density functional theory (DFT) calculations were carried out. A benchmarking of common density functionals for the calculations of benzaldehyde and octanal adsorptions was initially performed due to the difficult description of the interaction of benzaldehyde and octanal with transition metal surfaces. The DFT calculations are quantified using experimental data for (1) the adsorption of linear alkanes on Pd(111) surfaces [239] and (2) the adsorption of benzene on Pd(111) [240], as shown in Figure 6.1.

Table 6.1. Cell sizes and corresponding k-point sampling of the Pd(111) surfaces.

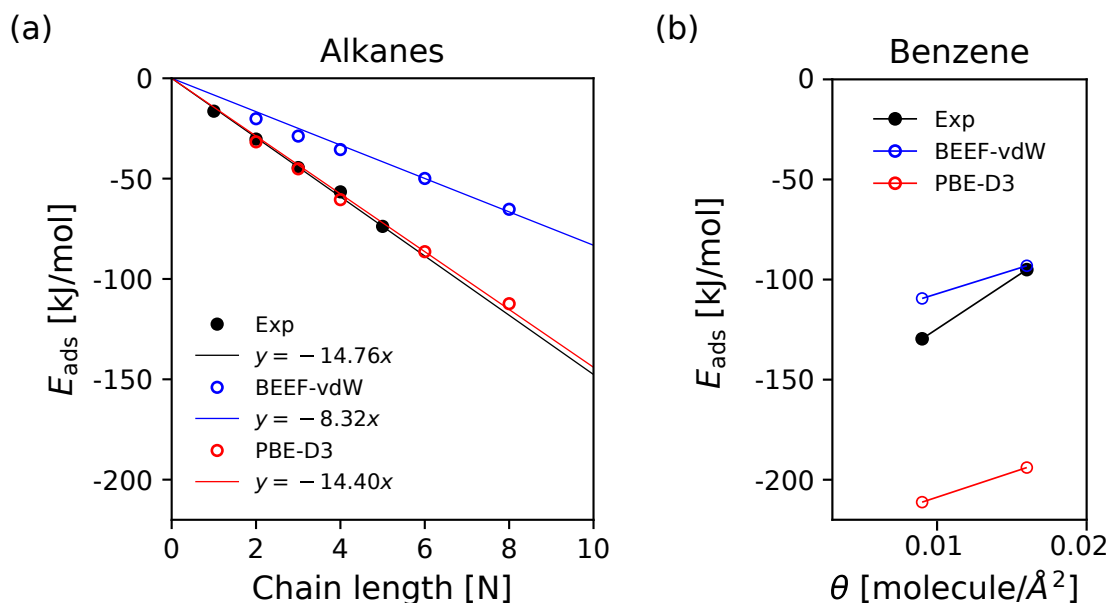| Surface	Area [Å^2]	k-points
2×2	27.4	6×6×1
3×2	41.1	4×6×1
3×3	61.7	4×4×1
3×6	123.4	4×2×1
3×7	144.0	4×1×1
4×4	109.7	3×3×1
4×5	137.1	3×2×1

Figure 6.1. Adsorption energies of (a) alkanes as a function of the carbon chain length, and (b) benzene as a function of surface coverage. Experimental values are taken from Antony et al. [239] and Tysoe et al. [240]

Figure 6.1a shows a comparison between the calculated adsorption energies of C_1–C_8 alkanes on the Pd(111) surface calculated using the BEEF-vdW and PBE-D3 functionals and the experimental values as a function of the number of carbon atoms of the corresponding alkanes. The primary interaction of these alkanes with the Pd(111) surface comes from dispersion forces. Besides, it can be seen that the PBE-D3 functional is much better in reproducing the alkane adsorption energies than the BEEF-vdW functional. In fact, PBE-D3 has only very small errors compared to the experiments. Therefore, the PBE-D3 functional is the best option for the octanal adsorption calculations and it is used for this purpose in the rest of the chapter. Figure 6.1b shows a comparison of the two functionals and the experimental adsorption energies of benzene on Pd(111) as a function of coverage. In this case, the situation is reversed: the BEEF-vdW functional performs much better than PBE-D3, with the latter having an error of more than 70 kJ/mol. Hence, the BEEF-vdW functional is employed for calculations of benzaldehyde adsorption.

6.4. Aldehydes Adsorption on Palladium Surfaces

The adsorption isotherms using benzaldehyde and *n*-octanal as probe substrates were determined. Interestingly, increasing the substrate partial pressure, both benzaldehyde and octanal interact with the catalyst surface (Figure 6.2a). A larger amount of benzaldehyde than of octanal was adsorbed at any time, with a maximum quantity adsorbed of 66 cm^3/g (compared with 62 cm^3/g with octanal) before condensation phenomena occurred at ca. 2.0 mmHg. Substrate surface coverage values were estimated based on the adsorption at
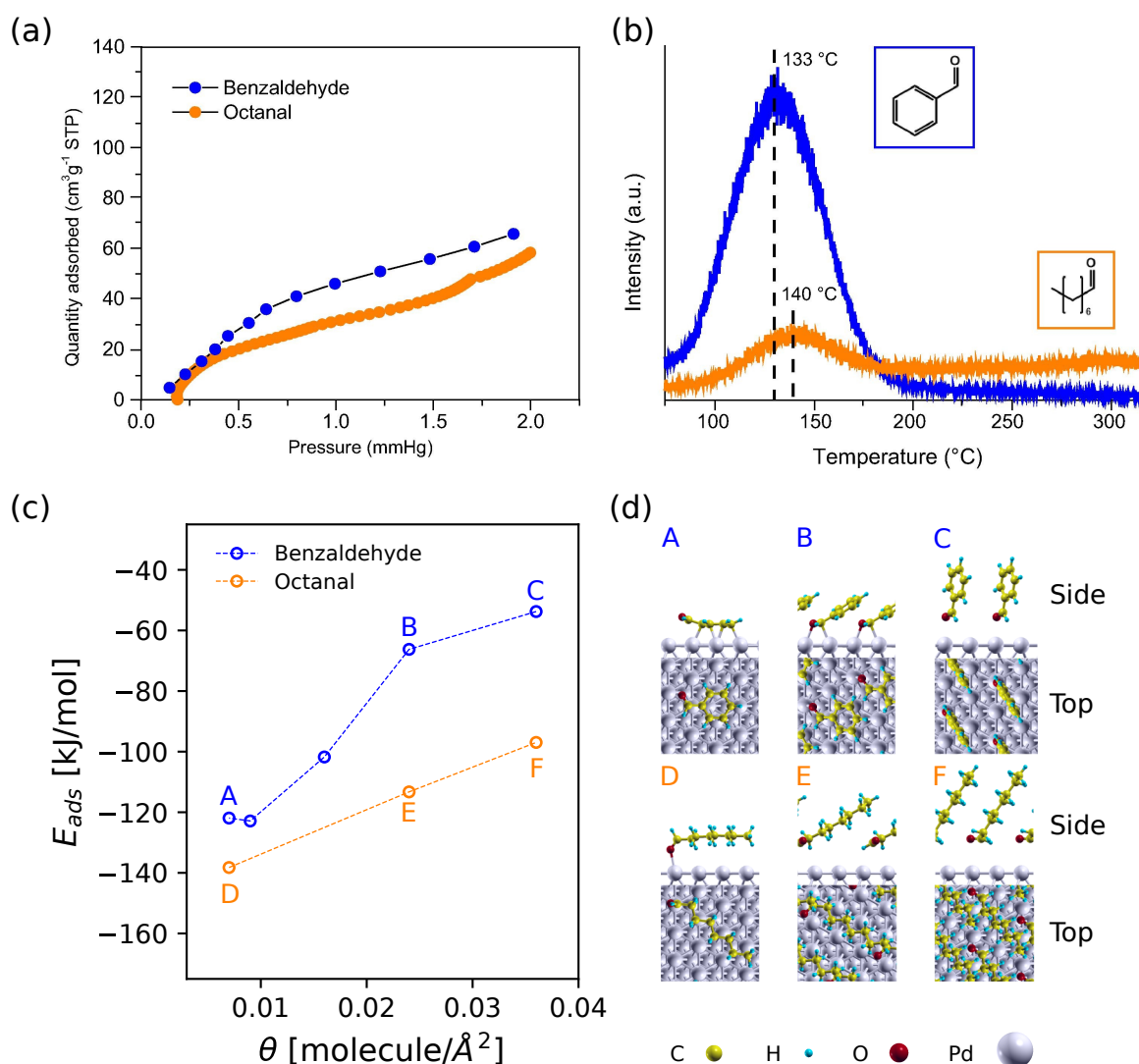
Figure 6.2. (a) Benzaldehyde and octanal adsorption isotherms of Pd/AC at 40 °C. (b) TPD analysis of benzaldehyde and octanal on the Pd/AC catalyst, the reactor was heated up till 350 °C at 5°C/min. All isotherms and TDP analysis were performed by Stefano Cattaneo at Milan University. (c) Benzaldehyde and octanal adsorption energies as a function of the surface coverage. (d) Configurations of the benzaldehyde (A, B, and C) and octanal (D, E, and F) adsorption. Coverages are given as molecules per Å^2 of the Pd surface. Adapted from Ref. [71]. Copyright 2021, Elsevier Inc.

1.9 mmHg: the surface coverage for octanal was 0.0154 molecules/Å^2. At the same time for benzaldehyde was ca. 21% higher, with an estimated value of 0.0186 molecules/Å^2. In addition, the adsorption isotherms of the two substrates followed a different trend in the whole pressure range studied, which suggests a different adsorption mechanism for the two molecules. In particular, the isotherm of octanal changes slope more than once in the range of pressures studied. This means that the mechanism of adsorption of octanal is more complex than that of benzaldehyde and/or might involve different adsorption sites, as highlighted in the DFT study (see below).

Moreover, adsorption isotherms showed that octanal (as well as benzaldehyde) adsorbs onto the catalyst surface. In particular, the reactants are likely to adsorb mainly within the carbon micropores; in fact, micropores have a strong interaction with the substrates due to weak van der Waal interactions. Unfortunately, this technique does not provide information regarding the strength of interaction between the different substrates and the catalyst surface. For this reason, TPD measurements using both benzaldehyde and octanal as probe molecules for the Pd/AC catalyst were carried out by our experimental collaborators (Figure 6.2b). Although the peak areas cannot be directly compared, as it was impossible to calibrate the mass spectrometer due to the very low vapor pressure of both molecules, the chemisorption of octanal was proven by the presence of substrate desorbing at a temperature of 140 °C (orange line). Benzaldehyde desorbed at a similar temperature (133 °C), showing, in this case, a much stronger signal (blue line). These low desorption temperatures point in the direction of substrate physisorption onto the catalyst surface.

Using DFT, the adsorption energies of octanal (with PBE-D3) and benzaldehyde (with BEEF-vdW) as a function of surface coverage were calculated, as shown in Figure 6.2c. In both cases, the adsorption energy depends on the coverage. Benzaldehyde adsorbs with the aromatic ring parallel to the Pd(111) surface in an almost flat geometry with an adsorption energy of ca. −120 kJ/mol at low coverages, $\theta = 0.007$ and 0.009 molecules/Å^2 (which correspond to 4×5 and 4×4 unit cells, see 6.2d, structure A). Higher coverages were evaluated with a single molecule in 3×2 and 2×2 unit cells of Pd(111) surface, $\theta = 0.024$ and 0.036 molecules/Å^2 respectively. At $\theta = 0.024$, the benzaldehyde molecule adsorb through a η_2–(O) mode (see 6.2d, structure B) with an energy of −66 kJ/mol. A decrease of more than half of the adsorption energy is found at high coverage of benzaldehyde (ca. −54 kJ/mol) (see 6.2d, structure C). At low coverage (one molecule in a 3×7 unit cell of Pd(111), corresponding to a coverage of $\theta = 0.007$ molecules per Å^2), octanal is chemisorbed on the palladium surface through an η_1–(O) mode, and the aliphatic chain lies over the surface with an adsorption energy of −138 kJ/mol over,(see Figure 6.2d, structure D). As the coverage increases (one molecule per 3×2 and 2×2 unit cells), the octanal molecules start to tilt over, reducing the adsorption energy to −97 kJ/mol (see Figure 6.2d, structure F). The adsorption energies of octanal are always higher than those for benzaldehyde at any coverage investigated herein, confirming the results obtained by TPD.

Therefore, from the theoretical and experimental results, it is concluded that both substrates change adsorption mechanisms depending on the surface coverage. Furthermore, when normalizing the adsorption energies to the number of molecules per surface area of Pd (molecules/Å^2), it is found that octanal binds more strongly to the Pd surface compared to benzaldehyde over the range of coverages investigated herein. Finally, the results of DFT calculations fit perfectly with TPD and adsorption isotherm results. However, the differences in adsorption energy revealed between the two substrates are not enough to justify the complete inactivity of octanal hydrogenation on the Pd/AC catalyst shown by Cattaneo et al. [71]. Octanal, in fact, is entirely inactive at any range of concentration, while benzaldehyde can be easily converted. Therefore, to fully investigate the systems and highlight the possible role of carbonyl electron density, a set of experiments using slightly

Table 6.2. Adsorption energies of the species involved in the hydrogenation of propanal(octanal) and benzaldehyde. Numbers in parenthesis represent the D3 contribution from PBE-D3 calculation

ΔE_{ads} (kJ/mol)	BEEF-vdW	PBE-D3	ΔE_{ads} (kJ/mol)	BEEF-vdW	PBE-D3	ΔE_{ads} (kJ/mol)	BEEF-vdW	PBE-D3
Propane	-29	-45(-41)	Octane	-64	-113(-98)	Benzaldehyde	-124	-235(-106)
Propanal	-41	-69(-43)	Octanal	-82	-139(-103)	Benzyl alcohol	-121	-
Propanol	-49	-82(-52)	Octanol	-	-	Hydrogen	-34	-64(-3)

different substrates which differ from each other in electron density of the carbonyl group were carried out. See Cattaneo et al. [71] for more information.

6.5. Hydrogenation of Aldehydes on Pd Surfaces

The successive hydrogenation of aldehydes on the Pd(111) surface is studied using DFT calculations. Considering computational efficiency and economy, propanal is used instead of octanal. The results found through propanal hydrogenation can be easily extrapolated to octanal because these two aldehydes have the same functional group, The binding strength energy can be asses by the dispersion contributions of the carbon-chain length, as demonstrated in chapter 4. As shown in Table 6.2, the dispersion contribution difference between the adsorption of propane/octane and propanal/octanal is *ca.* 60 kJ/mol showing that the difference in energy is mainly due to the alkyl chain. A similar approach has been used before for propanoic acid instead of octanoic acid [86].

Figure 6.3a presents the free energy profiles for the benzaldehyde hydrogenation following the two possible competing reaction pathways at 50 °C, the first one attacking the O atom of the carbonyl group followed by the attack to the C atom. The second pathway is the other way around, and these two pathways are denoted as O→C and C→O, respectively. The first pathway, drawn with a solid blue line in Figure 6.3a, proceeds via hydroxyl formation (O–H bond) with an energy barrier of 73 kJ/mol (see Figure 6.3d). A second step, with an activation energy of 85 kJ/mol, where the carbon atom is attacked, leading to the formation of the corresponding alcohol (Figure 6.3e and f, respectively). In dashed lines is drawn the opposite process, that is, the formation of the C–H bond first and then the further formation of the O–H bond with activation energies of 105 and 35 kJ/mol, respectively.

Similar to the hydrogenation of benzaldehyde, propanal can be hydrogenated through the O→C and C→O reaction pathways. The activation energies of the former pathway are 63 and 99 kJ/mol for the first and second hydrogenation steps (see solid orange line in Figure 6.3b), and their transition state structures are presented in Figure 6.3h and i. The later pathway, dashed line in Figure 6.3b, has a high hydrogenation barrier for the C–H bond formation (67 kJ/mol) and a much lower for the O–H formation barrier (81 kJ/mol). Similar behavior has been shown in previous studies for the (de)hydrogenation of (propanol) 2-ethylhexenal on Pd, where the difference in the activation energies in the reaction pathways is small. [87, 89]
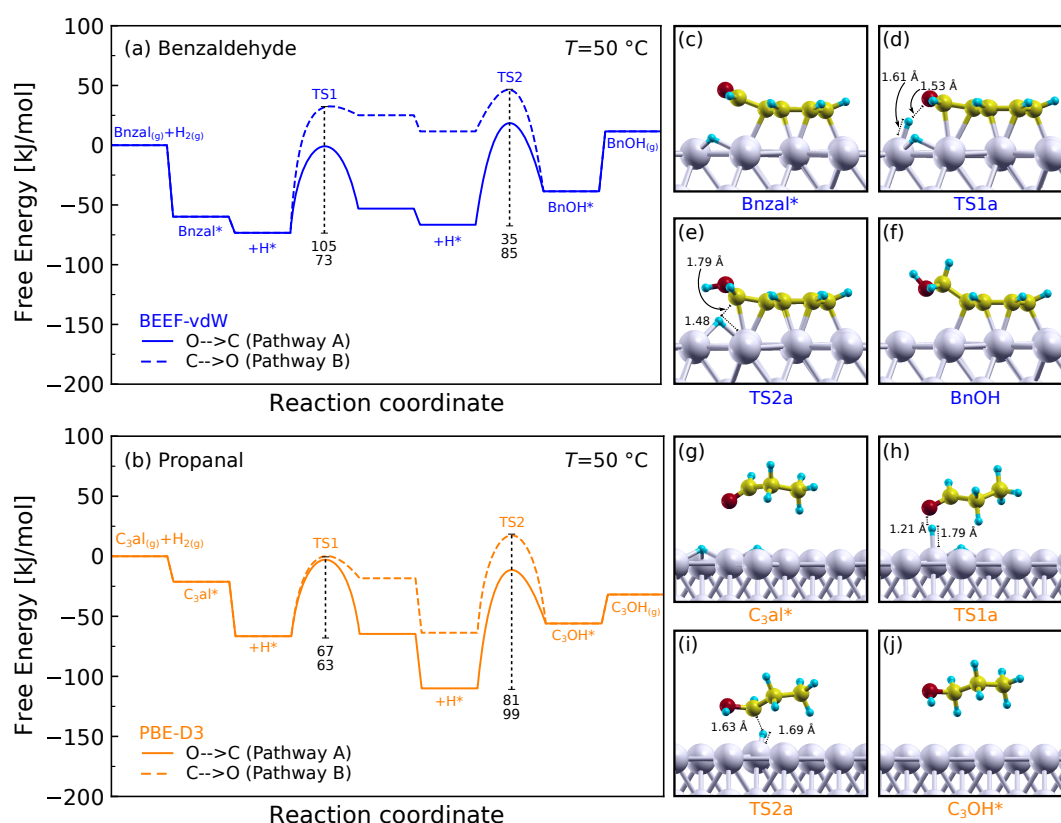
Figure 6.3. (a) Free energy profiles of the (a) benzaldehyde and (b) propanal hydrogenation on Pd(111) surface at 50 °C. The solid lines correspond to the reaction pathway where the O–H bond is formed first and then the C–H bond (O→C), the dashed lines correspond to the reaction pathway where the C–H bond is formed first and then the O–H bond (C→O). (c–f) Elementary steps of the O→C reaction pathway for benzaldehyde hydrogenation. (g–j) Elementary steps of the O→C reaction pathway for propanal hydrogenation.

Overall, benzaldehyde presents the lower activation energy barriers for the second hydrogenation steps, only 35 kJ/mol for the O–H bond formation. For propanal, there is no a real difference if the hydrogenation goes first through the carbon or oxygen atom. However, his second steps always have a higher barrier, and it is expected to be the rate determinant step, independently of the reaction pathway involved in the reaction. In order to determine the catalytic activity of Pd surfaces for the aldehydes hydrogenation, it is necessary to consider elaborate microkinetic models, including side reactions and catalyst deactivation. Further, it is necessary to investigate the solvent effect during the reaction; this could be asses using implicit solvation models, which capture the binding energy trends in complex systems.

6.6. Chapter Conclusions

This work elucidated the factors affecting the hydrogenation of various aldehydes on a Pd-based catalyst. Using benzaldehyde and *n*-octanal, the importance of the side chain

in determining the reactivity of the carbonyl group was demonstrated. Although the adsorption mode and strength are affected by the substrate structure, these aspects have proven not to be the decisive factors in the conversion of the carbonyl group. This was demonstrated by a combination of adsorption studies (substrate adsorption, as well as temperature-programmed desorption) and DFT calculations.

For the study of benzaldehyde and propanal/octanal adsorption using DFT, it is necessary to use two different functionals to describe the electronic properties of the substrates. While PBE-D3 functional performs well for the adsorptions of alkanes on Pd(111), BEEF-vdW functional severely underestimates their adsorption energies. On the contrary, BEEF-vdW functional performs rather well for benzene adsorption on Pd(111), while PBE-D3 is not. This behavior is expected to be transferable to benzaldehyde and propanal/octanal calculations.

Additionally, based on the hydrogenation calculations from the two possible pathways studied, the propanal hydrogenation presents similar activation energies through both reaction pathways and does not differ too much from the results obtained for benzaldehyde, despite of benzaldehyde has the lowest activation energy calculated. Nevertheless, the differences in the activation energies between the two substrates are not enough to explain the inactivity of propanal/octanal found experimentally. Therefore, considering microkinetic models of more elaborate reaction mechanisms becomes a further fundamental step, including the effect of the solvents. Finally, this study can provide valuable guidelines for the future investigation of materials with high activity and selectivity in the framework of hydrogenation of aldehydes.

7.   Final Conclusions and Outlook

This thesis dealt with the investigation of the C–H bond activation of light alkanes (methane, ethane, propane, *n*-butane) on transition metals (TMs), metal oxides (MOs), and single-atom-doped-metal oxides (M_1-MOs) surfaces, as well as the hydrogenation of aldehydes on palladium surfaces using density functional theory (DFT) calculations. The first part of this thesis covered the reaction mechanisms of propane's (oxidative) dehydrogenation to propylene over palladium surfaces, founding that the energy barriers of the oxidative dehydrogenation steps are always higher than those of the non-oxidative route. This strongly indicates that oxygen does not considerably change the kinetics of the reaction on Pd surfaces. Furthermore, it was shown that the transition state energies (ΔE_{TS}) scale with the final state energies (ΔE_{FS}) (on Pd(111) and Pd(211) surfaces), both for the oxidative and non-oxidative dehydrogenation of propane.

In the second part, the previous analysis is extended to the first (oxidative) dehydrogenation step of light alkanes (ethane, propane, and *n*-butane) on TM closed-packed and stepped surfaces, including an evaluation of the impact of oxygen and hydroxyl adsorption on the TM surfaces on promoting (e.g., for Au and Ag) and poisoning (e.g., for Co, Ni, and Rh) the reactions. In addition, a total of six linear scaling relationships (LSRs) are established (for the non-oxidative, the O-, and OH-assisted C-H bond activation of alkanes on TM closed-packed and stepped surfaces), showing that the ΔE_{TS} of the C–H bond activation of the studied alkanes scale linearly with the corresponding ΔE_{FS}. Here, the variations in ΔE_{TS} between alkanes were primarily attributed to differences in dispersion contributions determined by the carbon-chain length. Finally, it is shown that simple models based on the LSRs are able to predict ΔE_{TS} with a minimal error for a wide range of metals, alkane reactants, and dehydrogenation pathways.

The third part focused on the C–H bond activation of light alkanes (methane, ethane, and propane) on MO and M_1-MO surfaces, with particular emphasis on the C–H bond activation of propane on pristine and doped (Pt, Pd, and Au) monoclinic and tetragonal ZrO_2, CeO_2, and MgO surfaces. The C–H bond activation on MOs and M_1-MOs can be explained based on the Lewis acid-base properties of the surfaces, and among the analyzed pristine, defective, and doped surfaces, the ZrO_2 systems present the best combination of properties for propane activation. Additionally, previously published data were collected, and structure-activity relationships represented by linear correlations between the ΔE_{TS} and ΔE_{FS} were developed. These LSRs generated for the C–H bond activation of alkanes on MOs and M_1-MOs are universal with no functional restrictions and cover a broad structural diversity of MOs and M_1-MOs catalyst surfaces, including the effect of superficial oxygen vacancies, several dopants, and more than one phase of the same MO, and different active

sites. Besides, it was confirmed that the ΔE_{FS} is one of the most general descriptors to estimate ΔE_{TS} on MOs and M_1-MOs, which previously was demonstrated for the C–H bond activation on TMs surfaces.

The last part of this thesis is used to elucidate the factors affecting the hydrogenation of various aldehydes on a Pd-based catalyst. The importance of the side chain in determining the reactivity of the carbonyl group was demonstrated. Although the adsorption mode and strength are affected by the substrate structure, these aspects have proven not to be the decisive factors in the conversion of the carbonyl group. This was demonstrated by a combination of adsorption studies (substrate adsorption, as well as temperature-programmed desorption) and DFT calculations. Besides, based on the hydrogenation calculations of propanal and benzaldehyde on the Pd(111) surface, it is shown that the differences in the activation energies between the two substrates are not enough to explain the inactivity of aliphatic aldehydes found experimentally. Therefore, considering microkinetic models of more elaborate reaction mechanisms becomes a necessity, including the effect of the solvents. Nevertheless, the fundamental understanding offered by DFT calculations still serves as a cornerstone in the complete process of computer-aided catalytic design.

Lastly, the LSRs generated in this work are expected to pave the way toward the computational development of new and better catalyst materials guiding future experiments as a first-hand tool in heterogeneous catalysis. Moreover, in computational catalysis, many challenges are ahead, and it is still necessary to incorporate the dynamic nature of heterogeneous catalysis under realistic experimental conditions either in the LSRs or the microkinetic modeling in order to provide a more effective screening of materials with a potential industrial application such as dry reforming, steam reforming, partial oxidation, and (oxidative) dehydrogenation. Even though the LSRs ease the computational cost of complex reaction networks, the DFT calculations needed to obtain them are time-consuming and cost-ineffective. Hence, the computational-assisted discovery of materials should go through the application of universal LSRs and machine learning synergistic approaches. While this thesis covers the activity of catalysts towards C–H bond activation, selectivity descriptors, and stability measures are also needed in future studies.

References

[1]   J. J. H. B. Sattler, J. Ruiz-Martinez, E. Santillan-Jimenez, B. M. Weckhuysen, *Chemical Reviews* **2014**, *114*, 10613–10653.

[2]   50 percent increase in global propylene production by 2030 leads to shift in historical supply relationships (http://www.plastemart.com/plastic-technical-articles/50-percent-increase-in-global-propylene-production-by-2030-leads-to-shift-in-historical-supp, **2022**.

[3]   M. Bhasin, J. McCain, B. Vora, T. Imai, P. Pujadó, *Applied Catalysis A: General* **2001**, *221*, 397–419.

[4]   P. Chaiyavech, *The Journal of the Royal Institute of Thailand* **2002**, *27*, 1–7.

[5]   J. H. Carter, T. Bere, J. R. Pitchers, D. G. Hewes, B. D. Vandegehuchte, C. J. Kiely, S. H. Taylor, G. J. Hutchings, *Green Chemistry* **2021**, *23*, 9747–9799.

[6]   I. Horiuti, M. Polanyi, *Transactions of the Faraday Society* **1934**, *30*, 1164.

[7]   A. Iglesias-Juez, A. M. Beale, K. Maaijen, T. C. Weng, P. Glatzel, B. M. Weckhuysen, *Journal of Catalysis* **2010**, *276*, 268–279.

[8]   S. Zha, G. Sun, T. Wu, J. Zhao, Z.-J. Zhao, J. Gong, *Chemical Science* **2018**, *9*, 3925–3931.

[9]   M. H. Hansen, J. K. Nørskov, T. Bligaard, *Journal of Catalysis* **2019**, *374*, 161–170.

[10] Z.-J. Zhao, C.-C. Chiu, J. Gong, *Chemical Science* **2015**, *6*, 4403–4425.

[11] S. Wang, Z. H. Zhu, *Energy and Fuels* **2004**, *18*, 1126–1139.

[12] M. B. Ansari, S.-E. Park, *Energy & Environmental Science* **2012**, *5*, 9419.

[13] P. C. Myint, M. A. McClelland, A. L. Nichols, *Industrial & Engineering Chemistry Research* **2016**, *55*, 2252–2266.

[14] M. A. Atanga, F. Rezaei, A. Jawad, M. Fitch, A. A. Rownaghi, *Applied Catalysis B* **2018**, *220*, 429–445.

[15] Y. Wang, P. Hu, J. Yang, Y.-A. Zhu, D. Chen, *Chemical Society Reviews* **2021**, *50*, 4299–4358.

[16] F. Cavani, N. Ballarini, A. Cericola, *Catalysis Today* **2007**, *127*, 113–131.

[17] S. Najari, S. Saeidi, P. Concepcion, D. D. Dionysiou, S. K. Bhargava, A. F. Lee, K. Wilson, *Chemical Society Reviews* **2021**, *50*, 4564–4605.

[18] T. Otroshchenko, G. Jiang, V. A. Kondratenko, U. Rodemerck, E. V. Kondratenko, *Chemical Society Reviews* **2021**, *50*, 473–527.

[19]   C. Li, G. Wang, *Chemical Society Reviews* **2021**, *50*, 4359–4381.

[20]   J. Liu, W. Luo, Y. Yin, X.-Z. Fu, J.-L. Luo, *Journal of Catalysis* **2021**, *396*, 333–341.

[21]   H. Lieske, A. Sárkány, J. Völter, *Applied Catalysis* **1987**, *30*, 69–80.

[22]   B. M. Nagaraja, C.-H. Shin, K.-D. Jung, *Applied Catalysis A: General* **2013**, *467*, 211–223.

[23]   M. L. Yang, Y. A. Zhu, X. G. Zhou, Z. J. Sui, D. Chen, *ACS Catalysis* **2012**, *2*, 1247–1258.

[24]   D. W. McKee, *Journal of the American Chemical Society* **1962**, *84*, 4427–4431.

[25]   Z. Yan, D. W. Goodman, *Catalysis Letters* **2012**, *142*, 517–520.

[26]   E. Nowicka, C. Reece, S. M. Althahban, K. M. H. Mohammed, S. A. Kondrat, D. J. Morgan, Q. He, D. J. Willock, S. Golunski, C. J. Kiely, G. J. Hutchings, *ACS Catalysis* **2018**, *8*, 3454–3468.

[27]   E. Gomez, S. Kattel, B. Yan, S. Yao, P. Liu, J. G. Chen, *Nature Communications* **2018**, *9*, 1398.

[28]   E. Gomez, Z. Xie, J. G. Chen, *AIChE Journal* **2019**, *65*, 1–12.

[29]   I. Takahara, M. Saito, *Chemistry Letters* **1996**, *25*, 973–974.

[30]   B. M. Weckhuysen, R. A. Schoonheydt, *Catalysis Today* **1999**, *51*, 223–232.

[31]   M. P. Conley, M. F. Delley, F. Núñez-Zarur, A. Comas-Vives, C. Copéret, *Inorganic Chemistry* **2015**, *54*, 5065–5078.

[32]   X.-Q. Gao, W.-D. Lu, S.-Z. Hu, W.-C. Li, A.-H. Lu, *Chinese Journal of Catalysis* **2019**, *40*, 184–191.

[33]   T. Otroshchenko, S. Sokolov, M. Stoyanova, V. A. Kondratenko, U. Rodemerck, D. Linke, E. V. Kondratenko, *Angewandte Chemie International Edition* **2015**, *54*, 15880–15883.

[34]   Y. Zhang, Y. Zhao, T. Otroshchenko, H. Lund, M.-M. Pohl, U. Rodemerck, D. Linke, H. Jiao, G. Jiang, E. V. Kondratenko, *Nature Communications* **2018**, *9*, 3794.

[35]   Y. Zhang, Y. Zhao, T. Otroshchenko, S. Han, H. Lund, U. Rodemerck, D. Linke, H. Jiao, G. Jiang, E. V. Kondratenko, *Journal of Catalysis* **2019**, *371*, 313–324.

[36]   N. Jeon, H. Choe, B. Jeong, Y. Yun, *Catalysis Today* **2020**, *352*, 337–344.

[37]   S. Han, Y. Zhao, T. Otroshchenko, Y. Zhang, D. Zhao, H. Lund, T. H. Vuong, J. Rabeah, U. Bentrup, V. A. Kondratenko, U. Rodemerck, D. Linke, M. Gao, H. Jiao, G. Jiang, E. V. Kondratenko, *ACS Catalysis* **2020**, *10*, 1575–1590.

[38]   S. Han, D. Zhao, T. Otroshchenko, H. Lund, U. Bentrup, V. A. Kondratenko, N. Rockstroh, S. Bartling, D. E. Doronkin, J.-D. Grunwaldt, U. Rodemerck, D. Linke, M. Gao, G. Jiang, E. V. Kondratenko, *ACS Catalysis* **2020**, *10*, 8933–8949.

[39]   Q.-y. Chang, K.-q. Wang, Z.-j. Sui, X.-g. Zhou, D. Chen, W.-k. Yuan, Y.-a. Zhu, *ACS Catalysis* **2021**, *11*, 5135–5147.

[40]   H. Wang, H. Huang, K. Bashir, C. Li, *Applied Catalysis A: General* **2020**, *590*, 117291.

[41] H. Xiong, S. Lin, J. Goetze, P. Pletcher, H. Guo, L. Kovarik, K. Artyushkova, B. M. Weckhuysen, A. K. Datye, *Angewandte Chemie International Edition* **2017**, *56*, 8986–8991.

[42] P. Sabatier, *La Catalyse en Chimie Organique*, Paris et Liège: Librairie Polytechnique, **1920**.

[43] A. J. Medford, A. Vojvodic, J. S. Hummelshøj, J. Voss, F. Abild-Pedersen, F. Studt, T. Bligaard, A. Nilsson, J. K. Nørskov, *Journal of Catalysis* **2015**, *328*, 36–42.

[44] F. Studt, I. Sharafutdinov, F. Abild-Pedersen, C. F. Elkjær, J. S. Hummelshøj, S. Dahl, I. Chorkendorff, J. K. Nørskov, *Nature Chemistry* **2014**, *6*, 320–324.

[45] Z.-J. Zhao, S. Liu, S. Zha, D. Cheng, F. Studt, G. Henkelman, J. Gong, *Nature Reviews Materials* **2019**, *4*, 792–804.

[46] S. K. Kaiser, E. Fako, I. Surin, F. Krumeich, V. A. Kondratenko, E. V. Kondratenko, A. H. Clark, N. López, J. Pérez-Ramírez, *Nature Nanotechnology* **2022**, DOI `10.1038/s41565-022-01105-4`.

[47] M. T. Darby, M. Stamatakis, A. Michaelides, E. C. H. Sykes, *The Journal of Physical Chemistry Letters* **2018**, *9*, 5636–5646.

[48] B. Xing, G.-C. Wang, *Physical Chemistry Chemical Physics* **2014**, *16*, 2621.

[49] J. S. Yoo, T. S. Khan, F. Abild-Pedersen, J. K. Nørskov, F. Studt, *Chemical Communications* **2015**, *51*, 2621–2624.

[50] D. Hibbitts, M. Neurock, *Surface Science* **2016**, *650*, 210–220.

[51] M. D. Marcinkowski, M. T. Darby, J. Liu, J. M. Wimble, F. R. Lucci, S. Lee, A. Michaelides, M. Flytzani-Stephanopoulos, M. Stamatakis, E. C. H. Sykes, *Nature Chemistry* **2018**, *10*, 325–332.

[52] M. T. Darby, R. Réocreux, E. C. H. Sykes, A. Michaelides, M. Stamatakis, *ACS Catalysis* **2018**, *8*, 5038–5050.

[53] T. Wang, F. Abild-Pedersen, *Journal of Energy Chemistry* **2021**, *58*, 37–40.

[54] M. L. Yang, Y. A. Zhu, C. Fan, Z. J. Sui, D. Chen, X. G. Zhou, *Physical Chemistry Chemical Physics* **2011**, *13*, 3257–3267.

[55] R. T. Hannagan, G. Giannakakis, R. Réocreux, J. Schumann, J. Finzel, Y. Wang, A. Michaelides, P. Deshlahra, P. Christopher, M. Flytzani-Stephanopoulos, M. Stamatakis, E. C. H. Sykes, *Science* **2021**, *372*, 1444–1447.

[56] T. Saelee, S. Namuangruk, N. Kungwan, A. Junkaew, *The Journal of Physical Chemistry C* **2018**, *122*, 14678–14690.

[57] F. Ma, Q.-Y. Chang, Q. Yin, Z.-J. Sui, X.-G. Zhou, D. Chen, Y.-A. Zhu, *Catalysis Science & Technology* **2020**, *10*, 4938–4951.

[58] L. Xiao, Y.-L. Shan, Z.-J. Sui, D. Chen, X.-G. Zhou, W.-K. Yuan, Y.-A. Zhu, *ACS Catalysis* **2020**, *10*, 14887–14902.

[59] A. A. Latimer, A. R. Kulkarni, H. Aljama, J. H. Montoya, J. S. Yoo, C. Tsai, F. Abild-Pedersen, F. Studt, J. K. Nørskov, *Nature Materials* **2017**, *16*, 225–229.

[60] H. Metiu, S. Chrétien, Z. Hu, B. Li, X. Sun, *The Journal of Physical Chemistry C* **2012**, *116*, 10439–10450.

[61] J. Xu, X.-M. Cao, P. Hu, *The Journal of Physical Chemistry C* **2019**, *123*, 28802–28810.

[62] Q.-Y. Chang, Q. Yin, F. Ma, Y.-A. Zhu, Z.-J. Sui, X.-G. Zhou, D. Chen, W.-K. Yuan, *Industrial & Engineering Chemistry Research* **2019**, *58*, 10199–10209.

[63] Q.-Y. Chang, K.-Q. Wang, P. Hu, Z.-J. Sui, X.-G. Zhou, D. Chen, W.-K. Yuan, Y.-A. Zhu, *AIChE Journal* **2020**, *66*, 10–12.

[64] M. Zeeshan, Q.-Y. Chang, J. Zhang, P. Hu, Z.-J. Sui, X.-G. Zhou, D. Chen, Y.-A. Zhu, *Chinese Journal of Chemistry* **2021**, *39*, 2391–2402.

[65] J. Zhang, R.-J. Zhou, Q.-Y. Chang, Z.-J. Sui, X.-G. Zhou, D. Chen, Y.-A. Zhu, *Catalysis Today* **2021**, *368*, 46–57.

[66] J. N. Bronsted, *Chemical Reviews* **1928**, *5*, 231–338.

[67] M. G. Evans, M. Polanyi, *Transactions of the Faraday Society* **1938**, *34*, 11.

[68] J. Greeley, *Annual Review of Chemical and Biomolecular Engineering* **2016**, *7*, 605–635.

[69] M. Abdelgaid, G. Mpourmpakis, *ACS Catalysis* **2022**, *12*, 4268–4289.

[70] A. H. Motagamwala, J. A. Dumesic, *Chemical Reviews* **2021**, *121*, 1049–1076.

[71] S. Cattaneo, S. Capelli, M. Stucchi, F. Bossola, V. Dal Santo, E. Araujo-Lopez, D. I. Sharapa, F. Studt, A. Villa, A. Chieregato, B. D. Vandegehuchte, L. Prati, *Journal of Catalysis* **2021**, *399*, 162–169.

[72] S. Cattaneo, M. Stucchi, A. Villa, L. Prati, *ChemCatChem* **2019**, *11*, 309–323.

[73] M. J. Ndolomingo, N. Bingwa, R. Meijboom, *Journal of Materials Science* **2020**, *55*, 6195–6241.

[74] P. Gallezot, D. Richard, *Catalysis Reviews* **1998**, *40*, 81–126.

[75] J.-W. Zhang, K.-K. Sun, D.-D. Li, T. Deng, G.-P. Lu, C. Cai, *Applied Catalysis A: General* **2019**, *569*, 190–195.

[76] D. Procházková, P. Zámostný, M. Bejblová, L. Červený, J. Čejka, *Applied Catalysis A: General* **2007**, *332*, 56–64.

[77] S. Cattaneo, D. Bonincontro, T. Bere, C. J. Kiely, G. J. Hutchings, N. Dimitratos, S. Albonetti, *ChemNanoMat* **2020**, *6*, 420–426.

[78] S. Alijani, S. Capelli, S. Cattaneo, M. Schiavoni, C. Evangelisti, K. M. H. Mohammed, P. P. Wells, F. Tessore, A. Villa, *Catalysts* **2019**, *10*, 11.

[79] S. Alijani, S. Capelli, C. Evangelisti, L. Prati, A. Villa, S. Cattaneo, *Catalysis Today* **2021**, *367*, 220–227.

[80] H. Zang, K. Wang, M. Zhang, R. Xie, L. Wang, E. Y. Chen, *Catalysis Science & Technology* **2018**, *8*, 1777–1798.

[81] S. Nishimura, *Handbook of heterogeneous catalytic hydrogenation for organic synthesis*, Wiley-VCH Verlag GmbH, New York, **2001**.

[82] K. Tanaka, Y. Takagi, O. Nomura, I. Kobayashi, *Journal of Catalysis* **1974**, *35*, 24–33.

[83] G. F. Santori, M. L. Casella, O. A. Ferretti, *Journal of Molecular Catalysis A: Chemical* **2002**, *186*, 223–239.

[84] A. Kieboom, J. De Kreuk, H. Van Bekkum, *Journal of Catalysis* **1971**, *20*, 58–66.

[85] M. A. Keane, *Journal of Molecular Catalysis A: Chemical* **1997**, *118*, 261–269.

[86] H. Chen, Y. Wu, S. Qi, Y. Chen, M. Yang, *Applied Catalysis A: General* **2017**, *529*, 79–90.

[87] K. A. Goulas, S. Sreekumar, Y. Song, P. Kharidehal, G. Gunbas, P. J. Dietrich, G. R. Johnson, Y. C. Wang, A. M. Grippo, L. C. Grabow, A. A. Gokhale, F. D. Toste, *Journal of the American Chemical Society* **2016**, *138*, 6805–6812.

[88] K. A. Goulas, Y. Song, G. R. Johnson, J. P. Chen, A. A. Gokhale, L. C. Grabow, F. D. Toste, *Catalysis Science & Technology* **2018**, *8*, 314–327.

[89] J. Ji, L. Zhao, D. Wang, J. Gao, C. Xu, H. Ye, *The Journal of Physical Chemistry C* **2015**, *119*, 1809–1817.

[90] N. W. Ashcroft, N. D. Mermin, *Solid State Physics*, **1976**.

[91] R. G. Parr, W. Yang, *Density-Functional Theory of Atoms and Molecules*, Oxford University Press, New York, **1989**, p. 338.

[92] R. M. Dreizler, E. K. U. Gross, *Density Functional Theory*, Springer-Verlag Berlin Heidelberg, Germany, **1990**.

[93] B. B. Laird, R. B. Ross, T. Ziegler, *Chemical Applications of Density-Functional Theory*, ACS Symposium Series, Washington D.C., **1996**.

[94] R. M. Martin, *Electronic Structure: Basic Theory and Practical Methods*, Cambridge University Press, Cambridge, **2004**.

[95] M. Born, R. Oppenheimer, *Annalen der Physik* **1927**, *389*, 457–484.

[96] P. Hohenberg, W. Kohn, *Physical Review* **1964**, *136*, B864–B871.

[97] W. Kohn, L. J. Sham, *Physical Review* **1965**, *140*, A1133–A1138.

[98] R. Stowasser, R. Hoffmann, *Journal of the American Chemical Society* **1999**, *121*, 3414–3420.

[99] R. van Meer, O. V. Gritsenko, E. J. Baerends, *Journal of Chemical Theory and Computation* **2014**, *10*, 4432–4441.

[100] U. v. Barth, L. Hedin, *Journal of Physics C: Solid State Physics* **1972**, *5*, 1629–1642.

[101] E. Wigner, *Transactions of the Faraday Society* **1938**, *34*, 678.

[102] D. M. Ceperley, B. J. Alder, *Physical Review Letters* **1980**, *45*, 566–569.

[103] S. Grimme, J. Antony, S. Ehrlich, H. Krieg, *The Journal of Chemical Physics* **2010**, *132*, 154104.

[104] J. Wellendorff, K. T. Lundgaard, A. Møgelhøj, V. Petzold, D. D. Landis, J. K. Nørskov, T. Bligaard, K. W. Jacobsen, *Physical Review B* **2012**, *85*, 235149.

[105] J. Wellendorff, T. L. Silbaugh, D. Garcia-Pintos, J. K. Nørskov, T. Bligaard, F. Studt, C. T. Campbell, *Surface Science* **2015**, *640*, 36–44.

[106] S. Mallikarjun Sharada, T. Bligaard, A. C. Luntz, G.-J. Kroes, J. K. Nørskov, *The Journal of Physical Chemistry C* **2017**, *121*, 19807–19815.

[107] J. P. Perdew, K. Burke, M. Ernzerhof, *Physical Review Letters* **1996**, *77*, 3865–3868.

[108] B. Himmetoglu, A. Floris, S. de Gironcoli, M. Cococcioni, *International Journal of Quantum Chemistry* **2014**, *114*, 14–49.

[109] S. L. Dudarev, G. A. Botton, S. Y. Savrasov, C. J. Humphreys, a. P. Sutton, *Physical Review B* **1998**, *57*, 1505–1509.

[110] C. J. Cramer, *Essentials of Computational Chemistry Theories and Models, Vol. 42*, **2004**, pp. 334–342.

[111] F. Jensen, *Introduction to Computational Chemistry*, 3rd, Wiley, **2017**.

[112] F. Bloch, *Zeitschrift für Physik* **1929**, *52*, 555–600.

[113] P. Kratzer, J. Neugebauer, *Frontiers in Chemistry* **2019**, *7*, 106.

[114] D. Vanderbilt, *Physical Review B* **1990**, *41*, 7892–7895.

[115] P. E. Blöchl, *Physical Review B* **1994**, *50*, 17953–17979.

[116] G. Kresse, D. Joubert, *Physical Review B* **1999**, *59*, 1758–1775.

[117] A. Hjorth Larsen, J. Jørgen Mortensen, J. Blomqvist, I. E. Castelli, R. Christensen, M. Dułak, J. Friis, M. N. Groves, B. Hammer, C. Hargus, E. D. Hermes, P. C. Jennings, P. Bjerre Jensen, J. Kermode, J. R. Kitchin, E. Leonhard Kolsbjerg, J. Kubal, K. Kaasbjerg, S. Lysgaard, J. Bergmann Maronsson, T. Maxson, T. Olsen, L. Pastewka, A. Peterson, C. Rostgaard, J. Schiøtz, O. Schütt, M. Strange, K. S. Thygesen, T. Vegge, L. Vilhelmsen, M. Walter, Z. Zeng, K. W. Jacobsen, *Journal of Physics: Condensed Matter* **2017**, *29*, 273002.

[118] G. Jones, J. Jakobsen, S. Shim, J. Kleis, M. Andersson, J. Rossmeisl, F. Abild-Pedersen, T. Bliggard, S. Helveg, B. Hinnemann, *Journal of Catalysis* **2008**, *259*, 147–160.

[119] G. Henkelman, H. Jónsson, *The Journal of Chemical Physics* **2000**, *113*, 9978–9985.

[120] G. Henkelman, B. P. Uberuaga, H. Jónsson, *The Journal of Chemical Physics* **2000**, *113*, 9901.

[121] G. Henkelman, H. Jónsson, *The Journal of Chemical Physics* **1999**, *111*, 7010–7022.

[122] J. S. Plotkin, *Catalysis Today* **2005**, *106*, 10–14.

[123] J. S. Plotkin, The Propylene Gap: How Can It Be Filled?, **2015**.

[124] C. Chen, J. Zhang, B. Zhang, C. Yu, F. Peng, D. Su, *Chemical Communications* **2013**, *49*, 8151.

[125] O. O. James, S. Mandal, N. Alele, B. Chowdhury, S. Maity, *Fuel Processing Technology* **2016**, *149*, 239–255.

[126] W. Cai, R. Mu, S. Zha, G. Sun, S. Chen, Z.-J. Zhao, H. Li, H. Tian, Y. Tang, F. Tao, L. Zeng, J. Gong, *Science Advances* **2018**, *4*, eaar5418.

[127] N. Kaylor, R. J. Davis, *Journal of Catalysis* **2018**, *367*, 181–193.

[128] C. Yang, Z. Wu, G. Zhang, H. Sheng, J. Tian, Z. Duan, H. Sohn, A. J. Kropf, T. Wu, T. R. Krause, J. T. Miller, *Catalysis Today* **2019**, *323*, 123–128.

[129] L. R. Mentasty, O. F. Gorriz, L. E. Cadus, *Industrial & Engineering Chemistry Research* **1999**, *38*, 396–404.

[130] H. Fu, Z.-P. Liu, Z.-H. Li, W.-N. Wang, K.-N. Fan, *Journal of the American Chemical Society* **2006**, *128*, 11114–11123.

[131] A. S. Sandupatla, S. C. Nayak, C. Sivananda, G. Deo, *Catalysis Today* **2019**, *325*, 18–24.

[132] P. Michorczyk, J. Ogonowski, *Reaction Kinetics and Catalysis Letters* **2003**, *78*, 41–47.

[133] R. Larsson, *Molecules* **2015**, *20*, 2529–2535.

[134] G. Sun, Z.-J. Zhao, R. Mu, S. Zha, L. Li, S. Chen, K. Zang, J. Luo, Z. Li, S. C. Purdy, A. J. Kropf, J. T. Miller, L. Zeng, J. Gong, *Nature Communications* **2018**, *9*, 4454.

[135] W. Hu, X. Cao, *Molecules* **2018**, *23*, 126.

[136] J. R. Gallagher, D. J. Childers, H. Zhao, R. E. Winans, R. J. Meyer, J. T. Miller, *Physical Chemistry Chemical Physics* **2015**, *17*, 28144–28153.

[137] D. J. Childers, N. M. Schweitzer, S. M. K. Shahari, R. M. Rioux, J. T. Miller, R. J. Meyer, *Journal of Catalysis* **2014**, *318*, 75–84.

[138] Z. Wu, E. C. Wegener, H.-T. Tseng, J. R. Gallagher, J. W. Harris, R. E. Diaz, Y. Ren, F. H. Ribeiro, J. T. Miller, *Catalysis Science & Technology* **2016**, *6*, 6965–6976.

[139] G. Kresse, J. Furthmüller, *Computational Materials Science* **1996**, *6*, 15–50.

[140] G. Kresse, J. Furthmüller, *Physical Review B* **1996**, *54*, 11169–11186.

[141] J. J. Mortensen, K. Kaasbjerg, S. L. Frederiksen, J. K. Nørskov, J. P. Sethna, K. W. Jacobsen, *Physical Review Letters* **2005**, *95*, 216401.

[142] J. P. Perdew, K. Burke, M. Ernzerhof, *Physical Review Letters* **1996**, *77*, 3865–3868.

[143] H. Orita, N. Itoh, Y. Inada, *Surface Science* **2004**, *571*, 161–172.

[144] S. Lin, J. Ma, L. Zhou, C. Huang, D. Xie, H. Guo, *Journal of Physical Chemistry C* **2013**, *117*, 451–459.

[145] X. Pan, Q.-x. Cai, W.-l. Chen, G.-l. Zhuang, X.-n. Li, J.-g. Wang, *Computational Materials Science* **2013**, *67*, 174–181.

[146] C. Tsai, A. A. Latimer, J. S. Yoo, F. Studt, F. Abild-Pedersen, *The Journal of Physical Chemistry Letters* **2015**, *6*, 3670–3674.

[147] L. Liu, F. Fan, Z. Jiang, X. Gao, J. Wei, T. Fang, *The Journal of Physical Chemistry C* **2017**, *121*, 26287–26299.

[148] J. F. Weaver, C. Hakanoglu, J. M. Hawkins, A. Asthagiri, *The Journal of Chemical Physics* **2010**, *132*, 024709.

[149] S. L. Tait, Z. Dohnálek, C. T. Campbell, B. D. Kay, *The Journal of Chemical Physics* **2006**, *125*, 234308.

[150] S. Wang, V. Petzold, V. Tripkovic, J. Kleis, J. G. Howalt, E. Skúlason, E. M. Fernández, B. Hvolbæk, G. Jones, A. Toftelund, H. Falsig, M. Björketun, F. Studt, F. Abild-Pedersen, J. Rossmeisl, J. K. Nørskov, T. Bligaard, *Physical Chemistry Chemical Physics* **2011**, *13*, 20760.

[151] B. Hammer, L. B. Hansen, J. K. Nørskov, *Physical Review B* **1999**, *59*, 7413–7421.

[152] D. Garcia-Pintos, J. Voss, A. D. Jensen, F. Studt, *The Journal of Physical Chemistry C* **2016**, *120*, 18529–18537.

[153] Y. Gao, L. Neal, D. Ding, W. Wu, C. Baroi, A. M. Gaffney, F. Li, *ACS Catalysis* **2019**, *9*, 8592–8621.

[154] A. Trinchero, A. Hellman, H. Grönbeck, *Surface Science* **2013**, *616*, 206–213.

[155] L. Xiao, F. Ma, Y.-A. Zhu, Z.-J. Sui, J.-H. Zhou, X.-G. Zhou, D. Chen, W.-K. Yuan, *Chemical Engineering Journal* **2019**, *377*, 120049.

[156] J. Weaver, A. Carlsson, R. J. Madix, *Surface Science Reports* **2003**, *50*, 107–199.

[157] J. Niu, Y. Wang, Y. Qi, A. H. Dam, H. Wang, Y.-A. Zhu, A. Holmen, J. Ran, D. Chen, *Fuel* **2020**, *266*, 117143.

[158] I. Alstrup, I. Chorkendorff, S. Ullmann, *Surface Science* **1992**, *264*, 95–102.

[159] T. Niu, Z. Jiang, Y. Zhu, G. Zhou, M. A. van Spronsen, S. A. Tenney, J. A. Boscoboinik, D. Stacchiola, *The Journal of Physical Chemistry B* **2018**, *122*, 855–863.

[160] J. Wang, G.-C. Wang, *The Journal of Physical Chemistry C* **2018**, *122*, 17338–17346.

[161] B. Rahmani Didar, P. B. Balbuena, *International Journal of Quantum Chemistry* **2020**, *120*, 1–9.

[162] Q. K. Do, H.-V. Tran, S. Wang, L. C. Grabow, *Energy Technology* **2019**, *1900732*, 1900732.

[163] Z. Jiang, B. Wang, T. Fang, *Applied Surface Science* **2014**, *320*, 256–262.

[164] X. Lin, Y. Xi, J. Sun, *The Journal of Physical Chemistry C* **2012**, *116*, 3503–3516.

[165] C. Byron, S. Bai, G. Celik, M. S. Ferrandon, C. Liu, C. Ni, A. Mehdad, M. Delferro, R. F. Lobo, A. V. Teplyakov, *ACS Catalysis* **2020**, *10*, 1500–1510.

[166] X. Cao, *RSC Advances* **2016**, *6*, 65524–65532.

[167] M. Myint, B. Yan, J. Wan, S. Zhao, J. G. Chen, *Journal of Catalysis* **2016**, *343*, 168–177.

[168] A. Hook, F. E. Celik, *The Journal of Physical Chemistry C* **2017**, *121*, 17882–17892.

[169] W. H. Weinberg, Y.-K. Sun, *Science* **1991**, *253*, 542–545.

[170] W. Weinberg, Y.-k. Sun, *Surface Science Letters* **1992**, *277*, L39–L46.

[171] D. Kelly, W. H. Weinberg, *The Journal of Chemical Physics* **1996**, *105*, 3789–3793.

[172] J. Pérez-Ramírez, N. López, *Nature Catalysis* **2019**, *2*, 971–976.

[173] V. Pallassana, M. Neurock, *Journal of Catalysis* **2000**, *191*, 301–317.

[174] Z.-P. Liu, P. Hu, *The Journal of Chemical Physics* **2001**, *114*, 8244–8247.

[175] A. Logadottir, T. Rod, J. Nørskov, B. Hammer, S. Dahl, C. Jacobsen, *Journal of Catalysis* **2001**, *197*, 229–231.

[176] J. Nørskov, T. Bligaard, A. Logadottir, S. Bahn, L. Hansen, M. Bollinger, H. Bengaard, B. Hammer, Z. Sljivancanin, M. Mavrikakis, Y. Xu, S. Dahl, C. Jacobsen, *Journal of Catalysis* **2002**, *209*, 275–278.

[177] A. Michaelides, Z.-P. Liu, C. J. Zhang, A. Alavi, D. A. King, P. Hu, *Journal of the American Chemical Society* **2003**, *125*, 3704–3705.

[178] F. Abild-Pedersen, J. Greeley, F. Studt, J. Rossmeisl, T. R. Munter, P. G. Moses, E. Skúlason, T. Bligaard, J. K. Nørskov, *Physical Review Letters* **2007**, *99*, 016105.

[179] S. Wang, B. Temel, J. Shen, G. Jones, L. C. Grabow, F. Studt, T. Bligaard, F. Abild-Pedersen, C. H. Christensen, J. K. Nørskov, *Catalysis Letters* **2011**, *141*, 370–373.

[180] L. Yu, L. Vilella, F. Abild-Pedersen, *Communications Chemistry* **2018**, *1*, 2.

[181] P. Crawford, B. McAllister, P. Hu, *The Journal of Physical Chemistry C* **2009**, *113*, 5222–5227.

[182] B. Xing, X.-Y. Pang, G.-C. Wang, *Journal of Catalysis* **2011**, *282*, 74–82.

[183] V. N. Staroverov, G. E. Scuseria, J. Tao, J. P. Perdew, *Physical Review B* **2004**, *69*, 075102.

[184] E. A. Owen, D. M. Jones, *Proceedings of the Physical Society. Section B* **1954**, *67*, 456–466.

[185] E. Owen, E. Yates, *The London Edinburgh and Dublin Philosophical Magazine and Journal of Science* **1933**, *15*, 472–488.

[186] H. W. King, F. D. Manchester, *Journal of Physics F: Metal Physics* **1978**, *8*, 15–26.

[187] E. R. Jette, F. Foote, *The Journal of Chemical Physics* **1935**, *3*, 605–616.

[188] K. Toch, J. W. Thybaut, G. B. Marin, *AIChE Journal* **2015**, *61*, 880–892.

[189] Y. Chen, D. G. Vlachos, *The Journal of Physical Chemistry C* **2010**, *114*, 4973–4982.

[190] G. Peng, D. Gerceker, M. Kumbhalkar, J. A. Dumesic, M. Mavrikakis, *Catalysis Science & Technology* **2018**, *8*, 2159–2174.

[191] L. Xu, E. E. Stangland, M. Mavrikakis, *Journal of Catalysis* **2018**, *362*, 18–24.

[192] R. T. Vang, K. Honkala, S. Dahl, E. K. Vestergaard, J. Schnadt, E. Lægsgaard, B. S. Clausen, J. K. Nørskov, F. Besenbacher, *Surface Science* **2006**, *600*, 66–77.

[193] K. Lejaeghere, G. Bihlmayer, P. Blaha, S. Bl, V. Blum, D. Caliste, I. E. Castelli, S. J. Clark, A. D. Corso, S. D. Gironcoli, J. K. Dewhurst, I. D. Marco, C. Draxl, M. Dułak, O. Eriksson, K. F. Garrity, L. Genovese, P. Giannozzi, M. Giantomassi, S. Goedecker, X. Gonze, O. Gr, D. R. Hamann, P. J. Hasnip, N. A. W. Holzwarth, D. Ius, D. B. Jochym, D. Jones, G. Kresse, K. Koepernik, K. Emine, I. L. M. Locht, S. Lubeck, M. Marsman, N. Marzari, U. Nitzsche, L. Nordstr, T. Ozaki, L. Paulatto, C. J. Pickard, W. Poelmans, I. J. Matt, *Science* **2016**, *351*, 1–11.

[194] Y. Liu, Z. H. Li, J. Lu, K. N. Fan, *Journal of Physical Chemistry C* **2008**, *112*, 20382–20392.

[195] C. Xiong, S. Chen, P. Yang, S. Zha, Z.-J. Zhao, J. Gong, *ACS Catalysis* **2019**, *9*, 5816–5827.

[196] Z. Liang, T. Li, M. Kim, A. Asthagiri, J. F. Weaver, *Science* **2017**, *356*, 299–303.

[197] Y.-Q. Su, J.-X. Liu, I. A. W. Filot, L. Zhang, E. J. M. Hensen, *ACS Catalysis* **2018**, *8*, 6552–6559.

[198] M. Huš, D. Kopač, B. Likozar, *Journal of Catalysis* **2020**, *386*, 126–138.

[199] J. Paier, C. Penschke, J. Sauer, *Chemical Reviews* **2013**, *113*, 3949–3985.

[200] R. Ciriminna, M. Ghahremani, B. Karimi, M. Pagliaro, R. Luque, *Current Opinion in Green and Sustainable Chemistry* **2020**, *25*, 100358.

[201] S. Ji, Y. Chen, X. Wang, Z. Zhang, D. Wang, Y. Li, *Chemical Reviews* **2020**, *120*, 11900–11955.

[202] N. Asikin-Mijan, H. Mohd Sidek, A. G. AlSultan, N. A. Azman, N. A. Adzahar, H. C. Ong, *Catalysts* **2021**, *11*, 1470.

[203] M. Peng, Z. Jia, Z. Gao, M. Xu, D. Cheng, M. Wang, C. Li, L. Wang, X. Cai, Z. Jiang, H. Jiang, N. Wang, D. Xiao, H. Liu, D. Ma, *ACS Catalysis* **2022**, *12*, 2244–2252.

[204] F. Maurer, J. Jelic, J. Wang, A. Gänzler, P. Dolcet, C. Wöll, Y. Wang, F. Studt, M. Casapu, J.-D. Grunwaldt, *Nature Catalysis* **2020**, *3*, 824–833.

[205] B. Qiao, A. Wang, X. Yang, L. F. Allard, Z. Jiang, Y. Cui, J. Liu, J. Li, T. Zhang, *Nature Chemistry* **2011**, *3*, 634–641.

[206] A. I. Stadnichenko, V. V. Muravev, S. V. Koscheev, V. I. Zaikovskii, H. A. Aleksandrov, K. M. Neyman, A. I. Boronin, *Surface Science* **2019**, *679*, 273–283.

[207] H. Aljama, J. K. Nørskov, F. Abild-Pedersen, *The Journal of Physical Chemistry C* **2017**, *121*, 16440–16446.

[208] R. R. Seemakurthi, G. Canning, Z. Wu, J. T. Miller, A. K. Datye, J. Greeley, *ACS Catalysis* **2021**, *11*, 9588–9604.

[209] L. Xiao, P. Hu, Z.-J. Sui, D. Chen, X.-G. Zhou, W.-K. Yuan, Y.-A. Zhu, *Journal of Catalysis* **2021**, *404*, 32–45.

[210] T. Kropp, M. Mavrikakis, *Journal of Catalysis* **2019**, *377*, 577–581.

[211] J.-X. Liu, Y. Su, I. A. W. Filot, E. J. M. Hensen, *Journal of the American Chemical Society* **2018**, *140*, 4580–4587.

[212] A. A. Latimer, H. Aljama, A. Kakekhani, J. S. Yoo, A. Kulkarni, C. Tsai, M. Garcia-Melchor, F. Abild-Pedersen, J. K. Nørskov, *Physical Chemistry Chemical Physics* **2017**, *19*, 3575–3581.

[213] Z. Xie, Z. Li, P. Tang, Y. Song, Z. Zhao, L. Kong, X. Fan, X. Xiao, *Journal of Catalysis* **2021**, *397*, 172–182.

[214] M. Abdelgaid, J. Dean, G. Mpourmpakis, *Catalysis Science & Technology* **2020**, *10*, 7194–7202.

[215] S. M. Kozlov, K. M. Neyman, *Journal of Catalysis* **2016**, *344*, 507–514.

[216] G. Liu, L. Zeng, Z. J. Zhao, H. Tian, T. Wu, J. Gong, *ACS Catalysis* **2016**, *6*, 2158–2162.

[217] M. Dixit, P. Kostetskyy, G. Mpourmpakis, *ACS Catalysis* **2018**, *8*, 11570–11578.

[218] R. Martin, M. Kim, A. Franklin, Y. Bian, A. Asthagiri, J. F. Weaver, *Physical Chemistry Chemical Physics* **2018**, *20*, 29264–29273.

[219] Y. Bian, M. Kim, T. Li, A. Asthagiri, J. F. Weaver, *Journal of the American Chemical Society* **2018**, *140*, 2665–2672.

[220] A. Antony, A. Asthagiri, J. F. Weaver, *The Journal of Chemical Physics* **2013**, *139*, 104702.

[221] V. Fung, F. Tao, D. Jiang, *Physical Chemistry Chemical Physics* **2018**, *20*, 22909–22914.

[222] G. Righi, R. Magri, A. Selloni, *The Journal of Physical Chemistry C* **2020**, *124*, 17578–17585.

[223] Y. Tsuji, K. Yoshizawa, *Journal of Physical Chemistry C* **2020**, *124*, 17058–17072.

[224] J. F. Weaver, J. A. Hinojosa Jr., C. Hakanoglu, A. Antony, J. M. Hawkins, A. Asthagiri, *Catalysis Today* **2011**, *160*, 213–227.

[225] D. Knapp, T. Ziegler, *The Journal of Physical Chemistry C* **2008**, *112*, 17311–17318.

[226] T. L. M. Pham, E. G. Leggesse, J. C. Jiang, *Catalysis Science & Technology* **2015**, *5*, 4064–4071.

[227] Z. Xie, T. Yu, W. Song, J. Li, Z. Zhao, B. Liu, Z. Gao, D. Li, *ACS Catalysis* **2020**, *10*, 14678–14693.

[228] W. Tang, Z. Hu, M. Wang, G. D. Stucky, H. Metiu, E. W. McFarland, *Journal of Catalysis* **2010**, *273*, 125–137.

[229] Y. Liu, L. Annamalai, P. Deshlahra, *The Journal of Physical Chemistry C* **2019**, *123*, 28168–28191.

[230] D. Tian, K. Li, Y. Wei, X. Zhu, C. Zeng, X. Cheng, Y. Zheng, H. Wang, *Physical Chemistry Chemical Physics* **2018**, *20*, 11912–11929.

[231] C. Kittel, *Introduction to Solid State Physics*, 8th, John Wiley & Sons, Inc., Hoboken, NJ, USA, **2005**.

[232] L. Li, R. Tan, S. Luo, C. Jiang, F. Jing, *Applied Catalysis A: General* **2022**, *635*, 118565.

[233] Y. Mahara, K. Murata, K. Ueda, J. Ohyama, K. Kato, A. Satsuma, *ChemCatChem* **2018**, *10*, 3384–3387.

[234] A. D. Mayernick, M. J. Janik, *The Journal of Physical Chemistry C* **2008**, *112*, 14955–14964.

[235] T. Li, R. Rai, Z. Liang, M. Kim, A. Asthagiri, J. F. Weaver, *The Journal of Physical Chemistry C* **2016**, *120*, 9863–9873.

[236] R. Shekhar, M. A. Barteau, R. V. Plank, J. M. Vohs, *The Journal of Physical Chemistry B* **1997**, *101*, 7939–7951.

[237] S. Chen, R. Wojcieszak, F. Dumeignil, E. Marceau, S. Royer, *Chemical Reviews* **2018**, *118*, 11023–11117.

[238] D. P. Duarte, R. Martínez, L. J. Hoyos, *Industrial & Engineering Chemistry Research* **2016**, *55*, 54–63.

[239] A. Antony, C. Hakanoglu, A. Asthagiri, J. F. Weaver, *The Journal of Chemical Physics* **2012**, *136*, 054702.

[240] W. T. Tysoe, R. M. Ormerod, R. M. Lambert, G. Zgrablich, A. Ramirez-Cuesta, *The Journal of Physical Chemistry* **1993**, *97*, 3365–3370.

Appendixes

A. Universal Linear Scaling Relationships for the C–H Bond Activation of Alkanes on Metal Oxides and Single-atom-doped Metal Oxides

Table A.1. Calculated initial, transition, and final state energies for the C – H activation of alkanes on MO and M_1 – MO surfaces, all values in eV

		IS	TS	FS
	BEEF-vdW			
mZrO2(111)	Methane	-0.15	1.47	0.94
	Ethane	-0.16	1.45	0.94
	Propane	-0.21	1.59	0.93
d-	Propane	-0.25	0.16	-1.29
Pt-	Propane	-0.25	1.06	-1.01
d-Pt-	Propane	-0.21	0.18	-0.95
Pd-	Propane	-0.29	0.95	-1.12
d-Pd-	Propane	-0.26	0.89	-0.29
Au-	Propane	-0.26	0.24	-1.17
d-Au-	Propane	-0.35	1.43	-0.31
tZrO2(101)	Propane	-0.20	1.87	1.73
	Methane	-0.16	1.05	0.72
	Ethane	-0.21	1.36	0.76
	Propane	-0.25	1.42	0.88
d-	Propane	-0.25	-0.03	-1.61
Pt-	Propane	-0.10	1.09	-0.76
d-Pt-	Propane	-0.27	0.17	-1.43
Pd-	Propane	-0.25	0.89	-0.80
d-Pd-	Propane	-0.30	0.40	-1.13
Au-	Propane	-0.26	0.32	-1.01
d-Au-	Propane	-	-	-
CeO2(111)	Propane	-0.22	0.84	0.22
	Methane	-0.15	1.03	0.54
	Ethane	-0.19	0.90	0.28
	Propane	-0.25	0.70	0.06
d-	Propane	-0.14	0.53	-0.44
Pt-	Propane	-0.27	0.16	-1.47
d-Pt-	Propane	-	-	-
Pd-	Propane	-0.27	0.29	-1.43
d-Pd-	Propane	-	-	-
Au-	Propane	-	-	-
d-Au-	Propane	-	-	-
MgO (100)	Propane	-0.23	2.31	2.30
d-	Propane	-	-	-
Pt-	Propane	-0.20	1.85	1.88
d-Pt-	Propane	-	-	-
Pd-	Propane	-0.19	1.89	1.77
d-Pd-	Propane	-	-	-
Au-	Propane	-0.20	1.60	0.97
d-Au-	Propane	-	-	-

Table A.2. Collected initial, transition, and final state energies for the C – H activation of alkanes on MO and M_1 – MO surfaces, all values in eV

		IS	TS	FS
	BEEF-vdW			
β-Ga$_2$O$_3$(100)	Propane	-0.25	1.48	0.80
Pt-	Propane	-0.25	1.24	-0.15
Fe-	Propane	-0.24	1.32	0.84
Ru-	Propane	-0.27	0.74	-0.07
Os-	Propane	-0.21	0.83	-0.07
Co-	Propane	-0.23	1.06	0.28
Rh-	Propane	-0.27	0.56	-0.40
Ir-	Propane	-0.24	0.39	-0.60
Mn-	Propane	-0.23	1.46	0.82
Cu-	Propane	-0.23	0.47	-0.47
Ag-	Propane	-0.23	0.66	-0.47
Au-	Propane	-0.20	1.36	-0.20
Ni-	Propane	-0.23	0.98	-0.18
Pd-	Propane	-0.25	1.08	-0.33
Pt-	Propane			
V$_2$O$_3$(0001)	Propane	-0.29	1.12	0.25
Mn-	Propane	-0.44	0.84	0.15
Fe-	Propane	-0.38	1.03	0.28
Co-	Propane	-0.36	1.11	0.15
Ni-	Propane	-0.35	1.07	0.07
Cu-	Propane	-0.30	1.11	-0.09
ZnO(1010)	Propane	-	1.19	0.17
	Propane	-	1.10	0.21
	Propane	-0.32	1.09	0.64
d-	Propane	-0.27	1.54	0.87
Pt-	Propane	-0.28	0.94	0.74
$\alpha-$Cr$_2$O$_3$(0001)	Propane	-0.26	1.39	0.82
d-	Propane			
Pt-	Propane	-0.28	1.13	0.23
MgO(111) M-Oct	Methane	–	0.70	0.03
MgO(111) O-Oct	Methane	–	0.84	-0.01
MgO(310)	Methane	–	0.78	0.53
MgO(211)	Methane	–	0.58	
MgO(100)	Methane	–	2.96	2.95
MgO(110)	Methane	–	0.53	-0.09
CaO(110)	Methane	–	0.45	-0.21
	PBE-D3			
$\gamma-$Al$_2$O$_3$(100)	Propane	-0.37	0.86	0.45
	Propane	-0.20	1.57	1.44
	Propane	-0.09	1.84	1.59
	Propane	-0.19	1.51	1.07
$\gamma-$Al$_2$O$_3$(110)	Propane	-0.67	0.49	-0.92
	Propane	-0.71	0.92	0.16
	Propane	-0.31	1.24	0.33
	Propane	-0.27	1.17	0.74
	Propane	-0.41	0.75	-0.12
$\gamma-$Al$_2$O$_3$ (110)	Propane	-0.24	1.28	0.75
d-	Propane	-0.27	0.99	0.33
d-	Propane	-0.49	0.61	-0.62
IrO$_2$(110)	Propane	-1.51	-1.19	-2.54
	Ethane	-1.11	-0.72	-2.12
	Methane	-0.68	-0.48	-1.82
rTiO$_2$(110)	Methane	-0.39	0.43	-0.44
Ir-	Methane	-0.83	-0.62	-2.43
Pt-	Methane	-0.95	-0.82	-3.17

Table A.2. (continued)

		IS	TS	FS
CeO$_2$(111)	Methane			
d-	Methane	-0.69	0.56	0.03
d-Ag-	Methane	-0.76	-0.27	-2.45
d-Ag-CeO$_2$(100)	Methane	-1.01	-0.80	-3.20
PdO(101)	Methane	-0.41	0.17	-0.78

PBE				
tZrO$_2$(101)	Propane	-0.19	0.81	0.52
d-	Propane	-0.05	0.56	-0.34
2Ov-Cr	Propane	-0.04	0.95	-0.03
mZrO$_2$(111)	Propane	0.00	1.25	0.94
d-	Propane	-0.14	0.02	-1.04
β−Ga$_2$O$_3$(100)	Propane	–	0.79	0.62
IrO$_2$ (110)	Methane	-0.41	-0.16	-1.50
	Methane	-0.37	-0.12	-1.46
	Methane	-	0.42	-1.11
F-	Methane	-	0.08	-1.71
CeO$_2$(111)	Methane		1.42	1.33
rTiO$_2$(110)	Methane	-0.10	0.77	-0.12
V-	Methane	0.02	0.98	0.02
Cr-	Methane	-0.04	0.77	-0.41
Mn-	Methane	-0.04	0.48	-1.12
Fe-	Methane	-0.04	1.02	-0.39
Co-	Methane	-0.04	0.70	-1.25
Ni-	Methane	-0.03	0.49	-1.85
Zr-	Methane	-0.22	0.58	0.00
Nb-	Methane	-0.12	0.76	-0.24
Mo-	Methane	0.03	0.72	-0.33
Tc-	Methane	-0.29	0.22	-1.12
Ru-	Methane	-0.26	0.12	-1.49
Rh-	Methane	-0.34	-0.07	-1.94
Pd-	Methane	-0.32	-0.19	-2.60
Hf-	Methane	-0.21	0.59	0.05
Ta-	Methane	-0.12	0.66	-0.35
W-	Methane	-0.10	0.60	-0.59
Re-	Methane	-0.35	0.12	-1.18
Os-	Methane	-0.42	-0.05	-1.66
Ir-	Methane	-0.51	-0.28	-2.14
Pt-	Methane	-0.62	-0.47	-2.86
aTiO$_2$(101)	Propane	-0.09	1.50	0.70
	Propane	-0.08	1.73	1.54
d-	Propane	-0.08	1.36	0.45
d-	Propane	-0.09	1.63	1.33
V$_2$O$_5$(001)	Propane	-	1.12	0.66
	Propane	-	1.40	1.25
PdO(101)	Methane	-0.16	0.42	-0.51
	Methane	-	0.67	-0.41

PW91				
V$_2$O$_5$(001)	Propane	–	1.32	0.42
Cr$_2$O$_3$(0001)	Propane	-0.37	0.88	0.48
	Propane	-0.37	0.90	0.36
CeO$_2$(111)	Methane	-0.21	1.29	1.08

Table A.2. (continued)

		IS	TS	FS
Pt-	Methane	-0.16	1.08	0.90
PdO(101)	Methane	–	0.64	-0.44
optB88-vdW				
$IrO_2(110)$	Methane	-0.76	-0.46	-1.85
$rTiO_2(110)$	Methane	-0.37	0.58	-0.41
Ir-	Methane	-0.75	-0.45	-2.39
Pt-	Methane	-0.84	-0.65	-3.11
vdW-DF2				
$V_2O_5(001)$	Ethane	-0.13	1.26	1.07
PBE-sol				
$d-CeO_2(110)$	Methane	-0.15	1.01	0.22
$d-CeO_2(110)$	Methane	-0.13	1.16	0.25

B.   Acronyms

AC	Activated Carbon
ASE	Atomic Simulation Environment
BEEF-vdW	Bayesian Error Estimation Functional with van der Waals
BEP	Brønsted-Evans-Polanyi
CI	Confidence Intervals
D3	Grimme's dispersion corrections model
DFT	Denstiy Functional Theory
DH	Dehydrogenation
DOF	Degrees of Freedom
DOS	Density of States
FS	Final State
GGA	Generalized Gradient Approximation
IS	Initial State
KS	Kohn and Sham
LAB	Lewis Acid-Base
LSR	Linear Scaling Relationships
L(S)DA	Local (Spin) Density Approximation
LUMO	Lowest Unoccupied Molecular Orbital
non-oxiDH	Non-oxidative Dehydrogenation
MAE	Mean Absolute Error
mtpa	Million ton per annum
M_1-MO	Single Atom Doped Metal Oxide
MO	Metal Oxide
$mZrO_2$	Monoclinic Zirconia
NEB	Nudged Elastic Band Method
ODH	Oxidative Dehydrogenation
$ODH-CO_2$	Oxidative Dehydrogenation with Carbon Dioxide
$ODH-O_2$	Oxidative Dehydrogenation with Molecular Oxygen
OVFE	Oxygen Vacancy Formation Energy
PAW	Projected Augmented Wave
PBE	Perdew-Burke-Ernzerhof functional
PDOS	Projected Density of States
PW91	Perdew Wang 91 Functional
RPBE	Revised Perdew-Burke-Ernzerhof Functional
RWGS	Reverse Water-Shift Reaction
SAC	Single atom catalysts

SAR	Scaling-Activity Relationships
TM	Transition Metal
TPD	Temperature-Programmed desorption
$tZrO_2$	Tetragonal Zirconia
TS	Transition State
U	Hubbard model
VASP	Vienna Ab initio Simulation Package
vdW	van der Waals
ZPE	Zero Point Energy

Acknowledgements

List of Publications

1. **Araujo-Lopez, E.**; Joos, L.; Vandegehuchte, B. D.; Sharapa, D. I.; Studt, F. Theoretical Investigations of (Oxidative) Dehydrogenation of Propane to Propylene over Palladium Surfaces. *J. Phys. Chem. C* **2020**, 124 (5), 3171–3176.
   https://doi.org/10.1021/acs.jpcc.9b11424

2. **Araujo-Lopez, E.**; Vandegehuchte, B. D.; Curulla-Ferré, D.; Sharapa, D. I.; Studt, F. Trends in the Activation of Light Alkanes on Transition-Metal Surfaces. *J. Phys. Chem. C* **2020**, 124 (50), 27503–27510.
   https://doi.org/10.1021/acs.jpcc.0c08076

3. Cattaneo, S.; Capelli, S.; Stucchi, M.; Bossola, F.; Dal Santo, V.; **Araujo-Lopez, E.**; Sharapa, D. I.; Studt, F.; Villa, A.; Chieregato, A.; Vandegehuchte, B. D.; Prati, L. Discovering the Role of Substrate in Aldehyde Hydrogenation. *J. Catal.* **2021**, 399, 162–169.
   https://doi.org/10.1016/j.jcat.2021.05.012

4. **Araujo-Lopez, E.**; Kazmierczak, K; Vandegehuchte, B. D.; Curulla-Ferré, D.; Sharapa, D. I.; Studt, F. Universal Linear Scaling Relationships for the C–H Bond Activation of Alkanes on Metal Oxides and Single-atom-doped Metal Oxides. *To be submitted.*

5. Cattaneo, S.; Capelli, S.; Stucchi, M.; Bossola, F.; Dal Santo, V.; **Araujo-Lopez, E.**; Sharapa, D. I.; Studt, F.; Villa, A.; Chieregato, A.; Kazmierczak, K; Vandegehuchte, B. D.; Prati, L. Hydrodeoxigenation of Carboxylic Acids on Iron-Palladium Catalysts. *In Preparation.*

Eidesstattliche Erklärung

Hiermit versichere ich eidesstattlich, dass ich die hier vorgelegte Dissertation selbstständig angefertigt habe und keine anderen Quellen und Hilfsmittel genutzt habe als die hier angegebenen. Die wörtlich und inhaltlich übernommenen Stellen wurden als solche kenntlich gemacht. Die Regeln zur Sicherung guter wissenschaftlicher Praxis des Karlsruher Instituts für Technologie (KIT) in der gültigen Fassung wurden beachtet und Primärdaten gemäß Abs. A(6) gesichert. Die elektronische Version der Arbeit stimmt mit der schriftlichen überein. Die Arbeit wurde in gleicher oder ähnlicher Form noch keiner anderen Prüfungsbehörde zur Erlangung eines akademischen Grades vorgelegt.

Karlsruhe, den 31.05.2022